Master's thesis

NTNU
Norwegian University of Science and Technology
Faculty of Natural Sciences
Department of Biotechnology and Food Science

Vilde Årdal

Cell Wall Biomineralization in the Centric Diatom *Thalassiosira pseudonana*: Investigation of the Putative Role of Silicanin Tp23191 and the Impact of Microfilaments and Microtubules

Master's thesis in Chemical Engineering and Biotechnology
Supervisor: Olav Vadstein and Tore Brembu
July 2020

NTNU
Norwegian University of Science and Technology

Vilde Årdal

Cell Wall Biomineralization in the Centric Diatom *Thalassiosira pseudonana*: Investigation of the Putative Role of Silicanin Tp23191 and the Impact of Microfilaments and Microtubules

Master's thesis in Chemical Engineering and Biotechnology
Supervisor: Olav Vadstein and Tore Brembu
July 2020

Norwegian University of Science and Technology
Faculty of Natural Sciences
Department of Biotechnology and Food Science

NTNU
Norwegian University of
Science and Technology

Preface

The research material presented in this master thesis was obtained at the Analysis and Control of Microbial Systems (ACMS) group at the Department of Biotechnology and Food Science at the Norwegian University of Science and Technology (NTNU) Spring 2020. This master thesis is a prolongation of the work carried out during the specialization project performed by the author in Autumn 2019 [1].

Vilde Årdal

Trondheim, July 2020

Summary

Diatoms incorporate amorphous silica into the cell wall, the frustule, in a characteristic species-specific pattern. The silica structure is of high strength. Hence, the diatoms are suitable for high scale production of nanopatterned silica. While many organic components like proteins, long-chain polyamines, and scaffold structures such as the cytoskeleton play a role in biosilica formation, the process as a whole is poorly understood. The purpose of this thesis was to get an overview of biosilica creation in diatoms, the potential use of diatom frustules in biotechnological applications, and investigate the putative association between silicanins, elements of the cytoskeleton, and frustule assembly. This was achieved by conducting two literature studies and laboratory research. The literature studies gave an overview of the common morphological features of diatoms, how frustule assembly is related to the cell cycle, and an insight into the potential of diatom frustules in drug delivery systems and immunodiagnostics.

The putative association between silicanin Tp23191 and frustule assembly, and how microfilaments and microtubules contribute to frustule morphology were investigated with laboratory research. Tp23191 is a member of the newly discovered silicanin family, which is predicted to be silicalemma-spanning proteins. Before this thesis, the fusion protein mNeonGreen (mNG)-Tp23191 under a native promotor was created by the author and transformed into *Thalassiosira pseudonana*. Examination of transgenic lines localized the fusion protein in regions consistent with the cell wall, and valve and girdle band Silica Deposition Vesicles (SDVs). Additionally, the results from a synchronization study led to the assumption that the highest expression of mNG-Tp23191 is in the G_2+M phase of the cell cycle, where valves are created in valve SDVs.

In this thesis, transgenic lines of *T. pseudonana* were successfully synchronized in growth, and cell cycle stages were determined. Study of mNG-Tp23191 fusion protein involved intracellular localization with microscopy, immunodetection of mNG with western blot, and detection of fluorescence signal within the range of mNG with flow cytometry. However, all functional studies were inconclusive because of the unexpected reduction in the expression level of mNG-Tp23191 in transgenic lines of *T. pseudonana*. It is assumed that the change was due to gene silencing, and the experiments should be repeated. *T. pseudonana* cultures were separately treated with the microfilament inhibitor cytochalasin D and the microtubule inhibitors colchicine and oryzalin. Observations of morphological changes in frustules examined by scanning electron microscopy indicated the involvement of microfilaments and microtubules in the formation of frustules in *T. pseudonana*, but their specific contribution to frustule assembly is not confirmed. Overall, the knowledge of biosilica creation is fragmented, and further characterization of intermediates, as well as a detailed description of molecular mechanisms involved in frustule assembly, are advantageous for the future development of diatom-based applications.

Samandrag

Kiselalgar inkorporerar kiseldioksid, betre kjent som silika (SiO_2), i celleveggen, frustulen, i eit karakteristisk og artspesifikt mønster. Denne silika-strukturen er av høg styrke, og nettopp difor er det fordelaktig å nytte kiselalgar for høgskala-produksjon av mønsterforma silika. Trass i at mange organiske komponentar som protein, langkjeda polyamin og rammestrukturar slik som cytoskjelettet er kjende for å delta i danninga av biosilika er prosessen i si heilheit lite kjent. Målet med denne oppgåva var å få eit innblikk i korleis biosilika vert danna i kiselalgar, potensiell bruk av frustular i bioteknologiske applikasjonar, og å undersøke den antekne assosiasjonen mellom silikaniner, element i cytoskjelettet, og danning av frustular. For å oppnå dette vart det gjennomført to literaturstudier og eksperimentell forskning. Litteraturstudia gav ei oversikt over dei vanlege morfologiske trekka hos kiselalgar, korleis framstilling av frustular er relatert til cellesyklusen i kiselalgar, og eit innblikk i potensiell framtidig bruk av frustular i medikamementell behandling og immundiagnostikk.

Den anteke assosiasjonen mellom silikanin Tp23191, danning av frustular og korleis mikrofilamenter og mikrotubuli bidreg til frustulemorfologi vart undersøkt eksperimentelt. Tp23191 tilhøyrer den nyleg oppdaga proteinfamilien silikaniner som er anteke å vere kopla til silikalemma, membranen rundt Silika Deponerings Vesiklar (SDVar). Før oppstart av denne masteroppgåva vart fusjonsproteinet mNeonGreen(mNG)-Tp23191 under same promotor som det opprinnlege genet konstruert av forfattaren og transformert inn i *Thalassiosira pseudonana*. Fusjonsproteinet vart lokalisert i celler frå transgene linjer som samsvarte med valve og girdle band SDVar, og resultat frå eit synkroniseringsstudie indikerte at mNG-Tp23191 er høgst uttrykt i fase G_2+M i cellesyklusen, der valves er danna i valve SDVar.

I denne oppgåva vart trangene linjer av *T. pseudonana* vellykka synkronisert i vekst, og tal celler i dei ulike fasane blei kalkulert. Studiet av mNG-Tp23191 i transgene linjer innebar intracellulær lokalisering med mikroskopiering, immunodeteksjon av mNG med western blot og deteksjon av fluorescens signal frå mNG med flowcytometri. Ein uventa reduksjon i ekspresjonsnivå av mNG-Tp23191 i transgene linjer av *T. pseudonana* førte til at studia ikkje gav resultat. Det er anteke at ei undertrykking av genekspresjon var grunnen til endringa, og eksperimenta burde gjentakast. Kulturar med *T. pseudonana* var individuelt behandla med cytochalasin D som hindrar polymerisering av mikrofilamenter, og colchicine og oryzalin som hindrar vekst av mikrotubuli. Ved bruk av skanningelektronmikroskop vart frustular avbilda. Basert på observerte morfologiske endringar, er det rimeleg å konkludere med at mikrofilamenter og mikrotubuli påverkar danninga av frustular i *T. pseudonana*, men at den spesifikke rolla framleis er ukjent. Kort oppsummert så er kunnskapen om danninga av biosilika mangelfull, og ytterlegare karakterisering av mellomprodukt og detaljert forståing av molekylære mekanismar involvert i danning av frustular vil vere fordelaktig for den framtidige utviklinga av kiselalge-baserte applikasjonar.

Aknowledgements

First, I would like to thank my supervisor Prof. Olav Vadstein and Researcher Tore Brembu for support and guidance throughout my thesis. I especially want to thank Tore Brembu for his valuable help in the form of shared insights, feedback, and experimental assistance. Also, thanks to the Ph.D. candidates Annika Messemer and Marthe Hafskjold, for your assistance in some of my experiments. Thank you, Thi My Linh Hoang, for your assistance in taking SEM images as I did not have access due to COVID-19 restrictions.

Marita Gresseth, I am grateful for all the laughs and collaboration in the laboratory during this thesis. Eli Anne Støfring, thank you for reading through parts of my thesis, and all the moral support you have given me along the way. I would also like to acknowledge Maya Keilen for all the psychological support and good friendship while studying.

Finally, I would like to thank friends and family for all their love and support. To all of you who have contributed to five good years in Trondheim, I am deeply grateful.

Abbreviations

AFM	Atomic force microscopy
APS	Ammonium persulfate
ARP	Actin-related proteins
bp	Base pair
C5-MTases	Cytosine-5 DNA methyltransferases
CAH	CEN6-ARSH4-HIS3
CLSM	Confocal laser scanning microscopy
CN	Central nodule
CRISPR	Clustered regularly interspaced short palindromic repeats
DE	Diatomaceous earth
DMSO	Dimethyl sulfoxide
EDTA	Ethylenediaminetetraacetic acid
ELISA	Enzyme-linked immunosorbent assay
ER	Endoplasmatic reticulum
FCM	Flow cytometry
fsc	Forward scatter
FSW	Filtered seawater
gen	Gentamicin
gbs	Girdle bands
IASEM	Ion-abrasion scanning electron microscopy
IgG	Immunoglobulin G
kan	Kanamycin
LB	Luria-Bertani
LCPA	Long-chain polyamines
LiDSI	Live diatom silica immobilization
MC	Microtubule-organizing center
mNG	mNeonGreen
mNG-Tp23191	*T. pseudonana* transformant with fusion protein
MQ	Milli-Q
ntc	Nourseothricin
page	Polyacrylamide gel electrophoresis
PBS	Phosphate-buffered saline
PCR	Polymerase chain reaction
PSS	Primary silicification site
PVDF	Polyvinylidene difluoride
RXL	Protease cleavage site
SAP	Silicalemma Associated Proteins
SEM	Scanning electron microscopy
SERS	Surface-enhanced Raman scattering
SDS	Sodium decyl sulfate
SDV	Silica Deposition Vesicle
Si	Silicon
Sin-1	Silicanin-1

siRNA	Small interfering RNA
SIT	Silicic acid transporter protein
SP	Signal peptide
SOC	Super Optimal Broth
TAE	Tris-acetate-EDTA
TEM	Transmission electron microscopy
TEMED	Tetramethylethylenediamine
TM	Transmembrane
TpWt	*T. pseudonana* wild type

Table of Contents

Chapter 1

Introduction

1.1 General Background

In the last decades, there has been a growing interest in developing environmentally friendly and economical alternatives to existing products. New products should, therefore, be sustainable and with a lower production cost. In the quest to meet these requirements, microorganisms have been proposed as possible elements in commercial products, technical applications, and as production organisms. It is assumed that the utilization of microorganisms in industrial manufacturing can improve a wide range of applications and simultaneously be produced at a lower environmental cost.

Biomineralization, the formation of biominerals into complex structures, is widely distributed and occurs in organisms for various purposes [2, 3, 4]. The implementation of inorganic pore-patterned structures in nanotechnological applications and biomineralization based technology holds great potential towards a ”greener” industry. The creation of a three-dimensional silica structure in diatoms is perhaps the most investigated biomineralization process. Diatoms incorporate amorphous silica into the cell wall, the frustule, in a characteristic species-specific pattern [5, 6, 7, 8]. The silica structure is of high strength, and this process of biosilicification appears to be unique as many proteins involved are only conserved in diatoms [8]. The mechanism is under strict biological control, and the structure is preserved through generations [2]. Hence, the diatoms can be suitable for high scale production of nanopatterned silica.

The diatoms are part of the heterokont lineage. Phylogenomic studies imply that the precursors of diatoms arose from a secondary endosymbiosis between a red alga, green alga, and a heterotrophic host cell between 700 and 1200 Ma years ago [9, 10]. A schematic representation of the development is given in Figure 1.1.1. The ancestral secondary endosymbiont developed into Stramenopiles, a major branch of eukaryotes in the phylogenetic tree. Fossils record the ancestral diatom back to 200 Ma years ago, with an evolution from a heavily silicified ancestral diatom, to the development of two major classes of diatoms; centric and pennate diatoms [9, 11, 12]. Fossil studies by Chacón-Baca et al. estimate that this evolution occurred around 70 Ma years ago [13]. However, other fossil studies indicate that the centrics developed approximately 90 million years before the pennates [14].

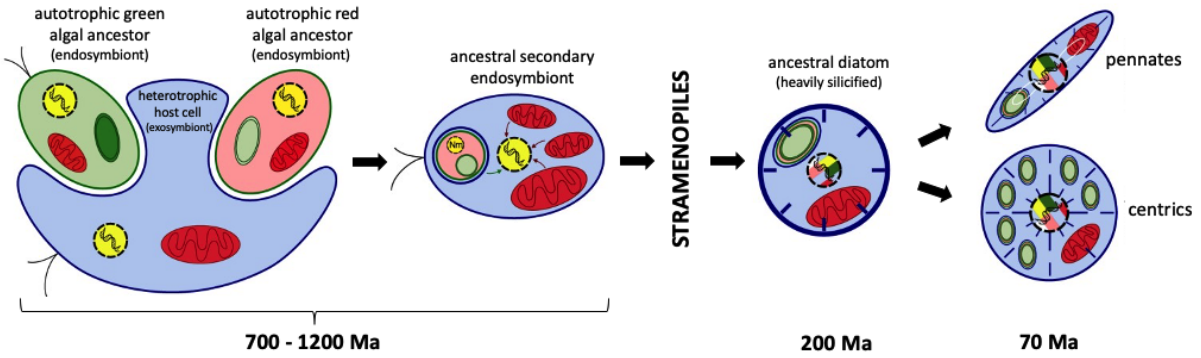

Figure 1.1.1: Schematic representation of diatom evolution with an approximate timeline. Modified from Benoiston et al., originally by Bowler et al. [9, 14].

Genome sequencing of the centric diatom *Thalassiosira pseudonana* and the pennate diatom *Phaeodactylum tricornutum* shows a high diatom diversification, as only 60% of the encoded proteins are present in both genomes [12]. The diversification is believed to be a result of horizontal gene transfer, transposable element mobilization, and gains and losses of exons and introns. Additionally, there are documented genes of bacterial origin within the diatom genome. These genes have no origin from a particular bacteria species, but appear to be derived from many bacterial genera [11, 12, 15].

Unicellular phototrophic diatoms, Bacillariophyceae, are phototrophic and widespread as they exist in marine and freshwater environments, wherever sufficient nutrients and light are accessible [14, 16]. It is estimated that there are around 100 000 different species of diatoms, ranging in size from approximately 2 μm to 400 μm, and that they are both cosmopolitan and diverse [17]. These brown-colored organisms can exist as single cells, chains, or colonies, and either planktonic (free-floating) or benthic (attached to a surface) [18]. Diatoms are considered responsible for 20% of the total photosynthetic CO_2 fixation carried out on Earth and are thus of great ecological importance [15]. Diatoms also play a significant role in the biogeochemical cycling of carbon, nitrogen, iron, phosphorus, and silicon (Si) on Earth [14].

Cell wall biomineralization in diatoms has been studied for decades, but the knowledge is still fragmented. The frustule assembly is a complex process as many organic molecules, scaffold structures, and cellular components are involved [19, 20]. Current knowledge is that biosilica is created inside Silica Deposition Vesicles (SDVs). Interactions between the SDV and cytosolic factors like the cytoskeleton have been observed but not yet thoroughly investigated [19]. However, proteins with an endoplasmatic reticulum (ER) signal peptide (SP) domain and a transmembrane (TM) domain that span the SDV membrane are presumed to be participatory in such interactions [20, 21, 22]. A family of diatom-specific transmembrane proteins named silicanins was recently identified. The silicanins are hypothesized to be associated with the biosilica assembly based on response to Si-availability and predicted domains [23]. A further investigation of the role of silicanins in frustule assembly and its possible interaction with the cytoskeleton can give a better understanding of cell wall biomineralization in diatoms.

In order to know the potential of diatoms in industrial manufacturing, the relationship between the variation in diatom morphology, and how diatoms construct the surrounding cell wall, should be better understood. The expression of genes involved in biosilica assembly is likely coordinated, and specific sets of proteins may be participating in the assembly of differ-

ent substructures of the cell wall. Thus, the identification of structural intermediates and how they interact with other components can give a better perception of the process as a whole. This knowledge, combined with information on the diatom genome and genetics, will make it easier for future utilization of diatoms. With gene-editing tools, diatom species can be modified to produce a biosilica structure adapted to be a good fit for a specific area of application.

1.2 Thesis Objective

This thesis aimed to better understand how nanopatterned biosilica is created in diatoms, the potential of diatom frustules in biotechnological applications, and investigate the putative association between the silicanins, elements of the cytoskeleton, and frustule assembly.

This master thesis is divided in two, and consist of literature study and laboratory research. An overview of the typical morphological features of diatoms, how frustule assembly is related to the cell cycle, and an insight into the potential use of diatom frustules in biotechnological applications in biomedicine was achieved by conducting two literature studies on published research. The putative association between silicanin Tp23191 and frustule assembly and the impact of microfilaments and microtubules on frustule morphology were investigated with laboratory research. The aim of the experimental work is defined more precisely in Section 4.7, after an introduction of *in vivo* protein investigation, the diatom *Thalassiosira pseduonana* and current knowledge of silicalemma-spanning proteins and the role of the cytoskeleton in diatoms.

Chapter 2

Literature Review: Diatom Morphology and Frustule Assembly

This literature study aimed to get an overview of the current knowledge of the natural biosilicification process in diatoms. The review focuses on the physical frustule morphology among the two main diatom classes and how the biosilica formation is associated with the cell cycle in diatoms. Even though organic molecules play a significant role in the formation of biosilica structure, they are only briefly mentioned.

2.1 Classes of Diatoms and Frustule Morphology

Diatoms are found in a multitude of shapes and sizes [24]. The morphology is unambiguous for the same species and is thus used for diatom classification [8]. Scanning electron microscopy (SEM) images of four diatom species, belonging to different diatom subclasses, are shown in Figure 2.1.1. These images exemplify the wide variety of morphology found among diatom species. The diatom morphology is mainly dependent on the skeleton, the frustule, which encloses the protoplast. Centric diatoms have symmetry around a central axis, while pennates have an elongated shape and a bilateral symmetry [25, 26]. The predominant forms of centric diatoms (Coscinodiscophyceae) are radial centrics and polar centrics [8, 12]. Pennate diatoms are divided into two subclasses; araphid (Bacillariophyceae) and raphid (Fragilariophyceae) pennates [27]. The latter has a raphe, which is a slit [15, 28], from where the diatom secretes mucilage [12, 14, 25]. As a result, the raphid pennates can glide along surfaces or attach to substrates [12, 14], which can explain why centrics tends to be planktonic, whereas pennates often are benthic or attached to surfaces [16]. Centrics are mainly found in marine habitats, while pennates predominate in freshwater. However, species from the two classes are present in both environments [29].

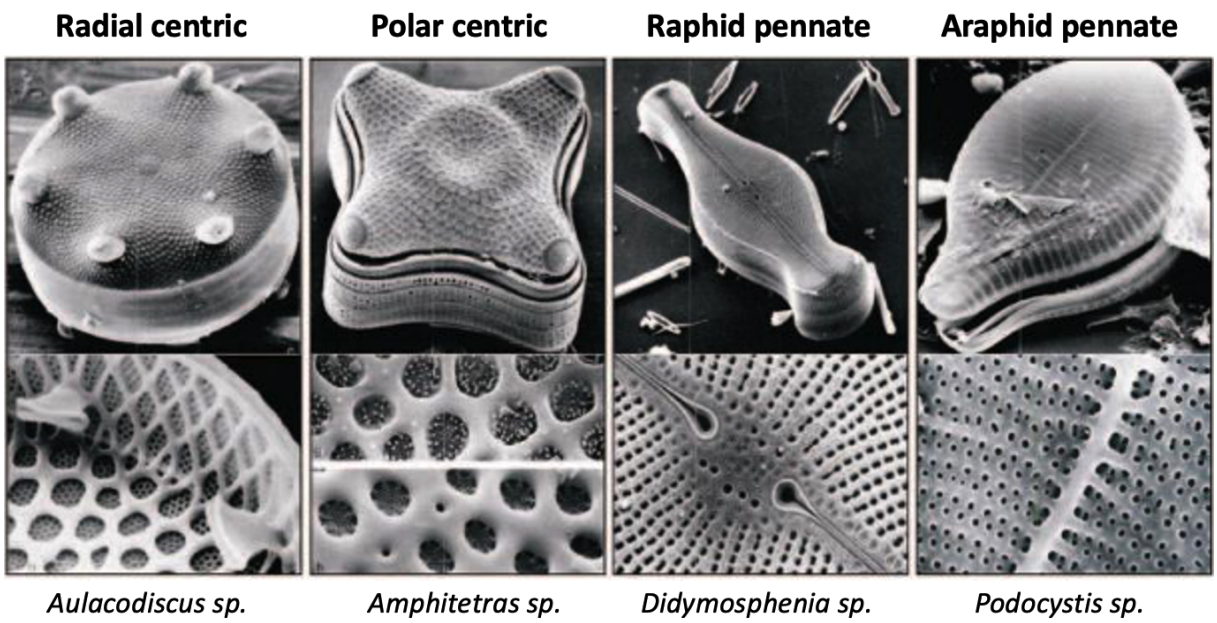

Figure 2.1.1: SEM images of four different diatom species illustrate the variety in frustule morphology among diatoms and within the classes of centric and pennate diatoms [8].

The diatoms got their name from the Greek word *diatomos*, which means ”cut in half”. Common for all diatom species is that the frustule is made of two thecas of identical structure [15]. An illustration of the cell wall composition is given in Figure 2.1.2.A. Both thecas are made of a valve composed of elaborate pore patterns and numerous thin girdle bands with incorporated pores in a uniform pattern [26]. The two thecas are constituted of either single- or double layer biosilica and differ in size as the largest, epitheca, overlaps the smallest, hypotheca. A pleural band at the end of each theca is coherent and connects the thecas. The valve is composed of several layers (foramen, cribrum, and cribellum), that each contains pores of different sizes, see Figure 2.1.3. This pattern is species-specific [22, 30]. The pores are surrounded by branched silica-structures, which is commonly referred to as an areola [22]. Girdle bands have a more straight-forward structure compared to the valves and are, in general, formed of split rings not fully connected. However, complete rings and scale-like girdle bands have been observed [31]. Amongst some diatom species, such as *T. pseudonana*, a bell-shaped section called the ligula, is present [32]. The girdle band located closest to the valve is called the valvocoupla [8].

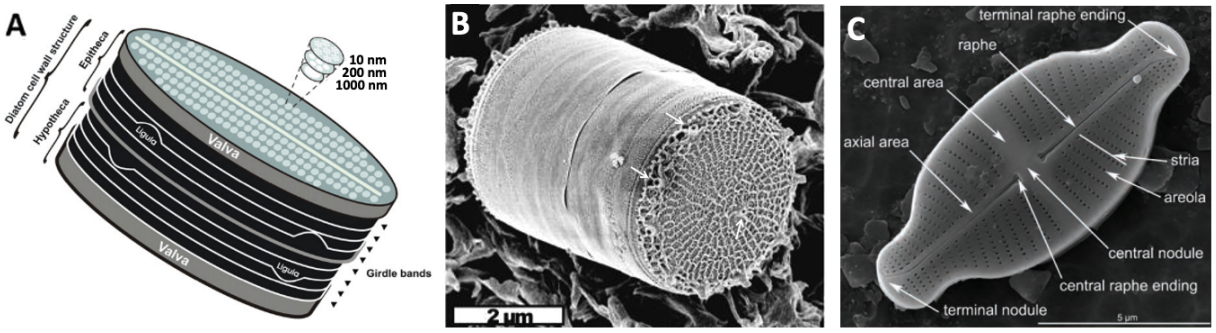

Figure 2.1.2: Diatom morphology. **A**) An illustration of the diatom cell wall constituted of two thecas, each composed of a valve, and numerous girdle bands. The valve contains layers with pores of different sizes. The largest theca, epitheca, overlap the smallest, hypotheca, in an overlap region with pleural bands [33]. **B**) SEM image of a centric diatom. The arrow located in the center of the valve denote the fultoportula, while the two arrows on the rim denote the two rimoportulae [32]. **C**) SEM image of a raphid pennate with characteristic pores and patterns for this class of diatom species [34].

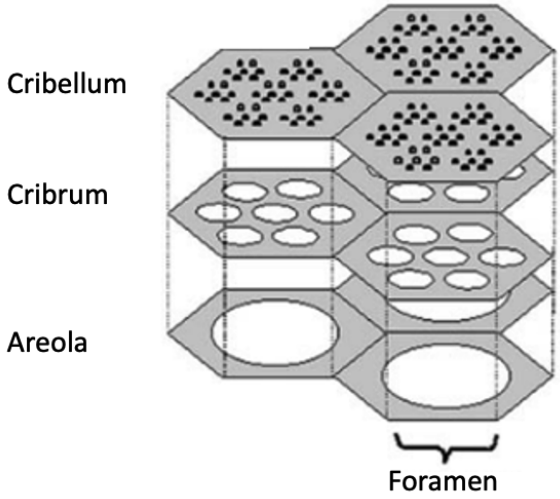

Figure 2.1.3: Schematic illustration of silica layers with pores of different sizes. The inner layer, areola, contains larger holes, called foramen. The cribrum layer contain smaller pores, while the cribellum has pores with the smallest diameter [30].

Despite the rib structure being conserved in diatom species, variations are found in the nanoscale structures [27]. In centric diatoms, branches of biosilica are spread out from the middle of the valve. A large pore, fultoportula, is generally located offset from the center. As a result of genetic variations, a varying number of fultoportulae have been detected. Numerous pores, rimoportulae, are located between the ribs on the edge of the valve [35]. An SEM image of a centric diatom with several rimoportulae and a futoportula is given in Figure 2.1.2.B. Pennate cell walls have an elongated shape, and bilateral symmetry, with a central nodule (CN) consisting of stored silica and a longitudinal slit, called a sternum. The sternum structure is different for araphid and raphid pennates [36]. Some pennates have areolae, which contains several elongated oval pores positioned in a row that forms a stria [37]. Figure 2.1.2.C. shows an SEM image of a raphid pennate where the raphe is visible. The raphe usually spans the length of sternum, but can also be localized on the side or along the center of the valve [37].

2.2 Biosilicification

The formation of biominerals is observed in all taxonomic kingdoms [3, 4]. Biosilicification, the uptake of soluble Si and transformation into a solid phase of silica [7], was first documented in diatoms by Lewin in 1954 [38]. Research from the last 70 years has provided a better understanding of diatom biosilicification. Orthosilicic acid, $Si(OH)_4$, is the predominant form of silica in aqueous environments [19, 39]. At high concentrations, the uptake is a result of diffusion transport, while specific silicic acid transporter proteins (SITs) facilitate the uptake in situations with low concentrations [19, 40]. Based on the varying rate of Si uptake, it is likely that the uptake is cell cycle dependent [41, 42]. The silicic acid transport mechanism within the diatom cell is currently unknown. Nevertheless, orthosilicic acid is brought into SDVs where amorphous silica, SiO_2, is created [19]. As illustrated in Figure 2.2.1, each individual SDV is surrounded by a lipid bilayer membrane, the silicalemma. The SDV is positioned close to the plasma membrane during frustule assembly, precisely opposite to the cell wall region where new biosilica is integrated [8, 28]. Partly because the SDVs have not yet been successfully isolated, it is difficult to determine the stepwise formation of biosilica and the intermediates involved [19, 25]. It is hypothesized that the organic matrix is trapped inside the SDV during silica formation, and serves as a template for patterned silica (Figure 2.2.1) [8, 43]. The organic matrix contains polysaccharides [44], long-chain polyamines (LCPAs) [45], and glycoproteins. After the intracellular silica synthesis is complete, the biosilica, which contains silica and the organic matrix, is exocytosed and deposited on the cell wall surface [8, 43]. The organic material prevents the frustule from degrading, and facilitate molecular transport across the cell wall [23].

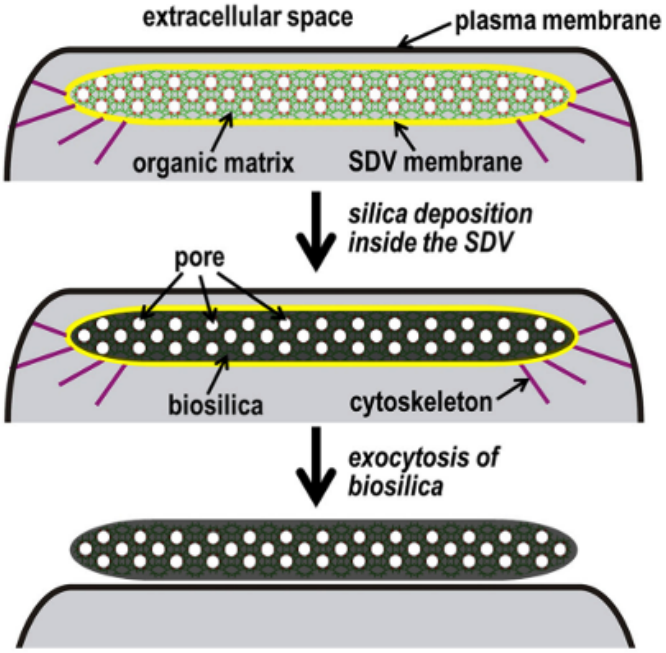

Figure 2.2.1: Biosilicification inside the SDV. A patterned organic matrix inside the SDV is believed to serve as a template for silica deposition, and the biosilica is deposited on the cell surface through exocytosis [43].

In the last fifteen years, there has been an increase in research on the implementation of inorganic silica into the surrounding cell wall [8, 25, 31]. Previous biochemical [46], genomic [11, 47], proteomic [48], and transcriptomic [23, 49, 50] approaches have identified several proteins such as silaffins [51], cingulins [52], and silacidins [53] with functions related to biosilica formation, and silaffin-like proteins [23], silicalemma associated proteins (SAPs) [54], and silicanins [23] putatively involved in biosilica formation. Pleuralins [45], and frustulins [55] have also been characterized, but these protein families have not shown functions related to the biosilica formation. A pentalysine cluster with non-consecutive lysines (KXXK, KXXK or KXXXK motif), is believed to promote silica targeting, as it is present in many of the protein families putatively involved in frustule formation, including silaffins and cingulins [19, 43]. However, this motif is not present in silicanins, silacidins, and SAPs, suggesting that these families are not directly involved in the initiation of silicification, or that the silica targeting is due to currently unknown motifs [19, 54].

Three different scales of biosilica structures are confirmed in diatoms. These are nanoscale, mesoscale, and microscale [28, 35]. The nanoscale involves initial polymerization of orthosilicic acid, [26, 35], while mesoscale predominantly is the organization of the polymerization product to form intermediate-sized silica structures, including ribs and larger pores. Microscale is the overall construction of the valve and girdle bands within the SDV [20, 22, 32]. Different nano- and mesoscale patterns are present within the same diatom species, and these scales are independent of the structure and size of the mesoscale pattern. Also, both random and ordered structures have been observed [56], and frustule formation includes both bottom-up and top-down approaches. The bottom-up approach uses small molecules to form larger-scale structures, and this approach has been observed during the creation of nanopatterned biosilica. The top-down approach creates large-scale structures before the fine details are generated and are typically involved in the formation of the pattern of biosilica on the mesoscale. It has been suggested that both approaches are highly conserved among diatom species and are partly responsible for the wide variety of existing frustule morphologies [20, 22].

2.3 Frustule Assembly Coupled to the Diatom Cell Cycle

Each species has its specific order of events, leading to the creation of an infinite number of frustules with a uniform pattern. The genetically encoded biomineralization process in diatoms is directly related to the cell cycle, as valves are created in valve SDVs, and girdle bands are created in girdle band SDVs at different cell cycle stages [8]. Cell expansion occurs during frustule formation, and both continuous and discontinuous expansion have been detected among different species [31]. A typical diatom cell cycle is illustrated in Figure 2.3.1. As the first step, the cell enters the S phase where DNA is synthesized, followed by a growth phase, G_2. In G_2, two valve SDVs are formed on each side of the newly created plasma membrane (Figure 2.3.1, stage 2). Valve SDVs gradually expand during biosilica formation and are deposited in the cleavage furrow by exocytosis when the valve in each daughter cell is fully developed (Figure 2.3.1, stage 5). In the M phase, the two sets of genomes are separated, and the cell reaches interphase, where a next growth phase, G_1, occurs. During G_1, girdle band SDVs are formed adjacent to the already existing girdle bands, and new girdle bands are created until the cell is outgrown (Figure 2.3.1, stage 7). The cell cycle is complete when the valvocoupla has been created (Figure 2.3.1, stage 9) [8]. The timing of girdle band formation varies between different species. Most species have girdle band assembly after cytokinesis, but observations

have shown that some species such as *T. pseudonana* have girdle band assembly both before and after cytokinesis [25, 28, 31, 57, 58].

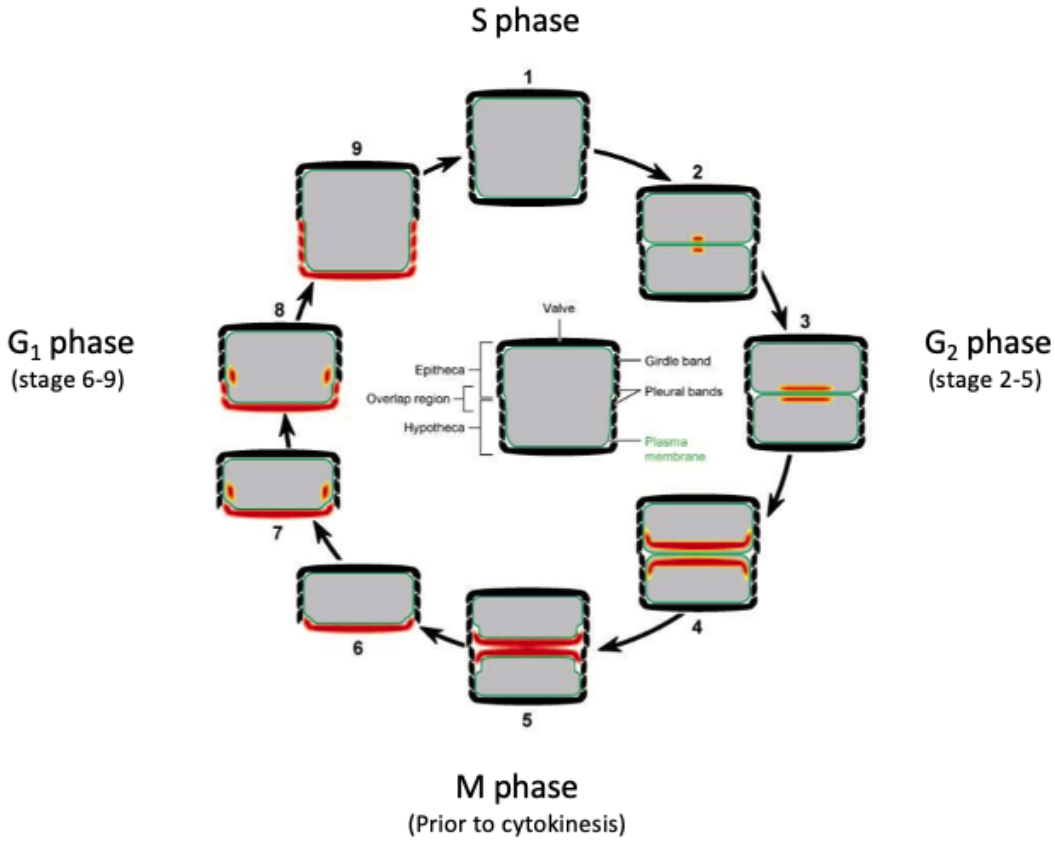

Figure 2.3.1: A general diatom cell cycle with the different phases. The centered cell illustrates the diatom cell wall, composed of two overlapping thecas. **1**) A fully outgrown diatom containing its maximal number of girdle bands where DNA replication has been initiated. **2-4**) Biosilica (red) is formed inside valve SDVs, (yellow) within each of the newly formed plasma membranes. The SDVs are expanding during this process. **5**) Fully developed valves are exocytosed prior to cytokinesis. **6**) Newly formed daughter cell. **7-9**) Girdle band SDVs (yellow) are formed, and new girdle bands are synthesized until the cell is fully outgrown, ending with the creation of pleural bands. Figure modified from Kröger et al. [8].

As a result of new daughter cells being formed within the thecas of the original cell, and hypothecas are created, the average cell size in a diatom population will gradually decrease. This is known as the MacDonald-Pfizer rule [8]. When the cell size reaches a certain minimum size, the cell becomes competent to undergo auxospore formation [24, 59]. Most diatom species undergo auxospore formation followed by sexual reproduction, but this reproduction pattern is not consistent for diatoms. Among centrics, the predominated sex is oogamous with flagellated male gametes. Within pennates, a variety of different mechanisms have been detected, such as anisogamy, isogamy, and automixis [16, 60]. Common for all is that the auxospore restores to its initial size. However, this reproduction phenomenon has not been detected in all diatom species. Some species, such as *T. pseudonana*, have flexible girdle bands, which makes further cell expansion possible, resulting in consistent cell size within the specific diatom population [57].

2.4 The Assembly of Valves

The diversity of the diatom valve structure is enormous, and the assembly of valves has been examined in several species, both centrics [28, 30, 35, 61] and pennates [28, 58, 62, 63]. As both *T. pseudonana* and *P. tricornutum* have often been used as model organisms for the investigation of cell wall biomineralization in diatoms, the following explanation of the general assembly of valves are based on these species.

In centrics, the formation of valves begins at the pattern center [28]. The pattern center is also referred to as the primary silicification site (PSS), and it is believed that its position is determined by the microtubule-organizing center (MC), a part of the cytoskeleton [28]. The following model is suggested by Hildebrand et al. [35], and is based on the stepwise valve assembly in *T. pseudonana* which is illustrated in Figure 2.4.1. In some centrics, included *T. pseudonana*, valve assembly starts with the creation of a hyaline ring called annulus. From the hyaline ring follows an expansion in the two-dimensional plane (x/y plane). This primary structure is known as the base layer (Figure 2.4.1.A-B) [19, 25, 35]. The base layer is fully developed during the intermediate stage of valve formation, and the valve is very flexible at this stage [57]. Ribs are extended from the center, and precursors of the fultoportula and rimoportulae are created (Figure 2.4.1.C). After initial deposition, a three-dimensional structure is developed as silica is deposited in the z-axis direction, and the interconnected silica pattern is created. The SDV exhibits a sidedness, which results in the deposition of silica only on the distal side (Figure 2.4.1.D) [35, 56]. This mechanism of expansion is detected in other centrics, but there are exceptions [35]. At this stage of the valve assembly, the rim is developed with pores, and the central region becomes firm [8]. It has been observed differences in rib structure and branching among different species, suggestively because different organic components are involved as a result of genetic variations [56]. The silica pattern created in the z-plane usually varies from the silica pattern in the base layer. In *T. pseudonana*, the base layer has a branched network of silica, while spherical silica particles dominate on the distal surface [35].

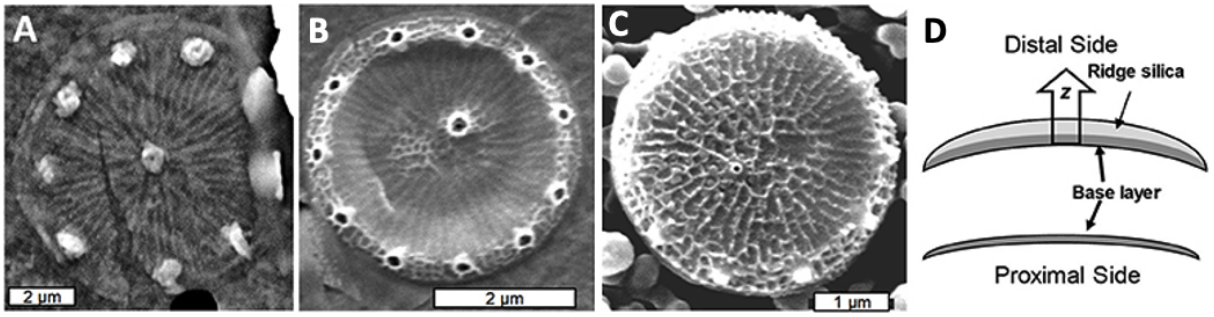

Figure 2.4.1: Valve assembly in *T. pseudonana*. **A**) SEM of base layer. **B**) Illustration of the first expansion (in x/y-direction) which occurs during base layer formation. **C**) Intermediate stage of valve formation with visible fultopulta and rimoportulae **D**) Complete valve. **E**) Illustration before and after expansion in z-direction. It results in a robust structure [19].

Studies have shown that in most pennates, the distal valve is created first, followed by proximal valve formation. *Nitzschia alba* is an exception, as the opposite order of assembly has been observed [56]. The pennate diatom *P. tricornutum* has three different morphologies, but biosilicification is only present in oval cells. Despite the unusual morphological properties, this species is the model organism for valve creation in pennates. Transmission electron microscopy

(TEM) images of a valve assembly in *P. tricornutum* are shown in Figure 2.4.2. Vartanian et al. suggest that valve synthesis in pennates starts with the creation of a "π"-like structure, which is the precursor of the CN. The sternum is further developed, and amongst raphid pennates, also the raphe is developed [56, 64]. A longitudinal rib appears on one side of the "π", and it twists and turns back. This is followed by the initiation of the second rib at the opposite side [64]. During intermediate phases, the raphe and sternum thicken [64]. Additionally, first-order branched ribs appear perpendicular to the sternum, and areola and other valve elements are formed. When the valve is fully created, it is exocytosed from the SDV and deposited on the cell wall [58].

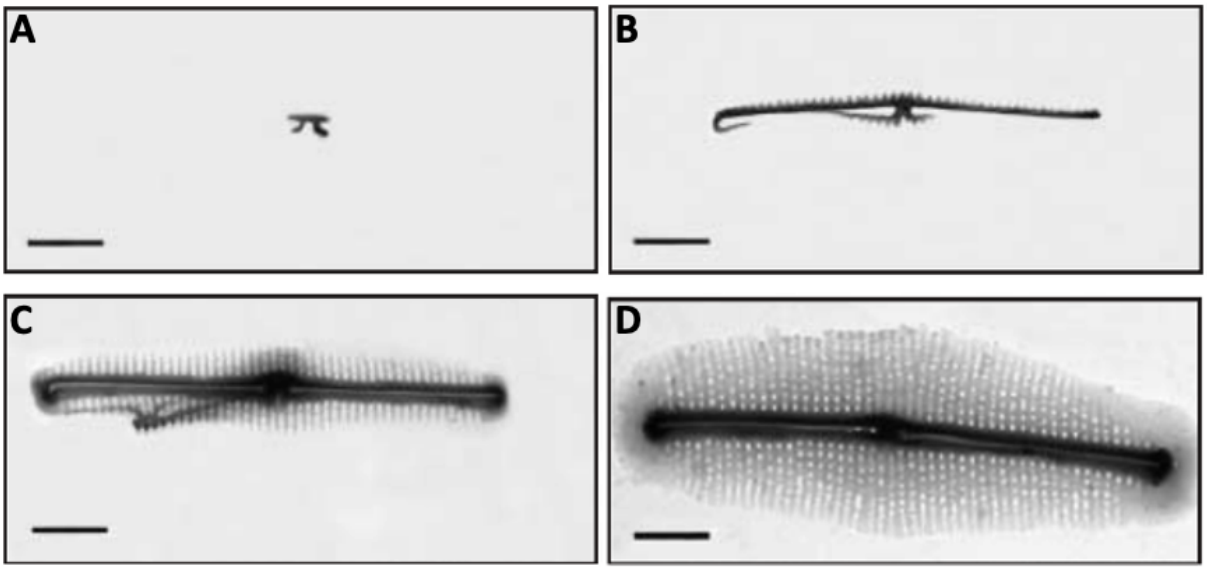

Figure 2.4.2: TEM images of a valve assembly in *P. tricornutum*. Scale bars 1 μm. **A**) A "π"-like structure appears in the early stages that is the precursor of the CN and controls the spatial organization of the sternum. **B**) The sternum and the raphe is developed, starting with the appearance of longitudinal ribs. **C**) The ribs have turned, and the raphe slit is enclosed at the CN. First-order branched ribs have appeared. **D**) The valve pattern is thickened, and the characteristic morphology of the species is visible. Pictures modified from Vartanian et al. [64].

2.5 The Assembly of Girdle Bands

In comparison to valve formation, the assembly of girdle bands has been little studied. Girdle bands are not as complex as the valves, and they are thinner and smaller in size, which makes them relatively transparent to electrons. Consequently, imaging of girdle bands with high resolution, such as TEM and SEM, are challenging [61]. The girdle band assembly has not been fully characterized, but the main structure has been examined. Girdle bands in both centric diatoms and pennate diatoms have complex geometric shapes and overlap each other [56]. Atomic force microscopy (AFM) imaging of girdle bands has revealed that the biosilica occurs on three different scales: nano-, meso-, and microscale, similarly as observed in valves [61]. Girdle band formation in the centric *T. pseudonana* has been imaged by Hildebrand et al. with ion-abrasion scanning electron microscopy (IASEM), see Figure 2.5.1 [32]. Based on findings from IASEM, Hildebrand et al. manifested that girdle band SDVs enriches the entire periphery of the cell during the assembly of girdle bands (Figure 2.5.1.A-B). The girdle bands are

assembled one at a time, exocytosed, and placed in an overlapping pattern adjacent to already existing girdle bands (Figure 2.5.1.C-D) [61]. The cell expands as new girdle bands are created until the terminal girdle band, the pleural band is synthesized, and the thecas are connected [8]. Generally, in diatom species, the ends of girdle bands are located on the exact opposite side of the lingula located in the same band during girdle band assembly. However, this is not the case for *T. pseudonana*, which instead has a relatively undefined border, with staggered lingula and girdle bands [35]. In contrast to the valve assembly, the silicalemma is not firmly attached to the silica inside girdle band SDVs. Thus, Hildebrand and coworkers suggested that organic materials are involved in the shaping of girdle bands [32]. Microfilaments of approximately 7 nm have been observed at the edge of a forming girdle band, at the same place where initial silica deposition later was present (Figure 2.5.1.E-F). This observation led to the assumption that microfilaments are involved in girdle band formation.

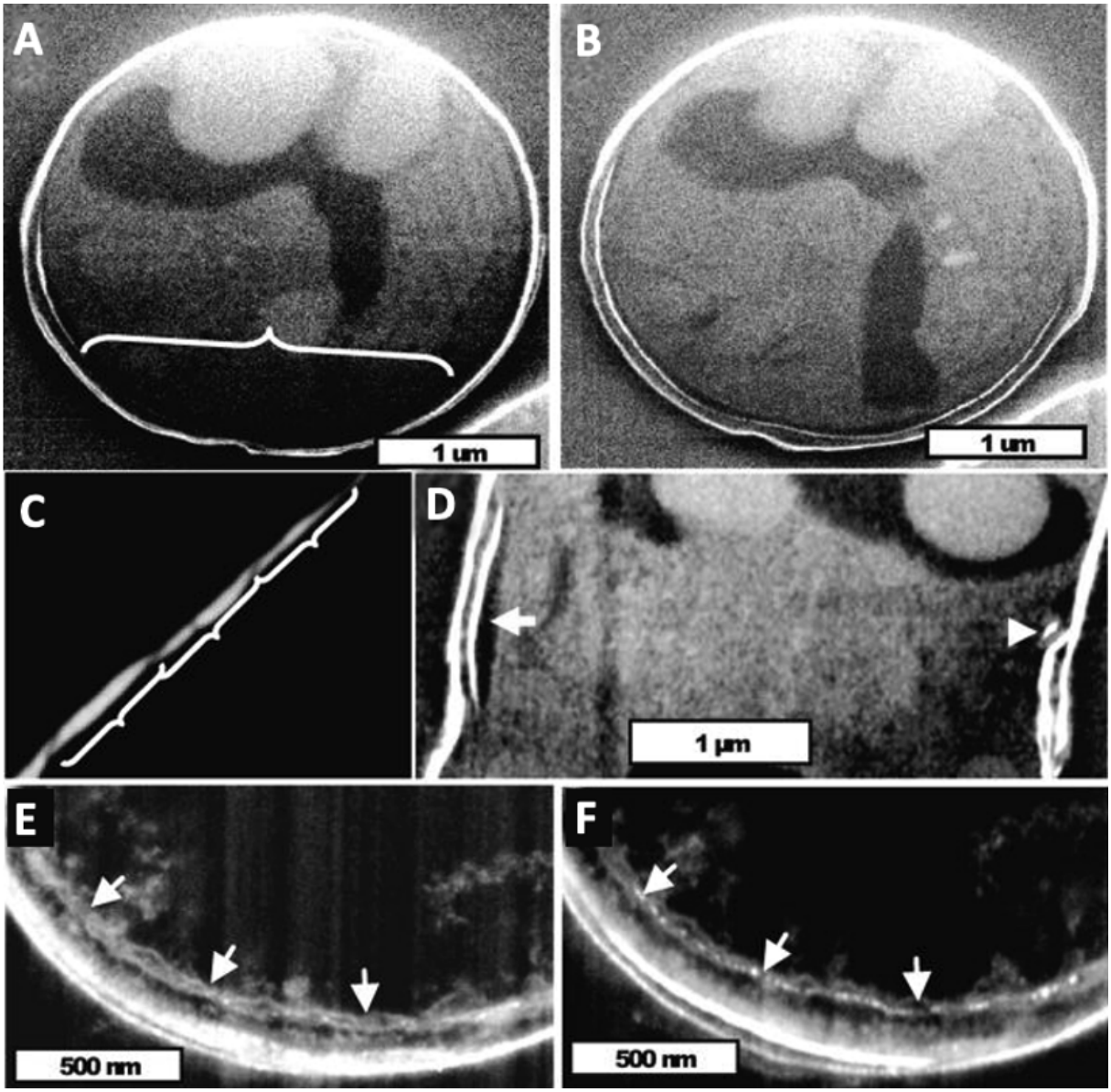

Figure 2.5.1: Visualization of girdle band SDV and associated microfilaments during girdle band assembly in *T. pseudonana*. Images from with IASEM. **A-B**) Valve plane section through a cell. **A**) Girdle band SDV is denoted with a bracket, and some silica inside the SDV is visualized on the left. **B**) More silica is present in the girdle band SDV. **C**). Cross-sectional image of the theca, visualizing three overlapping girdle bands. **D**) Girdle band view of newly formed girdle band and the associated girdle band SDV (left arrow), and a newly forming girdle band on the other side (right arrowhead). **E**) Microfilaments (arrows) approximately 7 nm long putatively associated with girdle band formation. **F**) The material is more electron-dense, which indicates that initial polymerization of silica has occured (arrows). Microfilaments were previously present at the same location [32].

Chapter 3

Literature Review: The Potential of Diatom Frustules in Biotechnological Applications

Biosilica from diatoms is considered as a promising candidate for a wide range of applications. This literature review focuses on the favorable properties of diatom frustules, general immobilization strategies, and the potential use of diatom frustules as biotechnological applications in biomedicine.

3.1 Sources of Biosilica from Diatoms and Potential Areas of Applications

Biosilica can be extracted from either live or dead diatoms. Diatomaceous earth (DE) silica, also known as diatomite, is the sediment from diatom fossils [65]. DE silica is chemically stable [66], and consists of amorphous silica, SiO_2, with trace amounts of organic components and metal oxides due to environmental impurities [67]. DE silica is highly fragmented and heterogeneous, as it contains of biosilica from many different diatom species [68]. The advantage of using DE silica for high-scale production is the availability in large quantities at low cost [69]. DE silica is currently used in a wide range of industrial applications, such as an additive in toothpaste, cosmetics, construction materials, paints, and filtration aids [69, 70]. Published research show the potential of DE silica in biomedicine as biocarriers for drug delivery [65, 71, 72], targeted delivery of small interfering RNA (siRNA) to cancer cells [67, 73], magnetically guided drug microcarriers [74], and as elements in biosensing devices [75]. The disadvantages of DE silica is mostly related to its chemical impurity and inhomogeneous structures of biosilica [68].

Monospecific diatom cultivation is an alternative source of natural biosilica. The use of frustules derived from diatom cultures is advantageous as it secures high purity and monodispersity [68]. The frustule pores do not scale with the cell size but are more or less constant [76]. Hence, the diatom species can be selected based on preferred pore size, pore shape, and frustule size. Diatoms are dividing exponentially, and rapid reproduction makes it possible to produce uniform nanopatterned biosilica in large quantities in a short time. Diatoms are self-replicative [27], and require only light and a minimum of nutrients for optimal growth [65]. As only a small quantity of the diatom must be shipped to the manufacturing company, the shipping costs can be reduced

to its minimum [77]. Many biotechnological applications have been proposed, explored, and tested with diatom frustules in the last twenty years - ranging from solar cells [26], batteries [26, 78], and electroluminescent devices [26], to molecular and particle separation [79], microscale gas-sensing [80], and optical sensors [81, 82]. Additionally, a wide range of articles and reviews regarding the potential of diatom frustules in biomedicine have been published.

3.2 The Potential of Diatom Frustules in Biomedical Applications

Diatom frustules are highly mesoporous, mechanically resistant, non-toxic, and thermally stable [83]. The reactive surface opens for great opportunities for surface functionalization and chemical modifications [70]. The general strategies for immobilization of biomolecules on diatom frustules and examples of biomedical application areas are illustrated in Figure 3.2.1. The high surface area, high permeability, and a large number of reactive silanol (Si-OH) and silanolate ($Si\text{-}O^-$) groups located on the cell wall surface makes diatoms especially suitable for immobilization [68, 83, 84]. Adsorption, encapsulation, and covalent binding are the three main types of *in vitro* immobilization of biomolecules on diatom frustules. The reactive groups enable adsorption of proteins by non-covalent binding with hydrogen bonds and Coulomb interactions with silanol and silanolate groups, respectively [8, 85]. As a result of the non-covalent binding being reversible, the protein is likely to detach from the surface. In applications where desorption is unfavorable, encapsulation is a good alternative. This method involves coating with the adsorbed protein with a nanoscale layer of, for example, silica or titania [68, 86]. Pre-treatment of frustules is necessary to enable the covalent binding of different biomolecules to the biosilica. Chemical treatment can generate controlled and irreversible attachment of bioactive molecules and antibodies through covalent binding [27].

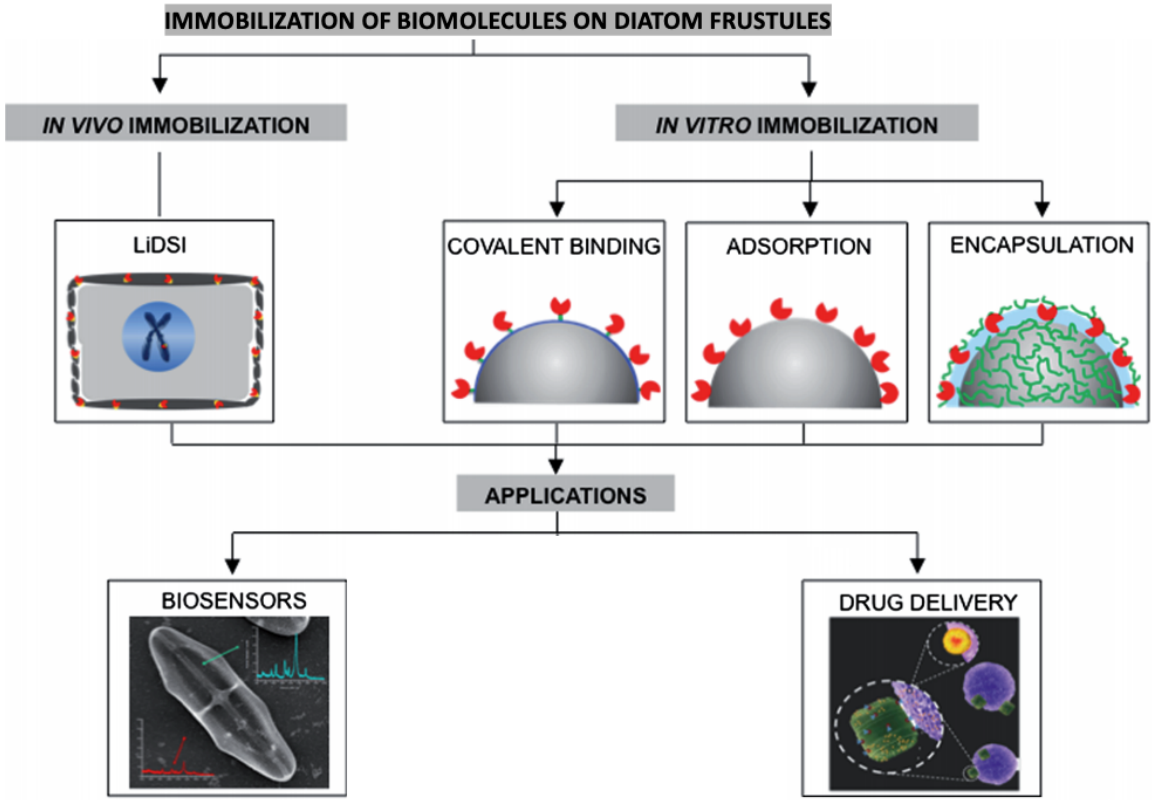

Figure 3.2.1: Illustration of possible methods for immobilization of proteins on diatom frustules, and examples of biomedical application areas. Modified from Kröger et al. [68].

Genome sequencing of diatom species has made it possible with *in vivo* immobilization of biomolecules through genetic engineering. Poulsen and coworkers were the first to use genetic engineering for diatom frustule immobilization. They developed an approach called living diatom silica immobilization (LiDSI), which is based on genetic manipulation of the biosilica assembly in *T. pseudonana*. The method is illustrated in Figure 3.2.2. By creating a fusion with the gene of interest and a gene encoding a protein that is naturally incorporated into the cell wall, the desired protein will be genetically tailored in the biosilica [87]. This type of *in vivo* immobilization is beneficial, as pre-purification of the proteins is unnecessary, and the proteins will be naturally integrated into the organic matrix of diatom biosilica with high mechanical stability [68]. Additionally, Poulsen et al. demonstrated LiDSI with a fluorescent protein and a simple enzyme that functions without cofactors or post-translational modifications [87]. As a continuation of the work by Poulsen et al., Sheppard and coworkers showed that LiDSI is compatible with enzymes with the activity requirements FAD, heme-groups, glycosylation, Ca^{2+} and Cu-ions [88]. Unfortunately, the unknown transport mechanism and pathway to the SDV during frustule assembly impose limitations on the functionalization of immobilized molecules. Thus, the LiDSI is still not compatible with functional immobilization of proteins that require cofactors, oligomerization, or post-translational modifications that are not provided during the intracellular unknown transport pathway to the SDV [68, 88]. Due to the lack of antibodies as binders in the biosilica, Ford et al. genetically engineered *T. pseudonana* to create antibody-functionalized frustules, such that chemical and biological agents can attach to artificial antibodies in the biosilica [89].

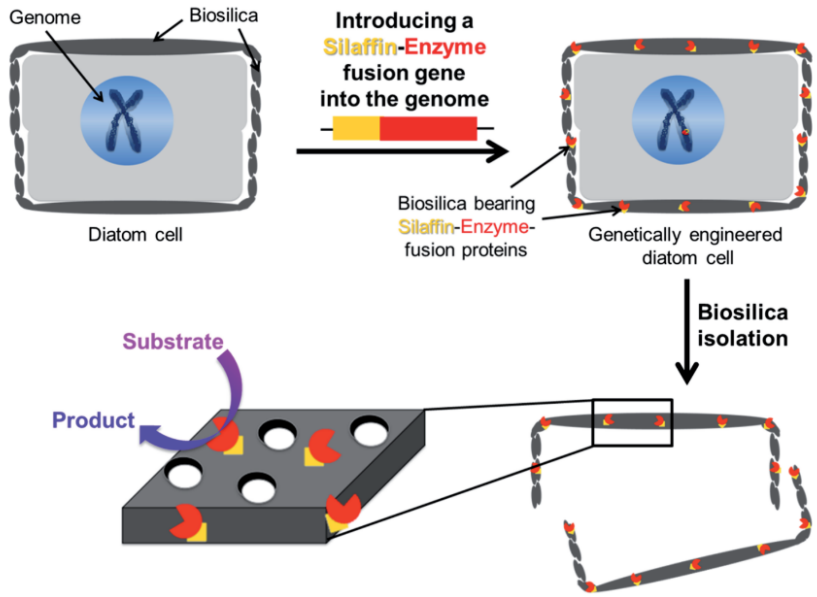

Figure 3.2.2: An illustration of the LiDSI method. By integrating a fusion gene into *T. pseudonana*, the silaffin-enzyme fusion protein (in yellow and red) is integrated into the biosilica during frustule assembly. The immobilized protein on the biosilica can be further used in a variety of applications [68].

A disadvantage of the LiDSI method is that only a small amount (0.1 % wt/wt) of the fusion protein is incorporated in the biosilica. This is about ten times lower than the yield observed with *in vitro* immobilization with encapsulation [88, 90]. Until recently, fusion proteins with silaffin or silaffin-fragments have been used for the incorporation, and proteins have been incorporated in all parts of the cell wall. Kumari et al. have successfully conducted regioselective immobilization of fusion proteins with LiDSI. This was done by fusion of enzymes to proteins that are naturally present at specific regions in the frustule. More specifically, they used Silaffin-1, which have only been observed in the valve region, and different cingulin proteins that are located in the girdle bands of *T. pseudonana* [91]. This work demonstrates the importance of characterization of proteins associated with the frustule assembly. To date, the LiDSI method is only established for *T. pseudonana* [91], and further development of the method to make it compatible with other diatom species is advantageous, especially since many species with different morphologies already have been genome sequenced [92]. To illustrate the potential of diatom frustules in drug delivery systems and as biosensors in immunodiagnostics, a selection of published research is described in the following sections.

3.2.1 Diatom Drug Delivery Systems

The drug delivery systems currently in use are effective but have limitations such as degradation, poor solubility, and short drug release [93]. Higher drug dosages can compensate for the limitations, but this is disadvantageous as it can result in higher toxicity [93]. Diatom frustules as biocarriers hold great potential mostly due to their uniform structure of pores, and as they are biocompatible, chemically inert, and non-toxic [83].

The first research on diatoms as potential drug carriers loaded DE silica with drugs. Even though the drug release mechanism was not investigated in detail, prolonged drug release properties were observed [65, 74, 94]. This property was further investigated by Zang et al., who

used cylindric diatom microparticles for oral drug delivery of prednisone and mesalamine for gastrointestinal diseases. The drugs were loaded into the external and internal surfaces, the pores included, resulting in a controlled release of both drugs [72]. Moreover, Vasani et al. demonstrated antibiotic drug delivery with whole *Aulacoseira sp.* frustules. The frustules were pre-treated to obtain a controlled drug loading, followed by a controlled drug release of the antibacterial agent levofloxacin [95]. Based on previous research, it is known that surface modifications can control the release of both hydrophobic and hydrophilic molecules [71, 96].

Specific and optimally adapted targeted drug delivery is hard to achieve because of barriers like non-specific distribution and drug localization, resulting in high drug dosages, which increases the risk for side effects [83]. Silica particles are believed to solve these problems [97]. By utilization of DE silica with human epidermoid cancer cells (H1355) as target cells, Rea and coworkers were the first to accomplish targeted delivery of siRNA [67]. Diatom frustules have not yet been used [27], but the LiDSI method would most likely be beneficial for this area of application.

The combination of antibody attachment and drug loading is especially feasible for targeted drug delivery. Delalat et al. genetically engineered *T. pseudonana* for drug delivery to targeted tumor sites. LiDSI was used to incorporate the antibody-binding protein domains for immunoglobulin G (IgG) into the diatom cell wall such that further antibody attachment was possible. Moreover, hydrophobic drug molecules were encapsulated into cationic micelles and liposomes before loading onto the frustule [98]. Figure 3.2.3 illustrates the genetically engineered *T. pseudonana* with integrated drug molecules and antibody-binding domains, enabling the release of drugs and attachment of cell-targeting antibodies [98].

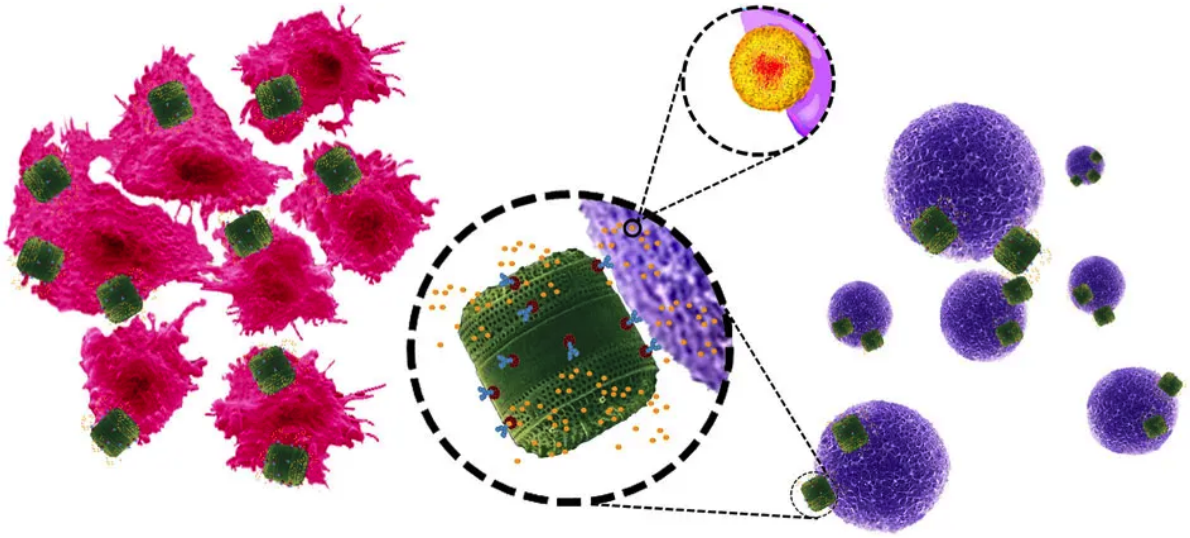

Figure 3.2.3: Genetically engineered frustule of *T. pseudonana* (green) with hydrophobic drug molecules encapsulated in liposomes (yellow) and incorporated antibody-binding protein domains (purple). Target cells (pink and violet) are selectively targeted and killed after being exposed to the biosilica particles [98].

3.2.2 Diatom Frustules as Biosensors in Immunodiagnostics

A biosensor is composed of a biological sensing element, for example, an enzyme, antibody, or a DNA molecule, with a transducer which detects and converts the signal into a physical quality [99]. Due to the optical features of diatoms, it is possible to use diatom frustules in optical biosensors [100]. When antibodies and ligands interact, photoluminescence is emitted, and the exact amount of antibody-ligand interaction can be measured. Frustules from the centric *Coscinodiscus concinnus* were chemically modified by De Stefano et al. such that selective bio-probes could be attached [82]. Wang and coworkers explored the potential of diatom frustules in optical sensors, and their capacity to increase the density of antibodies, with frustules from three different diatom species [81]. These studies combined confirmed that diatom frustules are furnished with extreme sensitivity, which makes them ideal for use in bio-chips and "lab-on-a-chip" sensors [81, 82].

Immobilization of biosilica makes it feasible to attach active biomolecules. Therefore, diatom frustules are especially suitable as elements in antibody arrays or applications used for immunodiagnostics [101]. For high quality and accurate measurements, it is necessary with a precise manipulation and arrangement of the frustule on the bio-chip [102]. Lin et al. have previously designed a biosensor assay with diatom-coating for the detection of cardiovascular biomarkers. The gold sensing sites were covered with *Coscinodiscus wailesii* before the biosensor was attached to the chip. The high cell wall surface enabled electrochemical detection of two inflammatory markers present at low concentrations in human serum [103]. The biosensor assay had a dynamic range of detection similar to other standard enzyme-linked immunosorbent assays (ELISA) [104]. A multilayered hierarchical array was constructed by Li et al. to achieve a high surface area for the attachment of antibodies. By stacking *Nitzschia soratensis* frustules into *Cosinodiscus argus* frustules, Li et al. showed that fluorescent intensities were significantly higher compared to assays with only one type of diatom frustules [102].

Cytokines is the collective term for signal molecules that mediates immunity and regulates inflammation. Several analyzation techniques have been developed for the detection of cytokines, but all have limitations [105]. An example is surface-enhanced Raman scattering (SERS) biosensing, which has limitations in signal detection [105]. The photonic diatoms can increase the signal intensity and facilitate Raman signal enhancement [76]. Among others, Yang et al. [106], Kong et al. [107], and Kaminska et al. [105], have previously demonstrated SERS-based immunoassay with diatom frustules. Yang et al. used chemical modifications to self-assemble plasmonic nanoparticles onto *Pinnularia sp.* frustules, while Kong et al. used *in-situ* growth to place plasmonic nanoparticles in pores of the diatom frustule [99, 107]. Kaminska et al. bound antibodies to reactive Si-OH groups on *Pseudostaurosira trainorii* frustules, as shown in Figure 3.2.4. Nanoparticles of gold and Raman reporters were used to detect interleukin in human plasma, resulting in a higher sensitivity of this immunoassay than other ELISA methods [105].

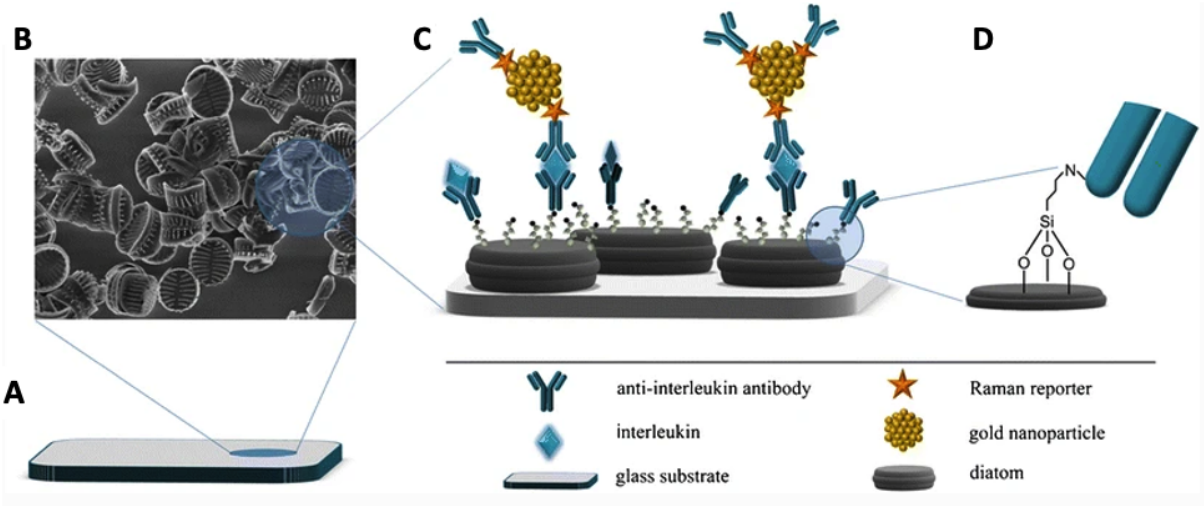

Figure 3.2.4: A SERS-based immunoassay. **A**) Modified frustules of *P. trainorii* attached to a glass substrate. **B**) SEM image of the glass substrate with diatom frustules. **C**) Schematic illustration of the immunoassay with antibody (anti-interleukin) attached to diatoms, which facilitates antigen (interleukin) attachment. Raman reporters and gold nanoparticles enhance the signal for detection. **D**) The antibody is attached to the reactive Si-OH groups on the diatom frustule [105].

3.2.3 Future Prospects

The use of diatom frustules in biomedical applications is a rapidly growing research front. Despite this, poor biodegradability of diatom biosilica in biological fluids has been detected. Poor biodegradability can lead to the accumulation of silica particles in unfavorable places within the human body. Nevertheless, the use of diatom frustules in biomedical applications is feasible, both by the independent and combined use of immobilization, modification, and biofunctionalization. Immobilization of other functional biomolecules than previously mentioned, such as peptide hormones, growth factors, and receptors, can be suitable for the further development of diatom frustules in biomedical applications [87].

Even though diatom frustules have a great potential considering drug delivery and as biosensors in immunodiagnostics, they are currently not used in any commercial products. Diatom biosilica has been classified as non-carcinogenic by the International Agency for Research on Cancer (IARC) but has no authorization for biomedical use [83]. *In vivo* studies, animal testing and clinical trials are crucial steps that must be completed before the applications can be legally approved for use in medical treatment and diagnostics. A full understanding of the biosilica assembly in diatoms would be highly advantageous for the further development of diatom-based applications, and genome sequencing has proven to be an important tool for this research. Moreover, identification and characterization of currently unknown intermediates can open up for a broader potential area of applications, not only within the field of biomedicine.

Chapter 4

Laboratory Research: The Study of Silicanin Tp23191 and the Contribution of the Cytoskeleton to Frustule Assembly in *T. pseudonana*

4.1 *T. pseudonana* as a Model Organism

As previously mentioned, the centric diatom *T. pseudonana* has been developed as a model species for the investigation of biosilica formation in diatoms. This species is especially suitable as valve expansion occurs, which prevents the population from decreasing in size. Sexual replication has never been observed, and auxospore formation has only been infrequently observed under normal growth conditions [48]. *T. pseudonana* was the first eukaryotic phytoplankton with a sequenced genome [57]. The 34.5 Mega base pair (bp) long genome is spread over 24 nuclear chromosomes, and a total of 11.242 genes are presumably within protein-coding regions [11]. Completion of the entire genomic sequence made it possible to combine genomic, proteomic, and transcriptomic approaches to identify cellular components involved in diatom biosilicification [35]. Thus, previous studies have detected the distinct stages of frustule assembly and described the corresponding silica morphologies [32, 35, 56, 61].

SEM and TEM images of *T. pseudonana* are shown in Figure 4.1.1. The average height is between 4-7 μm, and the diameter is approximately 4 μm [35]. Girdle bands are not complete circles but have an undefined border because of the ligula. Nanopores are present on the girdle bands, but the valvocoupla is ornated with more pores than the subsequent girdle bands (Figure 4.1.1.B). The valve is characterized by two types of ribs: costae and cross-connections. Costae are radiating from the center to the rim in a branched network (green lines in Figure 4.1.1.C), while cross-connections are short silica-bridges connecting neighboring costae (orange lines in Figure 4.1.1.C). The areola layer (red circle in Figure 4.1.1.C) with foramen pores, is shaped like a trapezoid and usually surrounds smaller cribrum pores [6]. Generally, one fultoportulae is located in offset from the center, and a varying number of rimoportulae are located on the rib. Based on observations, the average number of rimoportulae is 10 [6, 35].

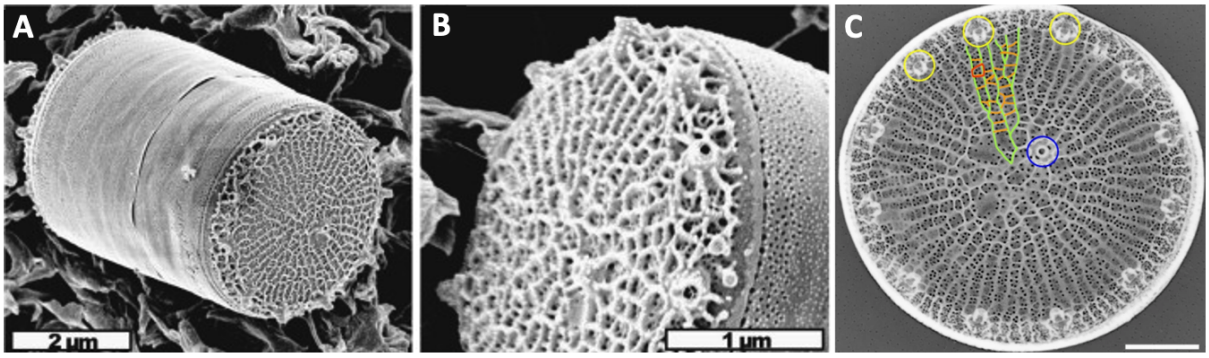

Figure 4.1.1: The *T. pseudonana* morphology. **A**) SEM images of the entire cell structure [32]. **B**) A close-up SEM image of the valve surface [32]. **C**) TEM image of valve surface where the main morphological features are colored for easier verification. Costa (green), cross-connections (orange) , areola pore (red), rimoportulae (yellow), fultoportula (blue) [6].

4.2 Analysis of Proteins *in vivo*

Fluorescent protein markers are beneficial for the investigation of dynamic responses and localization of proteins *in vivo*, as emitted fluorescence at a particular wavelength shows the presence of the fusion protein and can reflect the presence of the genomic DNA [108, 109]. When designing a fusion protein, the placement of the marker gene is crucial for optimal protein function. To minimize the risk of sterically hindered protein folding, and interference between targeting domains, the placement of the gene should be outside a functional domain [109]. mNeonGreen (mNG) is the brightest monomeric fluorescent protein discovered within the green and yellow part of the visible spectra. It is characterized by sharp peaks for excitation at 506 nm and emission at 517 nm, and can thus be detected with optical filters within this range [110]. Despite its sharp signal, mNG is affected by photobleaching, the underlying process where the fluorophore is converted to a non-fluorescent protein [111].

Plasmids are stable and will not interfere with genomic DNA within the organism [108]. Thus, they are often used as carriers of fusion proteins. pTpPuc3 made by Karas et al. contains a particular DNA sequence, CEN6-ARSH4-HIS3 (CAH), which is derived from yeast. Recent studies have proven that parts of the CAH cassette with low GC-content is essential for plasmid maintenance in diatoms due to its centromere functionalities [112, 113, 114]. Plasmid pTpPuc3 has two selectable marker genes, *KanR* and *NrsR*, that confers resistance to kanamycin (kan) in bacteria and nourseothricin (ntc) in diatoms, respectively.

A fluorescent-labeled gene placed on a plasmid under the same promoter as the similar gene within the genome will be translated into proteins whenever the gene is activated [108, 109]. Transgenic lines with integrated fusion protein will have two sets of genes; one gene localized in the genomic DNA and one fluorescence-labeled gene localized on the plasmid. Research has proven that overexpression of genes in different species may affect the total protein expression, by either increasing or decreasing the protein translation [115, 116]. Hence, the fraction of protein translated from the genes within the original genome is unknown, and biovisualization techniques can only reveal where the fluorescence-labeled protein is located.

4.3 Synchronized Cell Cycle Arrest by Si-starvation

Synchronized cultures of diatoms have proven to give novel insights into the frustule assembly related to the different stages of the diatom cell cycle [57, 117]. Moreover, identification of intermediates at different stages of the frustule assembly can give an insight into the underlying mechanism of how the species-specific silica pattern is created [35]. A Si-starvation/replenishment procedure for synchronization of *T. pseudonana* have previously been developed by Hildebrand and Frigeri. The Si-starvation causes the cells to arrest, and upon Si-addition, the cells progress synchronously through the cell cycle [57]. Two arrest points have appeared to be general among the different diatom species. The first is before G_1-S boundary, after girdle band creation, and the other is detected in G_2+M, during valve creation [57, 117, 118]. Synchronization studies have revealed that most cells arrest at the same stages, thus enabling characterization of events that occur at certain cell cycle stages. Based on observations, Hildebrand et al. have confirmed that the different steps in the cell cycle are well preserved among *T. pseudonana* cells, with the exception of G_1 phase. This phase can vary between 1-4 hours under optimal growth conditions among cells of *T. pseudonana* [19, 57].

4.4 Silicalemma Spanning Proteins

4.4.1 The Silicanin Family

A transcriptomic approach recently conducted by Brembu et al., led to the discovery of a diatom-specific transmembrane protein family, named silicanins, putatively associated with the biosilica assembly [23]. The silicanin family was identified by examination of gene expression in *T. pseudonana* at Si-starvation (shift-down) and replenishment (shift-up) under a light/dark regime. With full-genome oligonucleotide microarrays, dynamic responses to Si availability were detected and compared with previously published works. Approximately 21% (2,364 genes) of the *T. pseudonana* transcriptome was significantly regulated by Si availability, and three major gene clusters were identified. From one cluster of 94 genes, seven genes were identified that encoded proteins with a domain containing eight conserved cysteines. Further database searches identified 15 genes from *T. pseudonana* and 10 genes from *P. tricornutum*, including the already characterized Silicanin-1 (Sin-1, previously named SiMat7) [119]. Based on protein alignments, twenty-five silicanin proteins were identified and further divided into four subfamilies (Figure 4.4.1.A) [23].

All genes identified are predicted to have a similar construction as Sin-1. As illustrated in Figure 4.4.1.B, the SP domain and the protease cleavage site (RXL) is positioned at the N-terminal, eight conserved cysteine residues are located downstream for the RXL, and a TM domain is placed at the C-terminal. Most biosilica associated proteins previously characterized contain an RXL domain [46], and proteins associated with the ER contains an SP domain [51, 52, 53], both located at the N-terminal. The RXL domain indicates that the protein family is a target for protease activity, and the predicted SP domain implies a possible extracellular localization. Based on the predicted structure, the silicanins are most likely membrane-bound, with the C-terminal part localized in the cytosol. The expression profile of ten silicanins given in Figure 4.4.1.C shows a similar expression pattern with down-regulation the first hour after Si-replenishment [23].

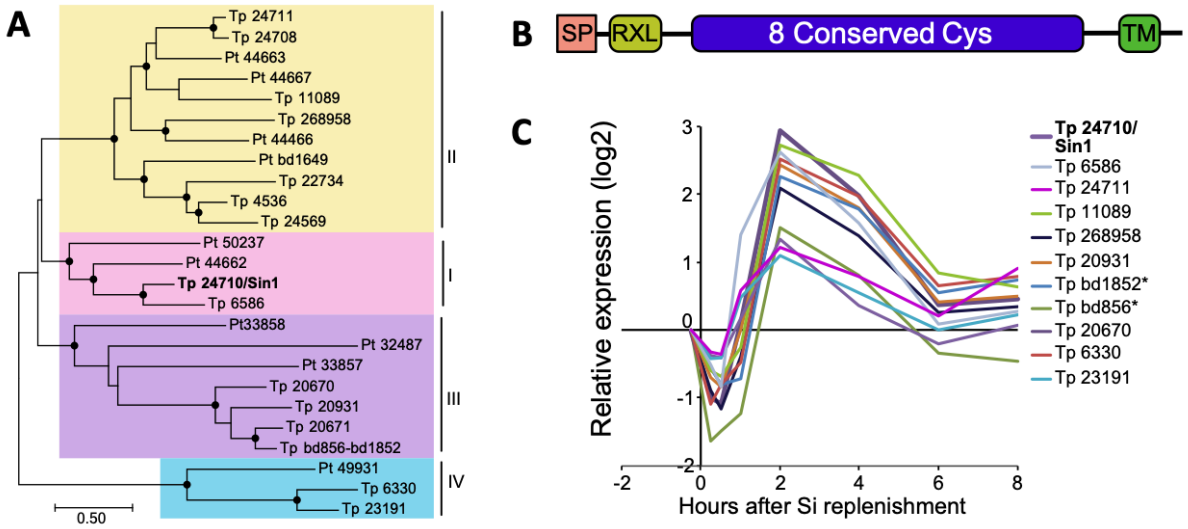

Figure 4.4.1: The silicanin family. **A**) Phylogenic tree with the 25 genes identified from *T. pseudonana* (Tp) and *P. tricornutum* (Pt). The genes are divided into four subfamilies based on protein alignment. **B**) Predicted domains. Signal peptide (SP) and a protease cleavage site (RXL) at the N-terminal. Eight conserved cysteine residues are located downstream for the RXL, and a transmembrane (TM) domain is located at the C-terminal. **C**) Expression profile of silicanin genes detected during a shift-up experiment. * are one gene and not two as annotated in the genome assembly [23].

Currently, Sin-1 is the only silicanin that has been characterized. Sin-1 is a type 1 transmembrane protein confirmed associated with LCPAs, the silicalemma, and the intracellular part of the SDV [119]. The composition of Sin-1 is shown in Figure 4.4.2. It is composed of 426 amino acid residues and contains a major region of asparagine and glutamine, referred to as the ”NQ-rich domain”. This region also contains 18 conserved cysteine residues [119]. Observations made by Kotszch and coworkers confirmed that the protein is silicalemma-anchored during biosilica assembly. Moreover, Sin-1 has an impact on frustule morphology. This knowledge was obtained by examination of *T. pseudonana Sin-1* knockout mutants [6]. The outline of girdle bands was similar to wild types, but valves among mutants had a simpler pore pattern. The combination of less mechanical robust frustules and the lack of hierarchical pore pattern proved that Sin-1 is but participatory in the biosilica formation in *T. pseudonana*, but not essential [6]. Based on these results, it is likely that a further investigation of the identified silicanins can be useful towards a better understanding of diatom biosilica formation.

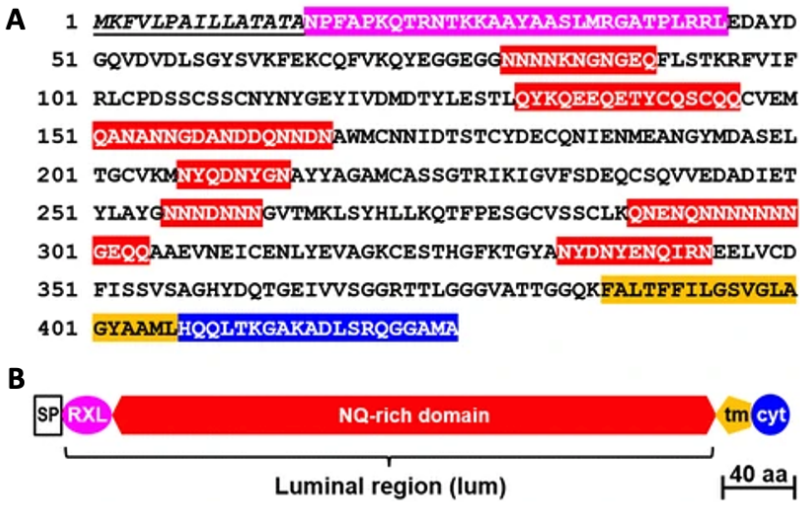

Figure 4.4.2: The composition of Sin-1 in the silicanin family. **A**) The amino acid sequence of Sin-1. **B**) Schematic illustration of Sin-1. The signal peptide (SP) is underlined, while the other domains are denoted specific colors similar to the schematic domain arrangement. Protease cleavage site (RXL), transmembrane (TM), cytosolic (cyt) domains [119].

4.4.2 Silicalemma Associated Proteins (SAPs)

Another transcriptomic approach with an analysis of *T. pseudonana* microarray data, found multiple silicalemma-associated candidate proteins with predicted SP and TM domains [50]. From this subset of genes, a new family of proteins was identified [54]. SAPs are mainly conserved in centric diatom species and have a similar predicted structure as the silicanins, with an extended intraluminal N-terminal region, and a short cytoplasmic sequence [54, 119]. The sequence domain conserved in other SAPs is located on the C-terminal side of the TM domain. Instead of an NQ-rich domain, SAPs are characterized by a serine-rich domain [54]. With *T. pseudonana* as a model organism, three SAPs with similar features were recently characterized. SAP1 and SAP2 have an extended intraluminal N-terminal region, and SAP3 are related to biosilica within the SDV lumen. The exact mechanisms of the SAPs are currently unknown, but an examination of frustule morphology in knockdown lines have confirmed their roles in *T. pseudonana* frustule morphology. Moreover, it is currently believed that SAPs have different functions [54].

Figure 4.4.3 illustrates how SAPs are integrated into the silicalemma and shows the putative interactions suggested by Tesson et al. [54]. Tesson et al. hypothesized that the serine residues on SAPs are phosphorylated, similarly like silaffins [120], and that these domains interact with orthosilicic acid, LCPAs, or peptide bound polyamines [54]. The cytoplasmic sequence of SAPs has not yet matched any sequences that interact with elements of the cytoskeleton [19]. Hildebrand et al. suggested that the silicalemma proteins may not be directly associated with the cytoskeleton but involved in multi-protein complexes that together are related to different elements of the cytoskeleton [19, 54].

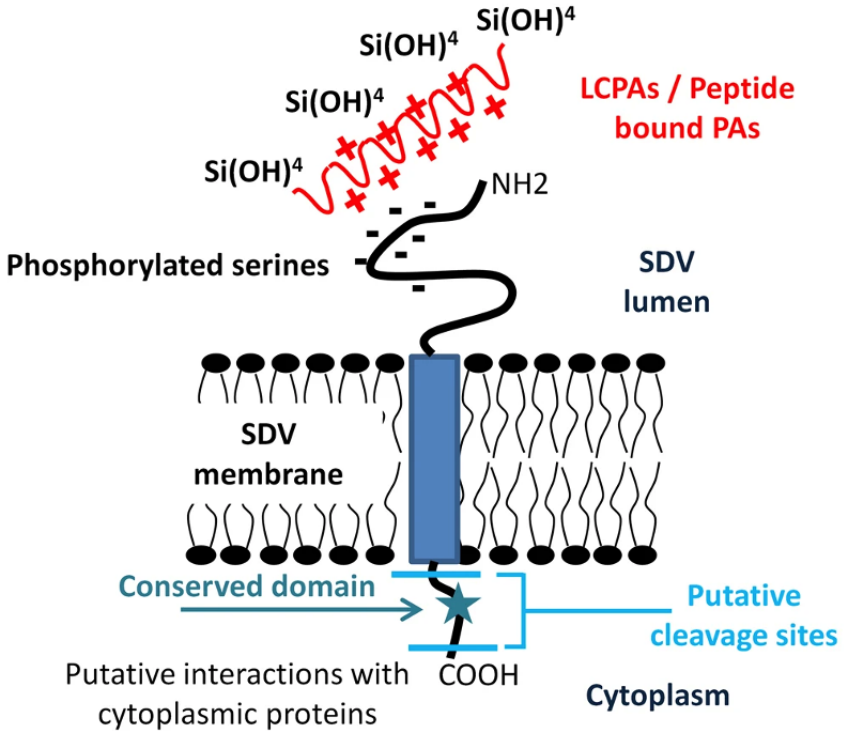

Figure 4.4.3: An SAP integrated into the SDV membrane, the silicalemma. The N-terminal is localized on the intraluminal side and the C-terminal in the cytoplasm. Hypothesized interactions between phosphorylated serines with orthosilicic acid ($Si(OH)_4$ and LCPAs or peptide bound polyamines (PAs) [54].

4.5 Previous Investigation of Silicanin Tp23191

Silicanin Tp23191, identified in *T. pseudonana* and placed in subfamily four, was investigated during the specialization project in 2019 [1]. A protein fusion of Tp23191 with the fluorescent protein mNG under control of a native promoter was assembled and integrated into pTpPuc3. The marker tag mNG was placed between RXL and the cysteine domains, i.e., in the predicted luminal region of gene *Tp23191* (Figure 4.5.1). *Tp23191* contains three exons, which are protein coding regions. The location of these exons was taken into consideration during construction. The modified plasmid was transformed into *T. pseudonana* by bacterial conjugation. An illustration of pTpPuc3 with its most essential coding regions and the fusion protein mNG-Tp23191 is given in Figure 4.5.2.

Figure 4.5.1: Graphical illustration of the fusion protein mNG-Tp23191. The marker tag, *mNeonGreen* (mNG) was inserted between the protease cleavage site (RXL) and the conserved cysteine domains in the nucleotide sequence of *Tp23191*.

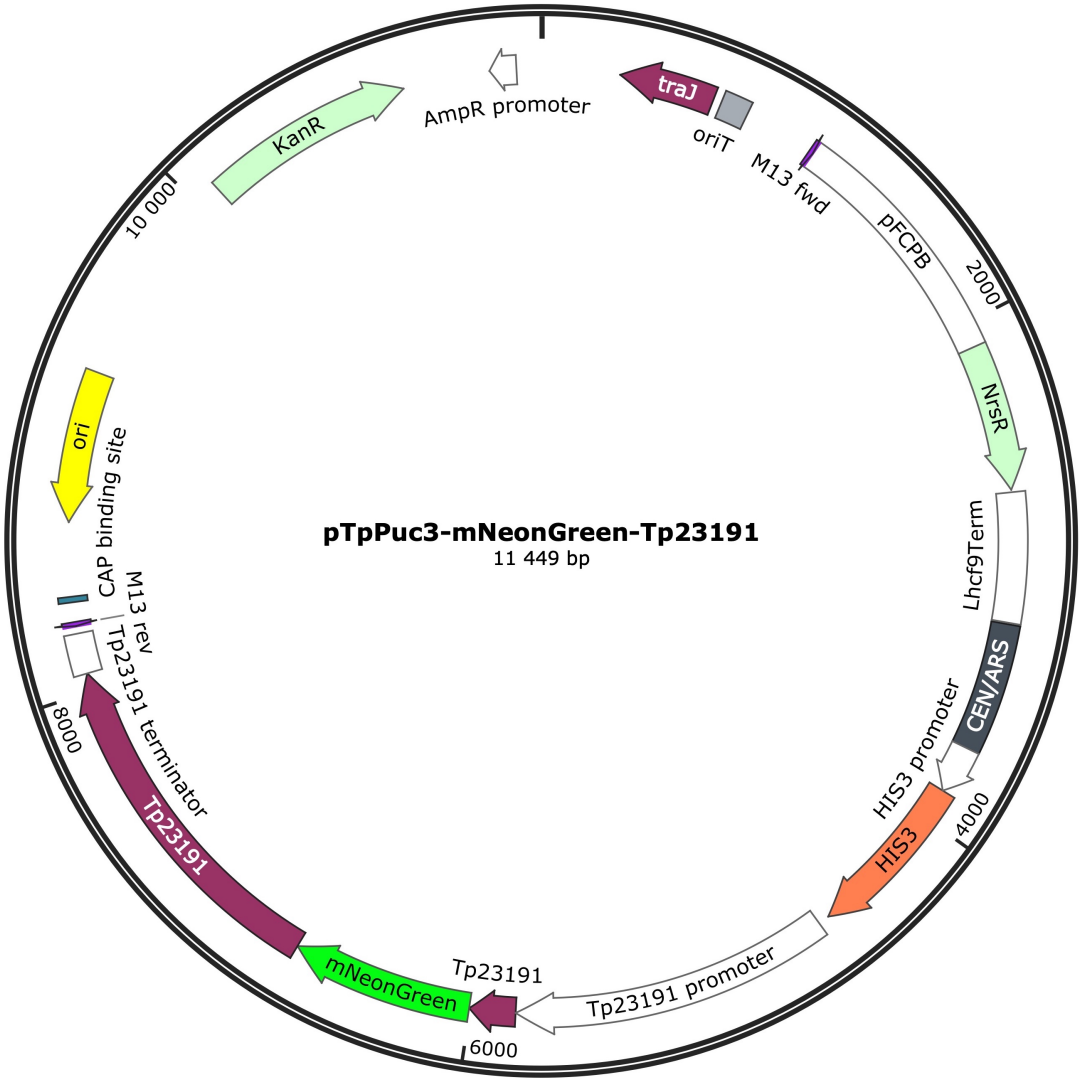

Figure 4.5.2: Plasmid pTpPuc3 with fusion protein mNG-Tp23191. The characteristic CEN6-ARSH4-HIS3 (CAH) region is necessary for plasmid maintainence in diatoms. *NrsR* gene confers to nourseothricin resistance in diatoms and *KanR* confers to kanamycin in bacteria.

Biovisualization of transgenic lines of *T. pseudonana* showed the presence of fusion protein mNG-Tp23191 in valves and girdle bands. Sharp dots of mNG-Tp23191 were observed on the outline of the cell and in the middle of the protoplast, suggestively consistent with the location of SDVs. Only a small fraction of cells expressed the fusion protein simultaneously, suggesting that functions of Tp23191 are related to specific stages of the cell cycle. Synchronized cell cycle arrest was obtained in cultures with *T. pseudonana* transformants by Si-starvation. A time-lapse detection was conducted after Si-replenishment, and the highest fluorescence signal within the range of mNG was detected in the first hour. Based on published research on synchronization studies and examination of results from flow cytometry, it was believed that most cells had arrested in the G_2+M phase. Thus, it is hypothesized that silicanin Tp23191 is utilized in the G_2+M phase of the cell cycle of *T. pseudonana*, but as no cell cycle determinations were conducted, no conclusion could be drawn. Hence, further investigation is necessary to determine if the silicanin family is participatory in the diatom frustule assembly.

4.6 The Cytoskeleton and its Role in Diatom Biosilicification

The cytoskeleton is a complex, dynamic network localized in the cytoplasm, with functions related to intracellular transport, cell shape, movements, and mechanical strength. The network contains different fibers, filaments, and associated molecules constantly in flux. Microfilaments, microtubules, and intermediate filaments are the three major components that build up the eukaryotic cytoskeleton. Each of them is constituted with a specific protein subunit as a result of polymerization [108]. Direct observations [28, 58], and cytoskeleton inhibitor treatments of several centrics [20, 121, 122], raphid pennates [123, 124], and araphid pennates [125], have given an insight into how elements of the cytoskeleton are involved in the cell wall biomineralization in diatoms. It has been observed that microfilaments are major contributors to the meso- and microscale, while microtubules affect the microscale positioning of biosilica (See Section 2.2 for more information regarding the different scales) [20, 22]. It is currently known that the assembly of microfilaments and microtubules play a crucial role in forming and shaping the SDV [28, 31, 126]. Moreover, it is thought that these elements impact the patterning of silica inside the SDV lumen, but this hypothesis requires the involvement of putatively unidentified proteins that connect elements in the cytoplasm with elements inside the SDV lumen [20, 21, 22].

Microfilaments, also called actin filaments, are built up to linear polymers by the globular multifunctional protein actin. The structure is illustrated in Figure 4.6.1, and the polymers are polar and tightly bound by ATP into a crosslinked network arranged into a loose spiral structure [127]. Actin is highly conserved among eukaryotes [128], and contributes to the outer cell shape and cell movement, as it produces protrusive (pushing) and contractile (pulling) forces [127, 129]. The protrusive movement is a result of coordinated polymerization of several actin filaments, while the contractile movement is due to sliding actin filaments along bipolar filaments [127]. Both forces are essential for cell movement, but also contribute to other areas such as cell shaping, cell polarity, cytokinesis, and mechanical properties of the cell surface [129].

The diatom cytoskeleton of microfilaments is highly organized in a complex network spanning the cytoplasm [129]. A genomic analysis of actin and actin-related proteins (ARPs) revealed that most diatoms possess one actin and a small number of ARPs within their genome [129]. Actin defines both overall and detailed patterned silica, in addition to the edges of SDV. The correspondence between the pattern of actin assembly and the creation of valves and girdle bands, confirms that the regulation of biosilica assembly is profoundly affected by microfilaments [20, 22].

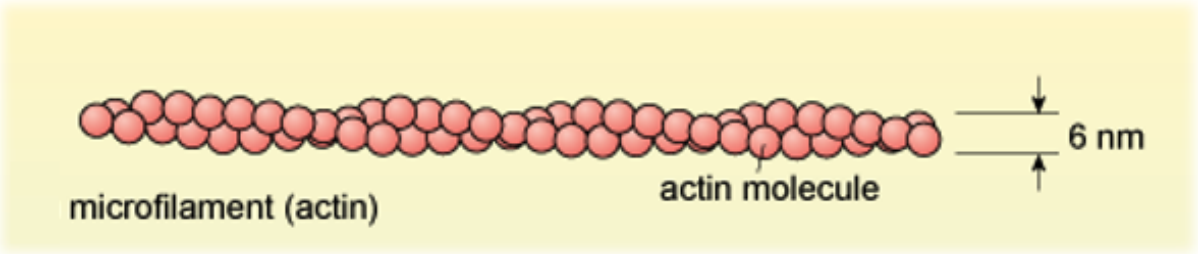

Figure 4.6.1: Microfilaments are composed of two chains of globular actin proteins tightly bound to ATP in a loose spiral structure and is an element of the cytoskeleton [130].

The structure of microtubules is shown in Figure 4.6.2. Microtubules are hollow and polar filaments made of tubulin subunits, which contain the two globular proteins, α- and β-tubulin [108]. The filaments are highly dynamic, and the microtubules can grow and shrink, resulting in pushing and pulling forces, respectively. During growth, a GTP-bound tubulin subunit attaches to the positive end of the microtubule. As hydrolysis occurs, GTP is reduced to GDP. Moreover, the GDP-bound tubulin dimer is covered in a stabilizing GTP-cap, which prevents depolymerization and makes the attachment of end-binding proteins possible [131]. Catastrophe is the common denotation of the process where microtubules change from its growing states and start shrinking. During depolymerization and shrinking, the microtubules are dynamically instable. Tubulin subunits dissociated from the plus end of the microtubule is a result of GTP hydrolysis [131].

Microtubules are responsible for the intracellular organization, organelle trafficking, and distribution of chromosomes during mitosis. They are organized in a complex network centered on the nucleus, and during mitosis, microtubules form a spindle, which is attached to the MC. A study on valve morphologyenesis in the centric diatom *Proboscia alata*, led to the hypothesis that the valve assembly is controlled by microtubules [121]. It has been observed that both the size and the position of SDVs in diatoms are influenced by microtubules [22]. Microtubules have also been associated with the expansion of the raphe in arapid pennates [22], and observations of the microtubule network in pennates have shown that the SDV is formed, followed by a connection between the SDV and the MC which is located close to the CN [25].

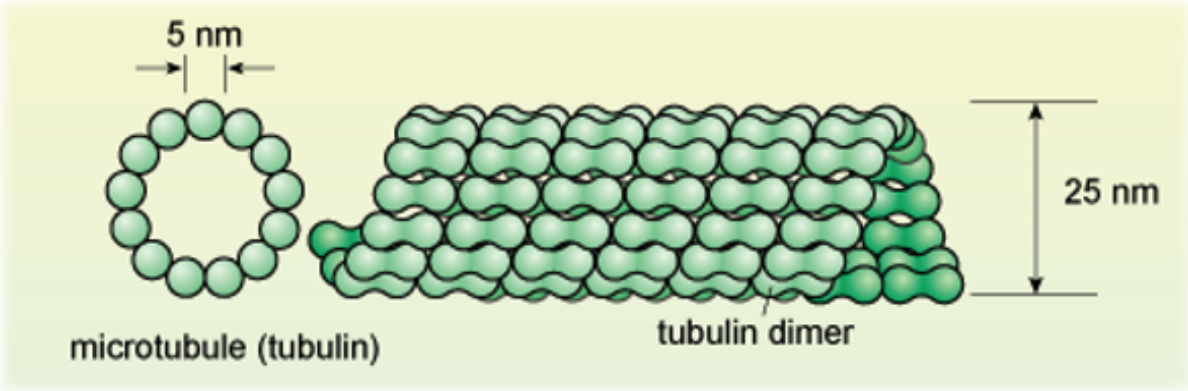

Figure 4.6.2: Microtubules, an element of the cytoskeleton, are hollow and built up by rings of 13 tubulin monomers arranged in a spral structure. [130].

Diatoms can be treated with inhibitors that affect different parts of the cytoskeleton, followed by an examination of the change in frustule morphology to determine the specific impact of the cytoskeleton on the biosilica structure of the specific species. Cytochalasin D has previously been used for investigation of the microfilament contribution in biosilica formation. This drug inhibits actin polymerization as it reacts with growing ends and hinders the addition of monomers to these sites [132]. Cytochalasin D causes cell arrest at the G_1-S boundary [133]. The affection of microtubules on biosilica formation has been studied with the use of colchicine and oryzalin. Colchicine binds to tubulin and thereby inhibits microtubule polymerization [134], while oryzalin depolymerizes microtubules [135]. Hence, both drugs interrupt cell division, which causes a block at the G_2-M boundary of the cell cycle [134, 135].

There are currently no published studies where *T. pseudonana* has been treated with drugs that inhibit cytoskeletal elements. Because the frustule morphology and biosilica assembly have been studied [32, 35, 56, 61], it would be beneficial to examine how different cytoskeleton inhibitors will affect the frustule morphology. Based on the hypothesis that cytoskeleton elements interact with proteins related to the silicalemma, it may be interesting to see if inhibitor treatments will affect the location of silicanins.

4.7 Aim of the Laboratory Research

The laboratory research aimed to investigate further the putative association between silicanin Tp23191 and frustule assembly and how elements of the cytoskeleton have an impact of frustule morphology. The change in fluorescence signal in transgenic lines of *T. pseudonana* with the integrated mNG-Tp23191 fusion protein, would give an indication of the expression pattern of gene *Tp23191* within the *T. pseudonana* genome. The role of elements of the cytoskeleton in frustule assembly was investigated by treating *T. pseudonana* cultures with drugs that inhibit different parts of the cytoskeleton and further examination of the changes in frustule morphology. Transgenic lines were also treated with the same inhibitors to see if the inhibition affected the fluorescence signal from mNG-Tp23191.

Four subgoals were defined:

- Successfully synchronize cells of *T. pseudonana* into the same growth phase, such that a time-lapse detection is possible.
- Investigate the change in fluorescence signal from mNG-Tp23191, localization of mNG-Tp23191, and the amount of fusion protein at different cell cycle stages.
- Find a suitable concentration for cytoskeleton inhibitors, where *T. pseudonana* cell growth is reduced but not stopped.
- Examine *T. pseudonana* frustule morphology after individual treatments with drugs that inhibit microfilaments and microtubules.

.

Chapter 5

Materials and Methods

5.1 Microbial Strains and General Cultivation Conditions

T. pseudonana strain CCMP1335 was obtained from The Culture Collection of Algae and Protozoa (CCAP) and grown in axenic cultures under constant light at 18°C. Cultivation medium f/2 was made as described in Appendix A.1, and the *T. pseudonana* cultures were stored in an oxygen-rich environment using cell culture flasks with filter caps delivered by VWR. To prevent plasmid loss, *T. pseudonana* transformants (denoted mNG-Tp23191) with plasmid pTpPuc3-mNG-Tp23191 were kept in f/2 medium with ntc (100 μg mL^{-1}). *T. pseudonana* is easier maintained when grown in a liquified medium compared to solid plates. However, when new transgenic lines were made, *T. pseudonana* cells were grown on L1 agar plates for a shorter period after bacterial conjugation. Before bacterial conjugation, cultures of *T. pseudonana* were grown in L1 medium, which is more nutrient-rich compared to f/2 medium. Recipes for L1 agar plates and L1 medium are given in Appendix A.2 and Appendix A.3, respectively.

DH10B strain of *Escherichia coli* was used as a molecular host during the transformation of pTpPuc3-mNG-Tp23191 to *T. pseudonana*. All growth of *E. coli* was done on Luria-Bertani (LB) agar plates or in liquified LB medium, see Appendix A.4 for detailed recipes. When not in use, cultures of *E. coli* were stored at -80°C.

5.2 Investigation of mNG-Tp23191 in *T. pseudonana* Transformants

The detected fluorescence signal within the range of mNG in transgenic lines can indicate when and where silicanin Tp23191 is present in *T. pseudonana*. The *T. pseudonana* transgenic lines created during the specialization project were used in the experiments explained in the following sections.

5.2.1 Synchronized Growth

To investigate mNG-Tp23191 at different cell cycle stages, cells of *T. pseudonana* were synchronized into the same growth phase by Si-starvation. The procedure was based on the protocol

by Hildebrand and Frigleri [57], with 24 h of incubation in Si-free medium and with a culture concentration of $1.0 \cdot 10^6$ cells/mL before Si-replenishment [57]. Three synchronization studies were conducted with different modifications, see Table 5.2.1. A wild type *T. pseudonana* (TpWt) culture was used as a negative control. *T. pseudonana* transformants were kept in f/2 medium without antibiotics three days prior to the experiments and during the synchronization studies. This was done to secure optimal growth and to reduce differences in growth conditions between the transformants and TpWt. Cultures were transferred to Si-free f/2 medium and kept under optimal growth conditions during incubation, both stirred and aerated. The medium recipe is given in Appendix A.1, and MAXQ2000 by Thermo Fisher was used for continuously stirring (120 rpm). For Si-replenishment, $Na_2SiO_3 \cdot 9H_2O$ (300 μM) was added to the different cultures.

Table 5.2.1: Synchronized cell arrest by Si-starvation was conducted with a different cell density of *T. pseudonana* cultures and different times in Si-free medium.

Number	Concentration at Si-starvation [cells/mL]	Time of Si-starvation [h]
1	$0.35 \cdot 10^6$	24
2	$0.5 \cdot 10^6$	24
3	$0.5 \cdot 10^6$	48

Flow cytometer BD Accuri C6 by BD Biosciences was used to measure the culture concentration. For the two first attempts of synchronization, the desired concentration was obtained by dilution. For the third attempt, culture concentrations were adjusted by cell harvesting (4200 g, 15 min) and further resuspension in Si-free f/2 medium. A constant cell density indicates stagnation in growth. Based on this, the change in culture concentration was used to determine the time of incubation in the Si-free medium during the third attempt of synchronization. Thus, the culture concentration was measured at three time-points (6 h, 24 h, and 30 h) when cells were kept in Si-free f/2 medium.

5.2.2 Detection of Fluorescence Pattern from mNG-Tp23191

For each timelapse detection, the first sample was collected before Si-replenishment, and further measurements were conducted with intervals of 30 min or 1 h. Flow cytometer BD Accuri C6 by BD Biosciences was used to measure the fluorescence pattern and changes in the population. The samples (0.5-1 mL) were run with a limit of either 5000 or 10 000 events, with medium flow. One cycle agitation was performed between each sample. The samples were excited by a 20 mW 488 nm Solid State Blue laser, and the fluorescence signal was measured with two optical filters: FL1 (533/30 nm) for the detection of fusion protein mNG-Tp23191, and FL3 ($>$ 670 nm) for detection of live cells, as the chlorophyll within the chloroplast has an emission peak at 677-678 nm. The BD Accuri C6 software was used to extract the data. Particles with fluorescence signal below 10^4 were presumed to be dead diatoms and were therefore excluded in the analysis.

5.2.3 Cell Cycle Stage Determinations

Samples (1.5 mL) for cell cycle stage determinations were hourly collected during the last synchronization study. A procedure developed by Hildebrand et al. was used for sample preparations [57]. Samples were spun down (5000 g, 10 min), before pellets were resuspended in methanol (1 mL), and incubated at 4°C overnight. The next day, cells were pelleted (5000 g, 10 min) and extracted in filtered phosphate-buffered saline, PBS, (1 mL, 20 mM phosphate buffer, pH 7.4, 150 mM NaCl). DNase free RNase was added (100 μg mL^{-1}), and cells were incubated (20°C, 60 min) with coherent shaking (250 rpm), using incubator Multitron by INFORS. Cells were pelleted (5000 g, 10 min) and washed twice in PBS (1 mL), followed by resuspension in PBS (25 μL). The nucleic acid dye SybrGreen was added (0.5 mL, 100x concentrate in dimethyl sulfoxide, DMSO), and incubated in darkness for 10 min before the samples (10 000 events, medium flow) were run on the flow cytometer NovoCyte by ACEA Biosciences. SybrGreen is characterized by sharp peaks for excitation at 280 nm and 502 nm and emission maximum at 530 nm when bound to a nucleic acid. Hence, the fluorescence signal from SybrGreen was monitored in channel BL1 (530/30 nm). Autofluorescence from chlorophyll was detected with channel BL4 (675/30 nm). The relative percentage of cells in phase G_1, S, and G_2+M were calculated with the NovoCyte software, NovoExpress.

5.2.4 Immunodetection of mNG-Tp23191

Samples (1.5 mL) were harvested three times during the last attempt of synchronization; prior to Si-addition, 4 h after Si-addition, and 9 h after Si-addition. Proteins were isolated following a protocol described by Nymark et al. [136]. Cells were harvested by filtration through membrane filters (Durapore Membrane Filters, pore size: 0.65 μm; Merck Millipore). Cells on filters were extracted in f/2 medium (1 mL) in Eppendorf tubes, vortexed (5 sec), and filters were removed. Furthermore, samples were centrifuged (16 000 g, 1 min), and supernatants were decanted before cells were stored at -80°C for 5 min.

Cells were mechanically broken down into smaller fractions such that protein extraction would be possible. A pre-cooled bead of stainless-steel was added to the pellets, and the samples were placed in a pre-cooled adapter set and run in TissueLyser 2 from Qiagen. Samples were transferred to a pre-warmed adapter set before the second run. Program settings are given in Table 5.2.2. Lysis buffer (700 mL, 50 mM Tris, pH 6.8, 2% [w/v] sodium dodecyl sulfate, SDS) was added, followed by centrifugation (130 g, 30 min, 4°C) and collection of the supernatant. Protein concentrations were determined with Qubit 3 Fluorometer from Invitrogen.

Table 5.2.2: Program settings used on TissueLyser 2 to break down cells into smaller fractions. The samples were run twice with different temperatures on the adapter set and with different duration times.

Run	Adapter set [°C]	Frequency [Hz]	Time [min]
1	-80	25	2
2	20	25	8

SDS-polyacrylamide gel electrophoresis (SDS-page) was done to separate proteins according to size. Two parallels were performed, see Appendix B.1 for the detailed procedure. TpWt was used as a negative control, while a pre-made protein sample derived from *E. coli* with integrated plasmid pNCS-mNG, was used as a positive control. mNG is placed after a constitutive *E. coli*

promoter in plasmid pNCS, and should, therefore, be present for this protein sample. After SDS-page, the gel was removed from the chamber and equilibrated in Twobin buffer (10 min). Instructions concerning the Twobin buffer are given in Appendix B.2.

One parallel was stained with SimplyBlue SafeStain (20 mL) by Invitrogen and incubated at room temperature with constant shaking for 1 h. This procedure was done to visualize the different protein bands. The other gel was used for western blot for the detection of mNG. A polyvinylidene difluoride (PVDF) membrane was prepared, as described in Appendix B.3. PVDF membrane, gel, and filter papers were stacked in a sandwich setup, as illustrated in Figure 5.2.1. An electric field (25 V, 1.0 A) was applied to the gel for 30 min to facilitate the migration of proteins from the gel and onto the membrane. The blotting was performed using the Trans-Blot Turbo Transfer System by Bio-Rad. After blotting, the membrane was pre-activated with methanol (100%, 30 sec) and rinsed with MQ (1-2 min).

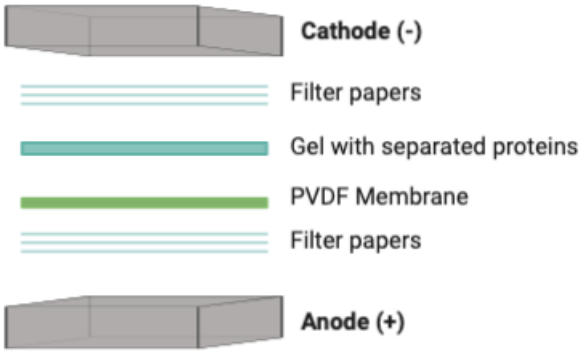

Figure 5.2.1: Assembly of a sandwich setup. The separated proteins are transferred from the gel and to the membrane.

Immunodetection was performed using iBind Flex Western Device by Invitrogen. iBind solution, made as described in Appendix B.4, was pipetted onto the blotted membrane with the protein-side pointing upwards, onto the whole flow region, and at the center of the membrane region of the iBind Card. Furthermore, the membrane was placed in the iBind system with the protein-side pointing downwards and the region with the lowest protein molecular weights closest to the stack. A blotting roller was used to remove air bubbles. Wells were loaded as described in Table 5.2.3.

Table 5.2.3: The solutions and the specific volume that was added to the different wells in an iBind Flex Western Device before the imunodetection was conducted.

Well	Content	Volume [mL]
1	primary antibody	2
2	1x iBindSolution	2
3	secondary antibody	2
4	1x iBindSolution	6

mNG tag antibody (1:1000) from Cell Signaling Technology was used as the primary antibody, while Goat anti-Rabbit IgG (H+L) horseradish peroxidase-conjugated (1:2000) by Invitrogen was used as the secondary antibody. Both antibodies were diluted to desired concentrations

using a 1x iBind solution, and the setup time was set to 2.5 h. After incubation, the membrane was rinsed with Milli-Q (MQ) (20 mL, 2 min x 2). Furthermore, the membrane was prepared with SuperSignal West Pico Plus Chemiluminescent working solution (50 % Peroxide solution, 50% Luminol/Enhancer solution), and incubated in darkness for 5 min. The membrane was visualized under UV light with ChemiDoc XRS+ Imaging System from Bio-Rad.

5.3 Transfer of pTpPuc3-mNG-Tp23191 into *T. pseudonana* by Bacterial Conjugation

Plasmid pTpPuc3-mNG-Tp23191 was delivered into *T. pseudonana* by bacterial conjugation, as illustrated in Figure 5.3.1, following a method developed by Karas and coworkers [112]. *E. coli* DH10B-strain are competent as they can take up foreign DNA from the surrounding environment [108]. Additionally, this strain contains episome pTA-mob, which can immobilize an integrated plasmid and further transfer it to another organism by conjugation. pTa-Mob contains Gm^r which confers resistance to gentamicin (gen) [137], while pTpPuc3 contains *NrsR* which confers resistance to kan, as previously mentioned [112]. Hence, kan (50 μg mL^{-1}) and gen (10 μg mL^{-1}) were used to ensure selective growth of *E. coli* with both episome and plasmid.

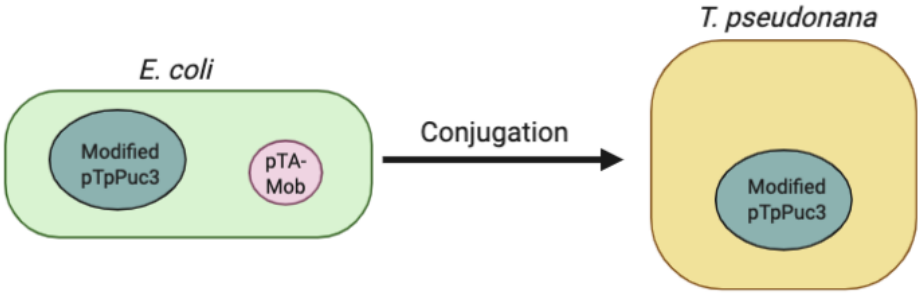

Figure 5.3.1: Bacterial conjugation. Episome pTA-Mob in *E. coli* immobilizes the integrated plasmid before conjugation. Only modified pTpPuc3 is transferred to the diatom species *T. pseudonana*.

The modified plasmid was transferred into competent *E. coli* DH10B cells by heat-shock transformation, as described in Appendix B.5. Colonies were picked from agar plates after overnight incubation, and grown in flasks with LB medium until the next day at 37°C. A culture of *E. coli* DH10B cells (150 mL) were grown at 37°C with coherent shaking (120 rpm), using incubator Multitron by INFORS until reaching an OD_{600} between 0.3 and 0.4. Cells were spun down (4000 g, 10 min) and resuspended in Super Optimal Broth (SOC) medium (800 μL). TpWt culture was grown in L1 medium, and the cell culture was adjusted into a total concentration of $2{\cdot}10^8$ cells mL^{-1}. Pellets were made by centrifugation (5500 g, 10 min x 3) and resuspended in L1 medium to a total of 1 mL.

Cell cultures of *T. pseudonana* (200 μL) and *E. coli* (200 μL) were added to an Eppendorf tube and mixed by gently pipetting up and down before plated on pre-heated agar plates (94% L1 medium, 5% LB, 1% agar). Plates were incubated in darkness at 30°C for 90 min, followed by 4 h in light at 18°C. The temperature for incubation in darkness is a compromise between the optimal growth conditions for *E. coli* and *T. pseudonana*, as the former has an optimal growth

condition at 37°C and the latter has optimal growth at 18°C [112]. f/2 medium (1 mL) was added to the agar plates, and cells were scraped. A volume of 200 μL was transferred to three L1 agar plates with ntc (100 μg mL^{-1}). Plates were incubated in light at 18°C.

After 16 days, twelve colonies from plates were picked and transferred to wells with f/2 medium (2 mL, ntc 100 μg mL^{-1}). After 34 days, the clones were analyzed with flow cytometry (FCM), and a TpWt culture was used as a negative control. This was done with flow cytometer DB Accuri C6 by BD Biosciences, with the same sample preparations and settings as described in Section 5.2.2. The two *T. pseudonana* transformants with the highest detected fluorescence signal within the emission wavelength 533 $\pm$ 15 nm were grown in larger culture flasks for further analysis. The plates were stored in darkness at 4°C, and after one month, twelve new colonies were picked and examined with fluorescence microscopy to see if the fusion protein was present.

5.4 Genomic Analysis of *T. pseudonana* Transformants

Cells were harvested by filtration through membrane filters (Durapore Membrane Filters, pore size: 0.64 μm: Merh Millipore) and transferred to Eppendorf tubes. A protocol from Qiagen was used for DNA isolation, see Appendix B.6 for the detailed procedure. DNA concentrations were measured with Qubit 3 Fluorometer by Invitrogen.

Polymerase chain reaction (PCR) was conducted for the analysis of DNA from two cultures of transgenic lines. DNA from TpWt was used as a control, and five different DNA fragments were amplified. Phusion High-Fidelity DNA Polymerase kit by Thermo Fisher Scientific was used for sample preparations according to the manufacturer's protocol, see Appendix B.7. The suggested Thermal Cycler setup given by Thermo Fischer Scientific was followed for all PCR reactions. The settings are given in Table 5.4.1. Annealing temperature and elongation time were adjusted to the primers melting temperature and the length of the DNA fragment. See Appendix B.8 for a detailed description of all DNA constructs, the belonging primers, annealing temperature, and elongation time. A map of the plasmid with the primers used for amplification is shown in Appendix C.1.

Table 5.4.1: Settings used on Thermal Cycler for all PCR reactions. Annealing temperature and elongation time were adjusted to the melting temperature of the primers and the length of the amplified DNA fragment, respectively. These are given in Appendix B.8.

Program	**Temperature [°C]**	**Time**	**Cycles**
Initiation	98	1	1
Denaturation	98	0.5	
Annealing	*	0.5	30
Elongation	72	*	
Final extension	72	5	

Gel electrophoresis was conducted for all PCR products. See Appendix B.9 for agarose gel recipe, sample preparations, and settings of the voltage source. DNA bands were visualized with Syngene Gbox EF Gel Imaging System. For further analysis, some DNA bands were cut out of the agarose gel and purified with a QIAquick gel extraction kit from Qiagen. Amplicons were analyzed on the nucleotide level with the use of Sanger sequencing. This was done by Eurofins

Genomics. DNA samples were prepared as described in Appendix B.10, before they were sent to Eurofins Genomics. The results were aligned with the expected nucleotide sequence from each reaction using SnapGene by GSL Biotech LLC. The nucleotide sequence for *mNeonGreen* and *Tp23191* were retrieved from National Center for Biotechnology Information (NCBI).

5.5 The Impact of Cytoskeleton Inhibition on *T. pseudonana*

How the cytoskeleton affects the growth and frustule morphology on *T. pseudonana* cells, were investigated by treating different cultures with several cytoskeletal inhibitors. Cytochalasin D hinders actin polymerization, while colchicine and oryzalin inhibit microtubules [132, 134, 135]. To determine the concentration at which cell growth was reduced but not stopped, inhibitors with different concentrations were added to cultures of mNG-Tp23191 and TpWt. *T. pseudonana* transformants grew on ntc throughout the whole experiment, and a TpWt culture without inhibitors was used as a control. The specific concentrations are described in Table 5.5.1. Cytochalasin D was prepared in DMSO, while oryzalin and colchicine were dissolved in water when preparing stock solutions. Cell concentrations were measured before addition, after 24 h and after 48 h with flow cytometer BD Accuri C6 by BD Biosciences. The impact of different grades of treatments was determined by comparing the change in cell density after inhibitor treatment with cultures without treatment.

Table 5.5.1: Final concentrations of the respective inhibitors added to different cultures of *T. pseudonana*.

Chemical	**Final concentration [μM]**			
Cytochalasin D	1.5	3.0	6.0	12.0
Colchicine	25	50	100	200
Oryzalin	0.1	0.2	0.4	0.8

Cultures of TpWt (50 mL, 744 cells/mL) were separately treated with different inhibitors. A TpWt culture (50 mL, 744 cells/mL) without inhibitors was used as a control, and all cultures were incubated in light at 18 °C. After four days of incubation, the frustules were cleaned using the soft cleaning protocol developed by Romann et al. [138]. This cleaning treatment was done to remove organic material before frustule morphology was examined with SEM. Some modifications were done, see Appendix B.11 for the stepwise procedure.

5.6 Microscope Studies of *T. pseudonana*

5.6.1 Scanning Electron Microscopy (SEM)

Frustules of *T. pseudonana* were imaged using a Thermo Fisher Scientific (FEI) Teneo, a field emission scanning electron microscope. Pre-cleaned frustule samples were prepared as described in Appendix B.12. Program settings are given in Table 5.6.1.

Table 5.6.1: Program settings used for imaging of frustules with SEM

Settings	Amount
Voltage source	HT 10 kV
Beam current	0.1 nA
Detector	ETD
Enlargement	20 000 x

5.6.2 Fluorescence Microscopy

The fluorescence microscope ZEISS Axio Imager 2 was used with the plan-achromat objective with 20X and 40X. HXP-120 was used as a UV light source. Two optical filters were used; one with emission bandwidth of range 505-555 nm was for the detection of fluorescence from mNG, and emission bandwidth greater than 650 nm for the detection of autofluorescence.

5.6.3 Confocal Laser Scanning Microscopy (CLSM)

Leica TCS SP5 confocal laser scanning microscope was used with an objective lens with a 63x enlargement. Ar-Laser, 488 nm was used with 30% intensity. Two optical filters were used; one with emission bandwidth from 500-570 nm detecting fluorescence from mNG and the other with emission bandwidth greater than 650 nm for the detection of autofluorescence.

5.6.4 Sample Preparation before Fluorescence Microscopy and CLSM

Cell cultures were immobilized to optimize images before fluorescence microscopy and CLSM were conducted. Alginate (0.33 mL, 2%) was added to cell culture (1 mL). A sample volume of 30 μL was applied to a coverglass (24 mm x 24 mm), and $CaCl_2$ (30 μL, 50 mM) was applied. A lens paper was used to remove excess fluid before the sample was covered with a microscope slide (grand edges). A SecureSeal imaging spacer (20 mm x 0.12 mm) was additionally used to seal the sample. This was done to prevent the cells from drying out during microscopy.

Chapter 6

Results

6.1 Expression Level of mNG-Tp23191 in Transgenic Lines of *T. pseudonana*

To investigate the expression of mNG-Tp23191 in the transgenic lines mNG-Tp23191-4 and 11 of *T. pseudonana* at different cell cycle stages, three synchronization studies were conducted. Stagnation in growth was induced by Si-starvation, followed by Si-replenishment and a time-lapse analysis with FCM. Different cell density before Si-starvation and incubation time was crucial to obtain a successful synchronization. Hence, the different modifications, together with the results, are summarised in Table 6.1.1.

Table 6.1.1: Three cell cycle stage synchronization studies were conducted with a few modifications. This table includes different attempts together with a short experimental explanation and conclusion.

Study	Concentration [cells/mL]	Starvation time [h]	Conclusion	Explanation
1	$0.35 \cdot 10^6$	24	Not successful	Error in measurements of fluorescence detection
2	$0.5 \cdot 10^6$	24	Not successful	Cultures are not synchronized in growth
3	$0.5 \cdot 10^6$	48	Successful	Synchronized cultures and valid fluorescence signal

As stated in Table 6.1.1, only the last cell cycle synchronization was successful. The two other synchronization studies were considered unsuccessful as the first study had an error in fluorescence detection, and the second study had unsynchronized before Si-replenishment. Graphical illustrations and further explanations of all attempts are given in the following sections.

6.1.1 The First Attempt of Synchronized Growth

Data from the first synchronization study is presented in Figure 6.1.1. The change in cell concentration and mean fluorescence signals in the range of mNG are given as a function of time after Si-replenishment. The culture concentration changed over time (Figure 6.1.1.A), but the experiment was terminated after 4 h due to the irregular pattern of fluorescence signal (Figure 6.1.1.B). Thus, the attempt was concluded as unsuccessful.

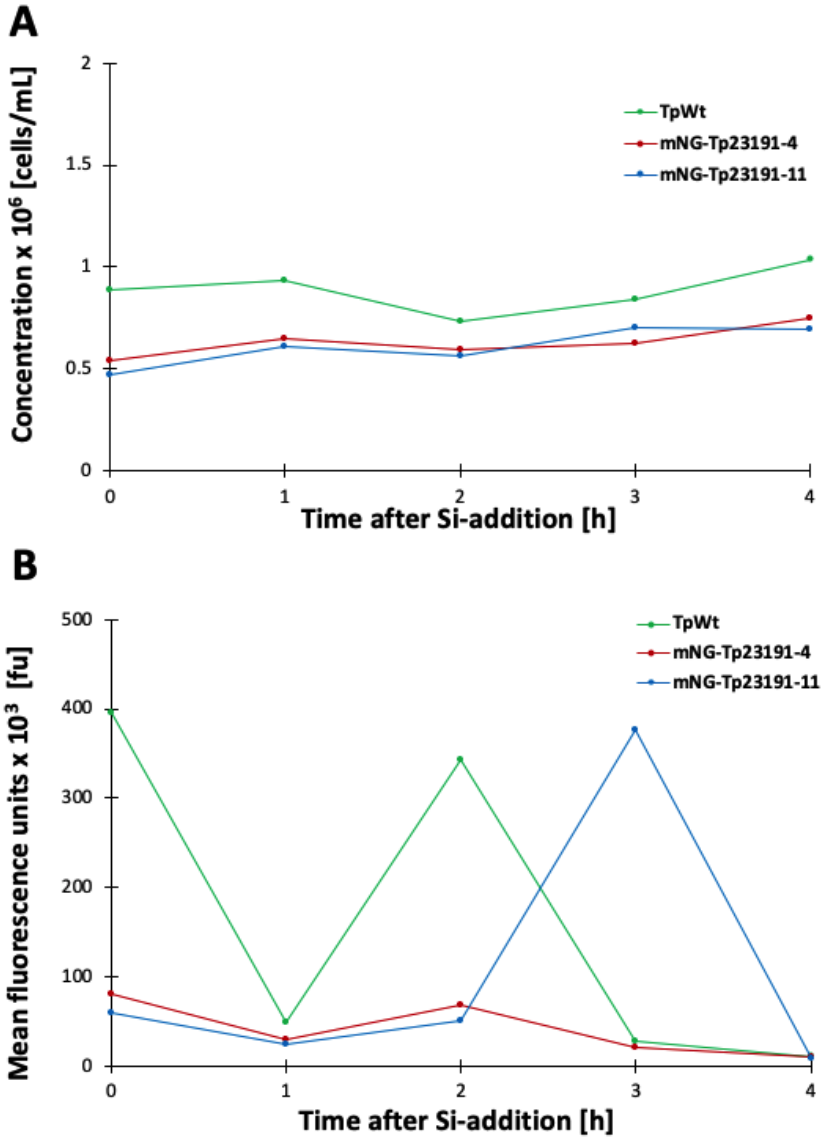

Figure 6.1.1: The first synchronization study. Measurements were conducted on pre-silicate starved *T. pseudonana* transformants with integrated fusion protein (mNG-Tp23191) and one wild type (TpWt). **A**) Cell concentration as a function of time. **B**) Mean fluorescence units detected within the range of mNG-Tp23191 as a function of time.

6.1.2 The Second Attempt of Synchronized Growth

Figure 6.1.2 represents data from the second synchronization study. The mean fluorescence signal in the range of mNG was remarkably larger for transgenic lines compared to TpWt. The level of signal decreased for transgenic lines throughout the experiment, while it was nearly constant for TpWt. (Figure 6.1.2.B). A sharp increase in cell concentration was observed for all cultures after 1 h. However, due to no significant changes in cell density for the next six hours (Figure 6.1.2.A), it was concluded that no cultures had achieved a complete arrest in growth prior to the Si-replenishment. Thus, the second attempt of synchronized cell cycle arrest was considered as unsuccessful.

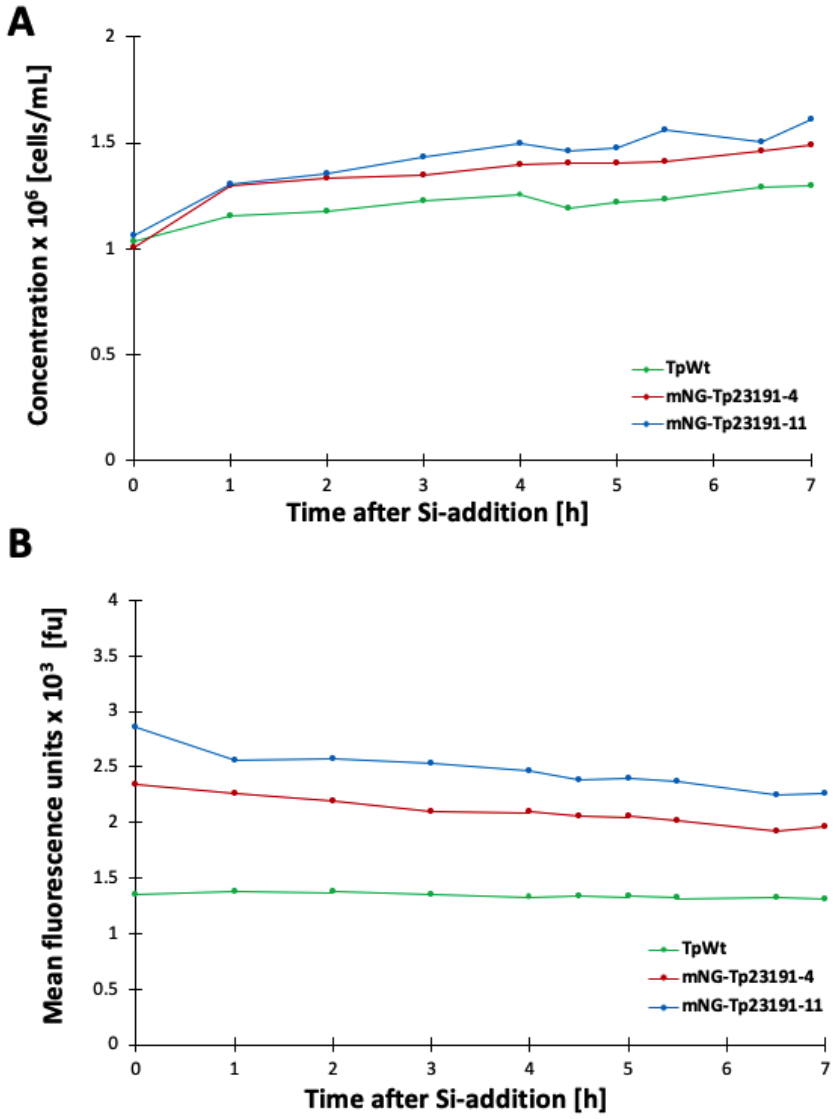

Figure 6.1.2: The second synchronization study. Measurements were conducted on pre-silicate starved *T. pseudonana* transformants with integrated fusion protein (mNG-Tp23191) and one wild type (TpWt). **A**) Cell concentration as a function of time. **B**) Mean fluorescence units detected within the range of mNG-Tp23191 as a function of time.

6.1.3 The Third Attempt of Synchronized Growth

For the third attempt of synchronization, the change in cell density was monitored during Si-starvation (Figure 6.1.3). Cultures had an exponential and identical growth rate until 24 h. Thereafter, mortality was observed among both transformants, in contrary to TpWt, which showed a gradually decreased growth rate.

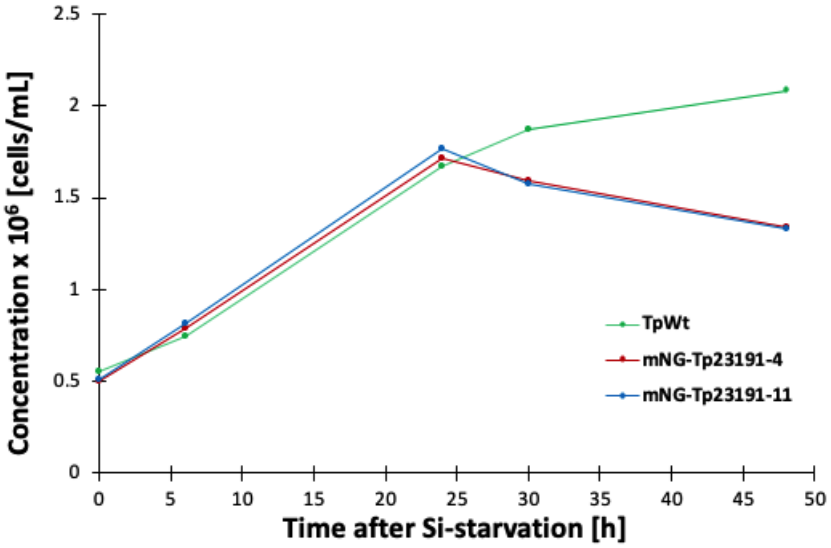

Figure 6.1.3: Cell concentration as a function of time after incubation in Si-free medium. mNG-Tp23191-4 and 11 contains integrated fusion protein while TpWt is a wild type of *T. pseudonana*.

The change in cell concentration and mean forward scatter (fsc) for the nine-hour experiment is given in Figure 6.1.4 A and B, respectively. As fsc is proportional to cell size, a comparison of these plots can indicate whether the attempt of synchronization was successful, and at what stages the majority of the cells had obtained cell cycle arrest. The fraction of live cells was approximately on the same level for TpWt, while the mean cell size slightly increased throughout the experiment. The trend observed for TpWt was different from the two transformants. mNG-Tp23191-4 and 11 had an identical growth rate with an increase in cell density of 21-22% and 34-36% the first hour and between 6-7 hours, respectively (Figure 6.1.4.A). The first hour, fsc decreased with 6-7% (Figure 6.1.4.B). The sharp temporary reduction at 3 h is inexplicable as the fraction of live cells was higher at this time point, compared to the previous and next measurements (See Appendix D.1 for more information). This error is probably due to underestimation, maybe as a result of sedimentation after insufficient stirring. Seven hours after Si-replenishment, 80-81% of cells from transgenic lines had divided. The detected changes in concentration and fsc for the two transformants, indicated that they were synchronized, while TpWt was not.

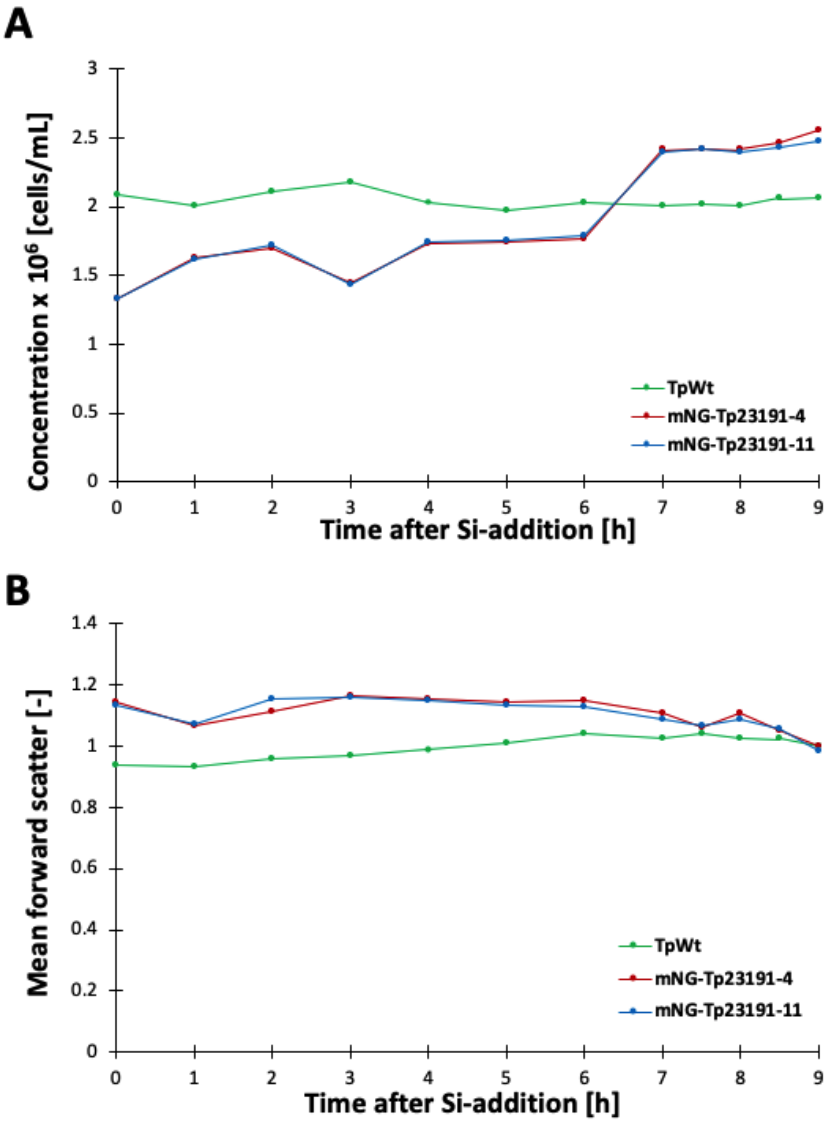

Figure 6.1.4: The third synchronization study. Measurements were conducted on pre-silicate starved transformants with fusion protein (mNG-Tp23191) and wild type (TpWt) of *T. pseudonana*. **A**) Cell concentration as a function of time. **B**) Mean forward scatter (fsc) as a function of time.

As seen from Figure 6.1.5, the change in mean fluorescence signal in the range of mNG is significantly lower for TpWt compared to transgenic lines. The detected fluorescence signal decreased for both transformants, while it was only slightly reduced for TpWt throughout the experiment. The expression pattern of mNG-Tp23191 was similar for the two transformants, and the results indicate that the highest expression of mNG-Tp23191 was at 0 h.

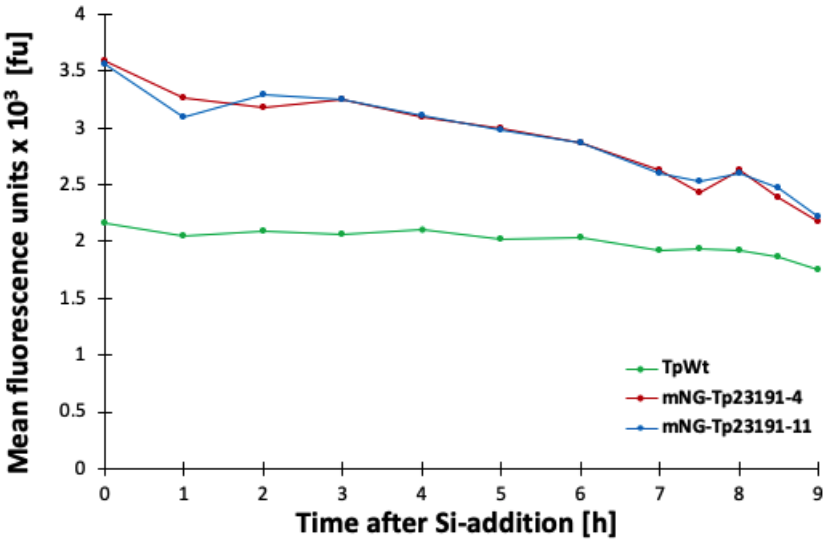

Figure 6.1.5: Mean fluorescence signal given as a function of time for three pre-synchronized *T. pseudonana* cultures. mNG-Tp23191-4 and 11 are transformants with the fusion protein, while TpWt is a wild type of *T. pseudonana*.

6.1.4 Cell Cycle Stage Determinations

Cell cycle stage determinations were conducted such that the change in fluorescence pattern and concentration of fusion protein mNG-Tp23191 could be coupled to different cell cycle stages. Thus, samples were collected during the third synchronization study. After pre-treatment and staining of nucleic acids with SybrGreen, samples were examined with FCM and NovoCyte software. With this method, cells in G_2 and M cannot be distinguished, and therefore, cells were partitioned in three groups; G_1, S, and G_2+M. The automatic grouping of plots was not successful, and the gating had to be manually adjusted for each measurement. This was done using a height versus area density plot on the fluorescent channel for SybrGreen (Figure 6.1.6.A). Thus, a varying percentage of the cell populations were gated to enable grouping of the different plots. The program assembled cell cycle plots from the cells within the gated area (Figure 6.1.6.B).

Due to the transformants having a similar pattern, only plots from mNG-Tp23191-4 and TpWt are given below. Supplementary plots of mNG-Tp23191-11 are given in Appendix D.2. The NovoCyte software calculated that all cultures had an approximately similar distribution of cells at 0 h. This distribution is shown for TpWt, see Figure 6.1.6.B. Plots from measurements before and after the significant increase of cell density of mNG-Tp23191-4, showed a clear significant decrease of cells in G_2+M from 6 h to 8 h (Figure 6.1.6.B).

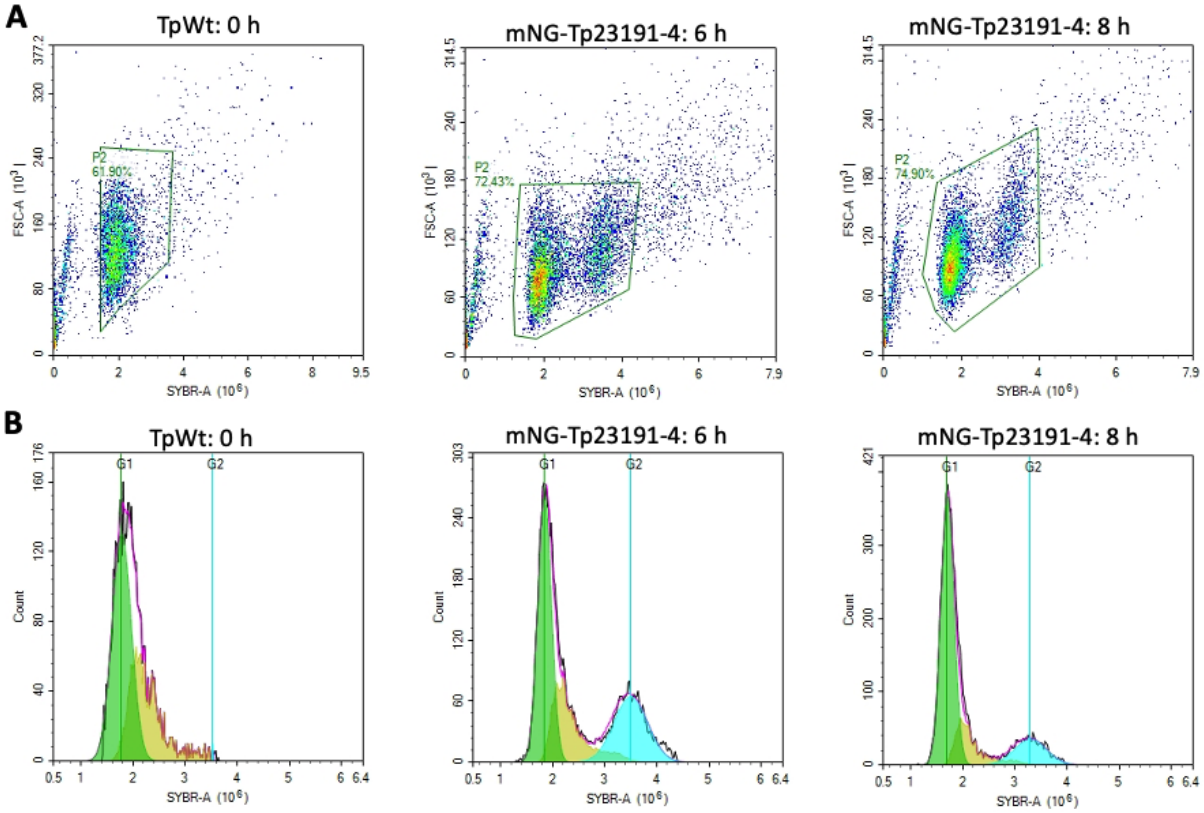

Figure 6.1.6: Cell cycle stage determinations with NovoCyte software. **A**) Manual gating in NovoCyte of the population for each measurement. **B**) Distribution of cells in different stages of the cell cycle; G_1 (green), S (yellow) and G_2+M (blue). TpWt is a wild type, while mNG-Tp23191-4 is a transformant of *T. pseudonana*.

The relative percentage of cells in the different phases for the three *T. pseudonana* cultures as a function of time, are shown in Figure 6.1.7. The largest percentage of cells were in the G_1 phase throughout the whole synchronization study, with the exception of transformant 4 at 3 h and transformant 11 at 4 h. At these time-points, most cells were calculated to be in the S-phase. According to the three plots, there is a negative correlation between the S phase and G_1. For the two transformants (Figure 6.1.7.A-B), G_2+M had a steady amount of cells throughout the experiment, varying between 0-23% for transformant 4 and 4-29% for transformant 11. Remarkably, under 0.5% of the cells were calculated to be in G_2+M the first two hours for TpWt (Figure 6.1.7.C).

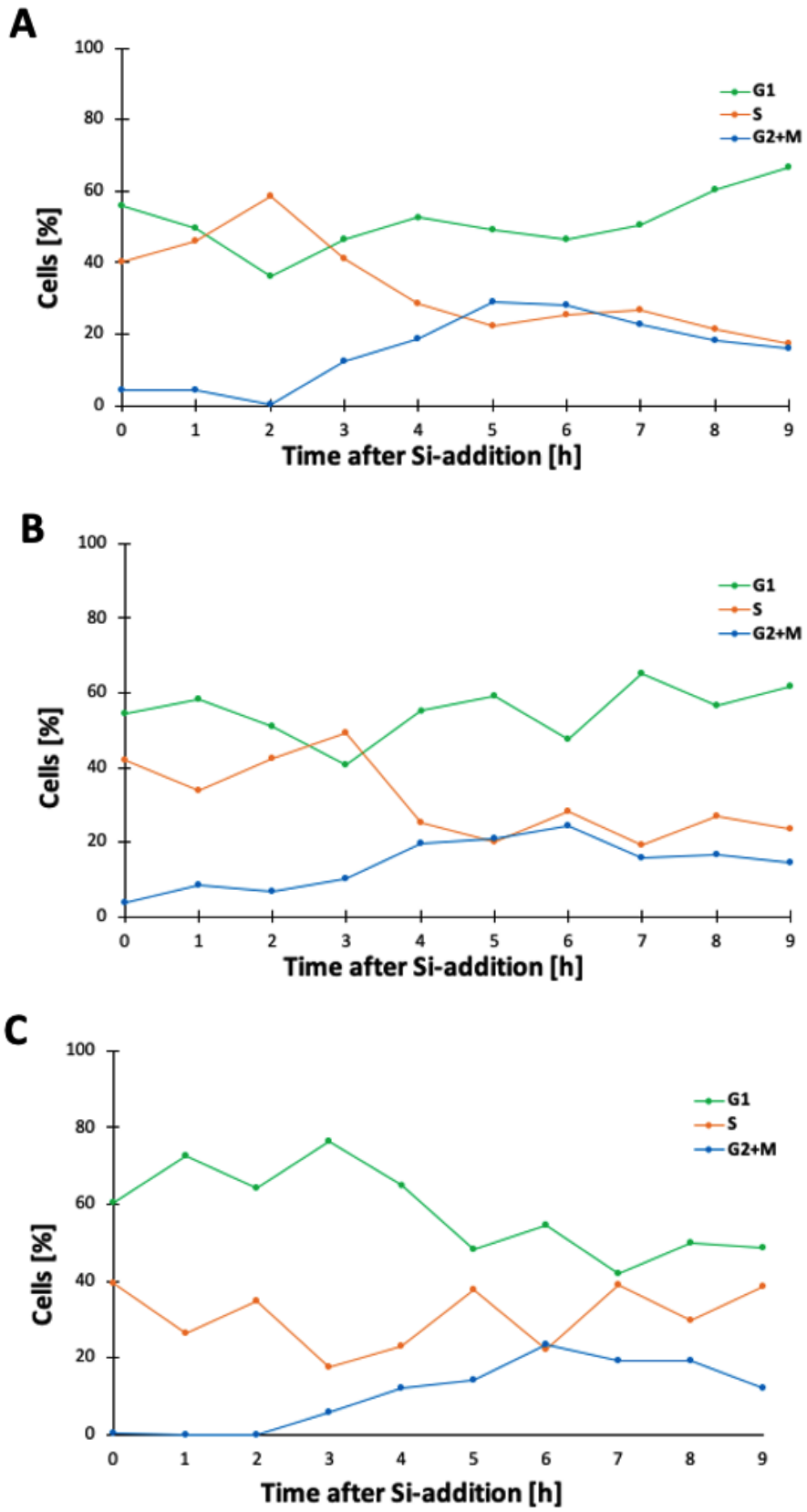

Figure 6.1.7: The relative percentage of cells in different cell cycle stages as a function of time after Si-addition. All *T. pseudonana* cultures were pre-synchronized with 48 h of Si-starvation. **A**) Transformant 4 with fusion protein mNG-Tp23191. **B**) Transformant 11 with fusion protein mNG-Tp23191. **C**) Wild type.

6.1.5 Immunodetection of mNG-Tp23191 in *T. pseudonana* Transformants

To verify the presence of fusion protein in *T. pseudonana* transformants, and to investigate how the concentration of fusion protein changes during a whole cell cycle, samples were harvested several times during the third synchronization study. This section outlines the results from the samples collected 4 h after Si-replenishment. The total protein concentration and the mean protein concentration per thousand cells are given in Appendix D.3. A western blot was conducted. Proteins were separated according to the size with SDS-page, and immunodetection was conducted to verify if the fusion protein was present among *T. pseudonana* transformants. The different sample content is given in Table 6.1.2, as a combination of protein extract, pellet, and the supernatant was used.

Table 6.1.2: Protein samples collected from cultures of wild type *T. pseudonana* (TpWt), transformants of *T. pseudonana* with fusion protein (mNG-Tp23191) and *E. coli* with pNCS-mNG.

Well	Type of organism	Sample content
1	*E. coli* with pNCS-mNG	Protein extract
2	*E. coli* with pNCS-mNG	Protein pellet
3	TpWt	Protein extract
4	mNG-Tp23191-4	Protein extract
5	mNG-Tp23191-11	Protein extract
6	mNG-Tp23191-4	Supernatant
7	mNG-Tp23191-4	Protein pellet

Results from SDS-page and immunodetection are visualized in Figure 6.1.8.A and B, respectively. Only the band sizes closest to the bands are given in kDa, see Appendix C.2 for all band sizes. As seen from Table 6.1.2, two different samples with positive control were run; *E. coli* from protein extract and protein pellet. Only the latter had visible bands after SDS-page. All samples of *T. pseudonana* had a lower content of proteins compared to the protein pellet from *E. coli* (Figure 6.1.8.A). Moreover, after immunodetection with western blot, only the protein pellet from *E. coli* had visible bands (Figure 6.1.8.B). The sizes of approximately 17 kDa and 13 kDa were not in coherence with the expected size of proteid mNG (26.7 kDa). However, it confirmed that the immunodetection was successful, and mNG was not detected in the protein samples isolated from *T. pseudonana* transformants.

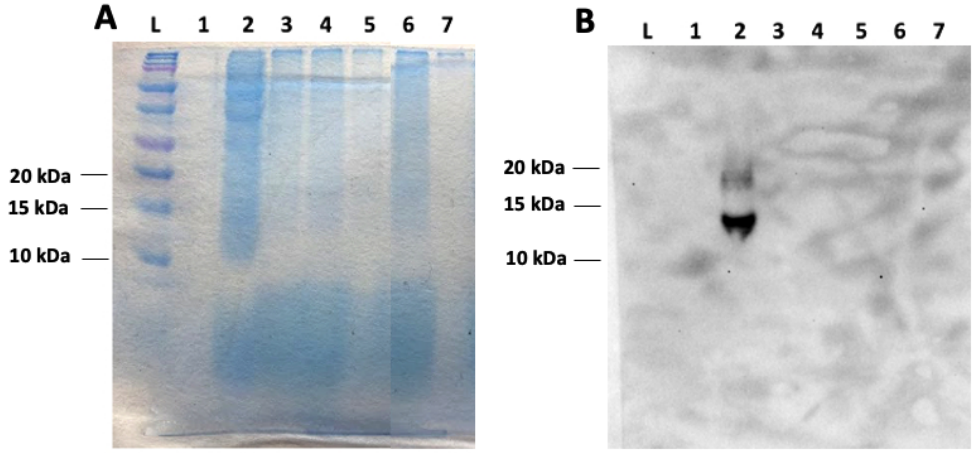

Figure 6.1.8: Western blot for the detection of mNG in cultures of *T. pseudonana* with fusion protein mNeonGreen-Tp23191, with a wild type of *T. pseudonana* as a negative control, and *E. coli* with integrated mNeonGreen as positive control. The content in each well is described in Table 6.1.2. **A**) Protein separation with SDS-page. **B**) Immunodetection of protein mNG.

6.2 The Creation of New *T. pseudonana* Transformants

Initially, the same *T. pseudonana* transformants created during the specialization project were supposed to be used throughout the whole laboratory research. After the third synchronization study, microscope studies revealed that the fusion protein was no longer visible in neither cells from mNG-Tp23191-4, nor mNG-Tp23191-11. Therefore, new transformants were created by the insertion of pTpPuc3-mNG-Tp23191 into *T. pseudonana* cells with bacterial conjugation. Twelve colonies were picked and analysed with FCM, using TpWt as a negative control. As seen from Figure 6.2.1, a higher fluorescence signal within the range of mNG was detected among 11 out of 12 clones. mNG-Tp23191-7 and 8, with the most significant fluorescence detection, were chosen for further analysis.

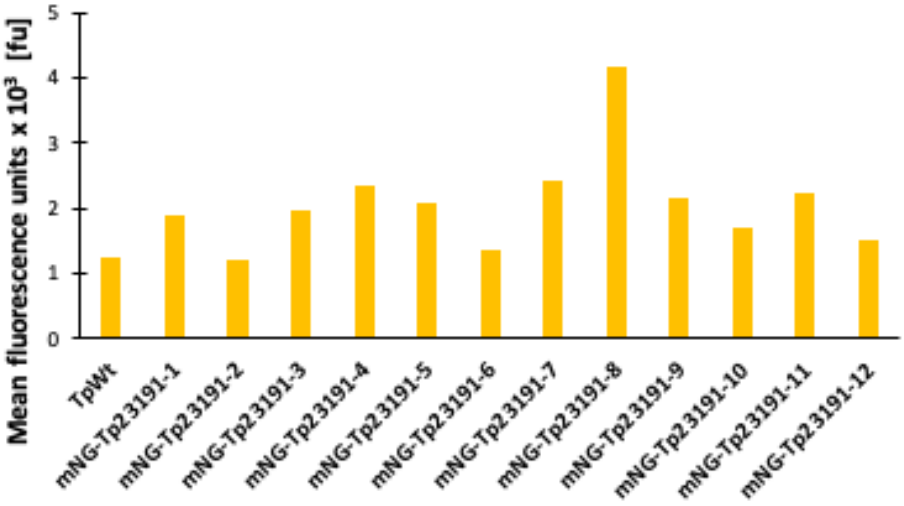

Figure 6.2.1: Mean fluorescence signal given in fluorescence units (fu) in the range of mNG detected for cultures of *T. pseudonana* transformants (mNG-Tp23191) after the insertion of integrated fusion protein. A wild type of *T. pseudonana* (TpWt) was used as a negative control.

6.3 Visualization of mNG-Tp23191 in *T. pseudonana* Transformants

Microscope studies were conducted to get an impression of how often the fusion protein is expressed in *T. pseudonana*, and the location of fusion protein within cells at different stages in the cell cycle. Thus, *T. pseudonana* cells from the second generation of transformants were examined with fluorescence microscopy and CLSM.

Cells from mNG-Tp23191-7 imaged with fluorescence microscopy are shown in Figure 6.3.1. Fluorescence signals within the range of mNG are colored green, while the autofluorescence from the chloroplast is colored red. By comparing the fluorescence signals detected with the different optical filters, there was a complete overlap. Thus, it was not possible to draw any conclusions considering the expression of fusion protein mNG-Tp23191. Twelve new clones (mNG-Tp23191-13 to 24) were picked from the plates, and several of them were examined with a fluorescence microscope, but none of them showed any signs of mNG-Tp23191. As all showed the same, images of three other transformants from the second transformation are given in Appendix D.4.

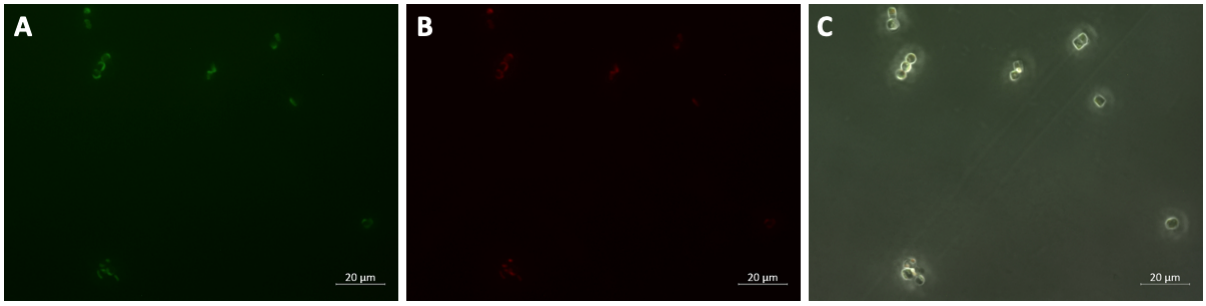

Figure 6.3.1: Visualization of *T. pseudonana* transformants with fusion protein mNG-Tp23191. All images show the same group of cells, but with different settings on the fluorescence microscope. Detected fluorescence signal between 505-555 nm is shown in **A**, while fluorescence signal above 650 nm is shown in **B**. **C**) The two channels of fluorescence signals are merged on top of a bright-field microscope image, which makes it possible to see the overlap.

Three cells from mNG-Tp23191-8 imaged with CLSM are shown in Figure 6.3.2. Both the girdle band view and the valve view are visualized. As seen from Figure 6.3.2, there was a complete overlap of the fluorescence signal with the two optical filters. Based on earlies observations, mNG-Tp23191 has been located in the diatom cell wall, and the protein is not expected to be located within the chloroplast. Thus, it was be concluded that there was no sign of fusion protein within any of the cells.

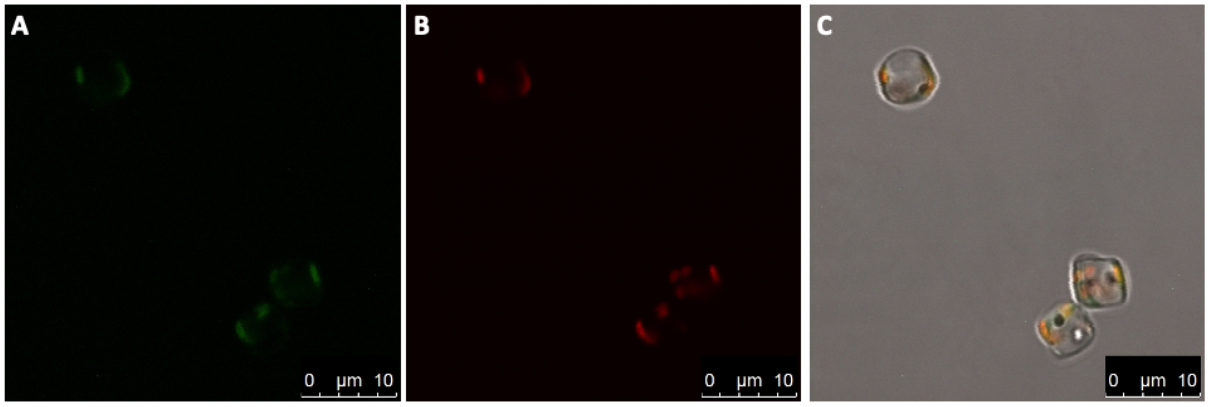

Figure 6.3.2: Visualization of three *T. pseudonana* cells with pTpPuc3-mNG-Tp23191. All images show the same group of cells, but with different settings on the CLSM. The upper-left cell is shown in the valve view while the two cells in the right corner are in the girdle band view. Fluorescence from mNG (colored in green) and autofluorescence (colored in red) are shown in **A**) and **B**), respectively. **C**) Bright-field microscope image, visualizing the whole cell. The other fluorescence channels are also included, making it possible to detect the location of expressed mNG-Tp23191.

6.4 DNA Analysis of *T. pseudonana* Transformants

After the discovery of no visible fusion protein present in the first generation and second generation of *T. pseudonana* transformants, a genomic analysis was conducted to investigate a possible plasmid loss or a default in the mNG-Tp23191 construct on pTpPuc3. Thus, DNA analysis on second generation transformants was performed with PCR and agarose gel electrophoresis. mNG-Tp23191-7 and 8 are denoted *a* and *b* in all gel images given below. DNA from TpWt was used as a negative control and is referred to as *w*. Five different reactions were conducted, and the different wells are denoted with their respective reaction number. *NrsR* was amplified in the first reaction, while different parts of the fusion protein were amplified in reaction 2-5. An illustration of the amplified regions on the fusion protein is given in Figure 6.4.1. The primers used for the firth and fifth reactions are complementary regions of *Tp23191*. Therefore, two amplicons were expected; one from the plasmid and the other from genomic DNA. As *mNeonGreen* has a length of 733 bp, the amplicon originating from the fusion protein should be 733 bp larger than the amplicon from genomic DNA. Lengths of the expected amplicons are listed in Table 6.4.1.

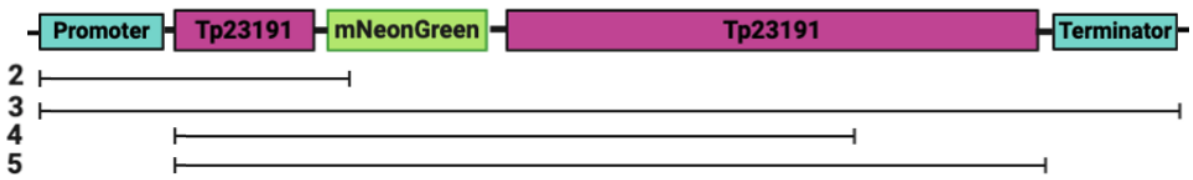

Figure 6.4.1: Expected DNA fragments from the fusion protein mNG-Tp23191 after four different PCRs.

Table 6.4.1: The expected lengths for each DNA fragment after five different PCRs. Fragment 4 and 5 are amplified with primers complementary to regions of the gene Tp23191. Thus, two different fragments are expected; a larger fragment from the fusion protein and a smaller fragment from genomic DNA.

Number	Template	Length [bp]
1	NrsR	211
2	Parts of mNG-Tp23191	1653
3	mNG-Tp23191	3769
4	Parts of Tp23191	1726, 993
5	The whole Tp23191	2299, 1566

With Gene Ruler (L) as a reference, the size of the different fragments was predicted and compared to the expected sizes. The sizes of some of the most intensive ladder bands are given in bp, see Appendix C.3 for all band sizes. The most significant observation was that amplicons appeared to be of a larger size than expected. As this trend was observed among all PCR reactions, it was presumed to be a systematic error, and this was taken into account when gel images were analyzed.

Gel images of PCR products for reaction 1-3 are given in Figure 6.4.2. Visible bands for the first PCR reaction (Figure 6.4.2, 1) indicated that *NrsR* was successfully amplified for mNG-Tp23191-7 and 8, but not for TpWt. For the second PCR (Figure 6.4.2, 2), all samples had a similar band of approximately 2500-2600 bp. Additionally, the two transformants had a band of size 1200 bp. None of these band sizes fitted the expected DNA fragment of 1653 bp. Thus, the results from the second PCR were inconclusive. For the third reaction (Figure 6.4.2, 3), no bands had occurred on the sample of TpWt. The two transformants had a large band on 6000 bp and 4000 bp, where the latter band may be the fusion protein, which should be of size 3769 bp. Moreover, two bands of size 1800 bp and 1400 bp were visible in the reactions for the two transformants, but with a weaker intensity, indicating that the primers had bound to something, but what exactly was unknown.

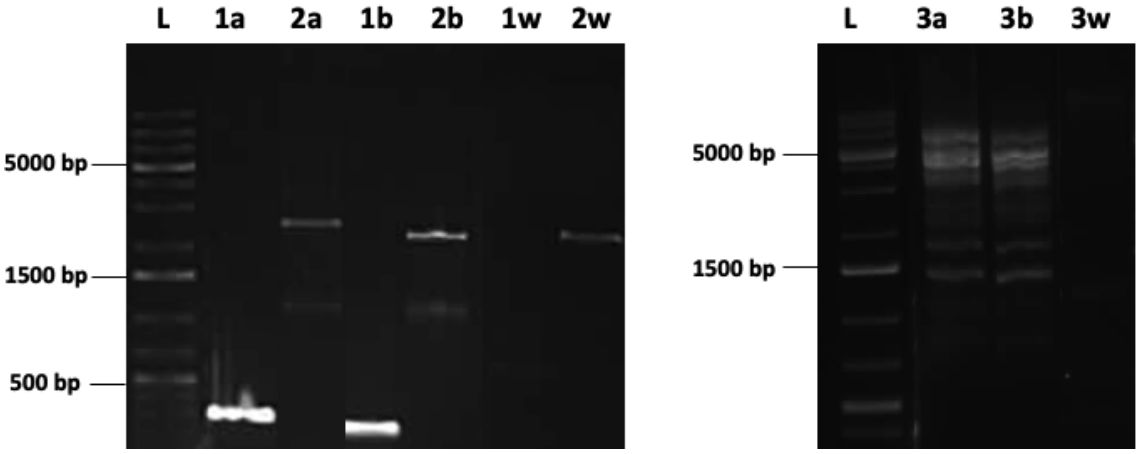

Figure 6.4.2: Amplified DNA fragments from PCRs were analyzed with agarose gel electrophoresis. This gel image shows the DNA ladder (L), in addition to the results after amplification of gene *NrsR* (1), parts of mNG-Tp23191 (2) and the whole fusion protein (3). Transformants are denoted *a* and *b*, while wild type *T. pseudonana* is referred to as *w*.

Amplicons from PCRs 4 and 5 are visualized in Figure 6.4.3. The two transformants had three bands of similar sizes for both of the reactions. Therefore, it is reasonable to believe that the amplicons from the transformants in reaction 4 were identical (Figure 6.4.3, 4), and the amplicons from the transformants in reaction 5 were identical (Figure 6.4.3, 5). Moreover, the smallest band was also present in TpWt for reactions 4 and 5, which indicated that the smallest size amplicons in all reactions originated from *Tp23191* located on the genomic DNA. As TpWt only had one visible band, the other products among the transformants suggestively originated from plasmid DNA. When considering the systematic error, the middle band in both reactions fits the size of the gene fusion mNG-Tp23191.

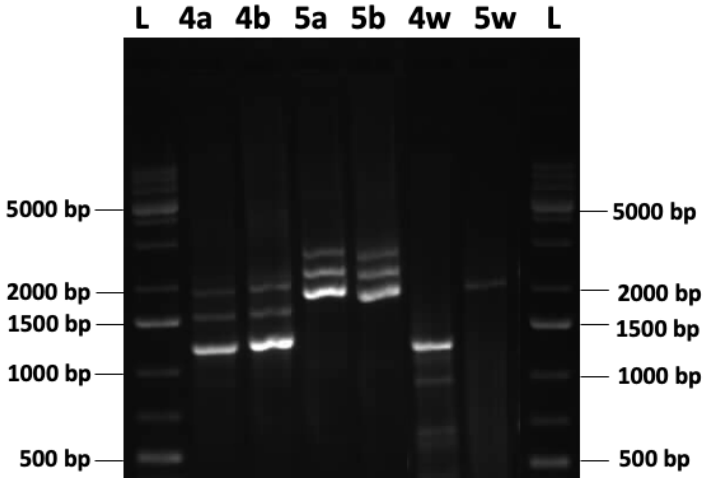

Figure 6.4.3: Amplified DNA fragments from PCRs analyzed with agarose gel electrophoresis. This gel image shows the DNA ladder (L) and the different amplicons when *Tp23191* is used as template. Transformants with integrated plasmid are denoted *a* and *b*, while wild type *T. pseudonana* is referred to as *w*.

Amplicons expected to originate from the plasmid were isolated from the gel and analyzed with Sangers sequencing. The results were aligned with the expected nucleotide sequences from the construct mNG-Tp23191, but all results were inconclusive. Thus, they were not included. In summary, the results from the DNA analysis led to the assumption that *NrsR*, and the gene fusion *mNG-Tp23191* was still present in *T. pseudonana* transformants. Nevertheless, the results neither confirmed nor disproved that a rearrangement in the plasmid conformation had happened.

6.5 Expression of mNG-Tp23191 in *T. pseudonana* Transformants

When new transformations were made, the first generation transformants were moved to a cabinet with approximately no light and 13°C. As these conditions result in cell arrest, regular addition of nutrients and seawater was not necessary. After two months, mNG-Tp23191-4 and mNG-Tp231911-11 were examined with FCM and microscopy. This revealed unexpected results. The mean fluorescence signal was considerably larger than the fluorescence signals detected at the same time as the synchronization studies were conducted (Figure 6.5.1).

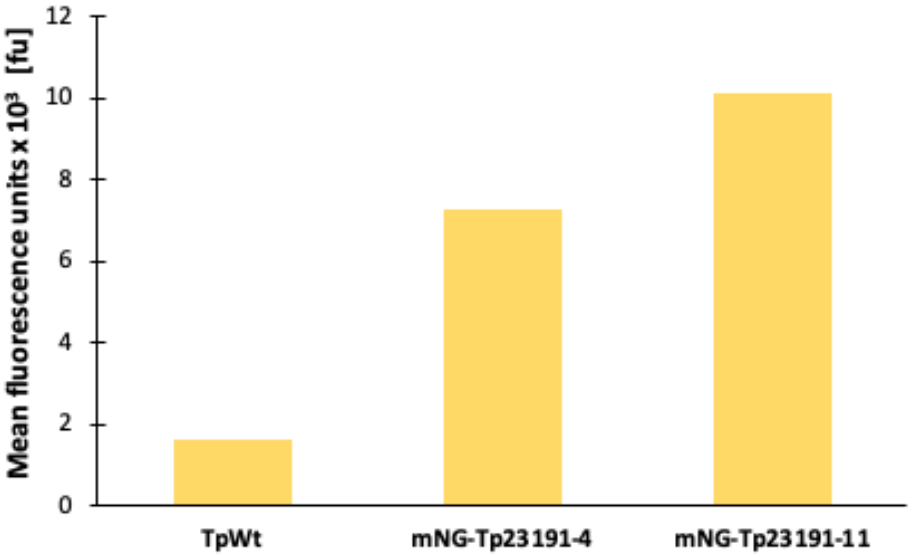

Figure 6.5.1: Mean fluorescence signal given in fluorescence units (fu) detected for the first generation of *T. pseudonana* transformants after two months incubation in darkness and at 13°C.

The presence of mNG-Tp23191 in transgenic lines of *T. pseudonana* was confirmed with CLSM and fluorescence microscopy. For images from both microscope studies, the fluorescence signals within the range of mNG are colored in green, while the autofluorescence is colored red. Fluorescence microscopy showed that numerous cells expressed the fusion protein and with different intensity (Figure 6.5.2). CLSM images of a cell in valve view is shown in Figure 6.5.3.A-C, and a cell in the girdle band view is shown in Figure 6.5.3.D-F. As there was no complete overlap of fluorescence signals within the range of mNG and autofluorescence, the fusion protein was present in both cells. The bright-field microscope images (Figure 6.5.3C,F) visualized mNG-Tp23191 in parts of the two cells outline. Moreover, the intracellular location of mNG-Tp23191 was consistent with the location of the valve and girdle bands.

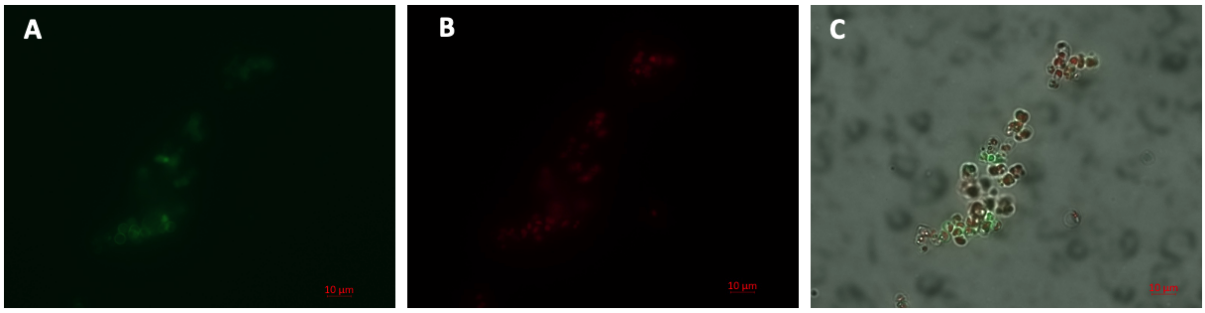

Figure 6.5.2: Visualization of *T. pseudonana* transformants with fusion protein mNG-Tp23191 imaged with fluorescence microscopy. All images show the same group of cells, but with different settings on the fluorescence microscope. Detected fluorescence signal between 505-555 nm is shown in **A**, while fluorescence signal above 650 nm is shown in **B**. **C**) The two channels of fluorescence signals are merged on top of a bright-field microscope image, which makes it possible to detect the localization of mNG-Tp23191.

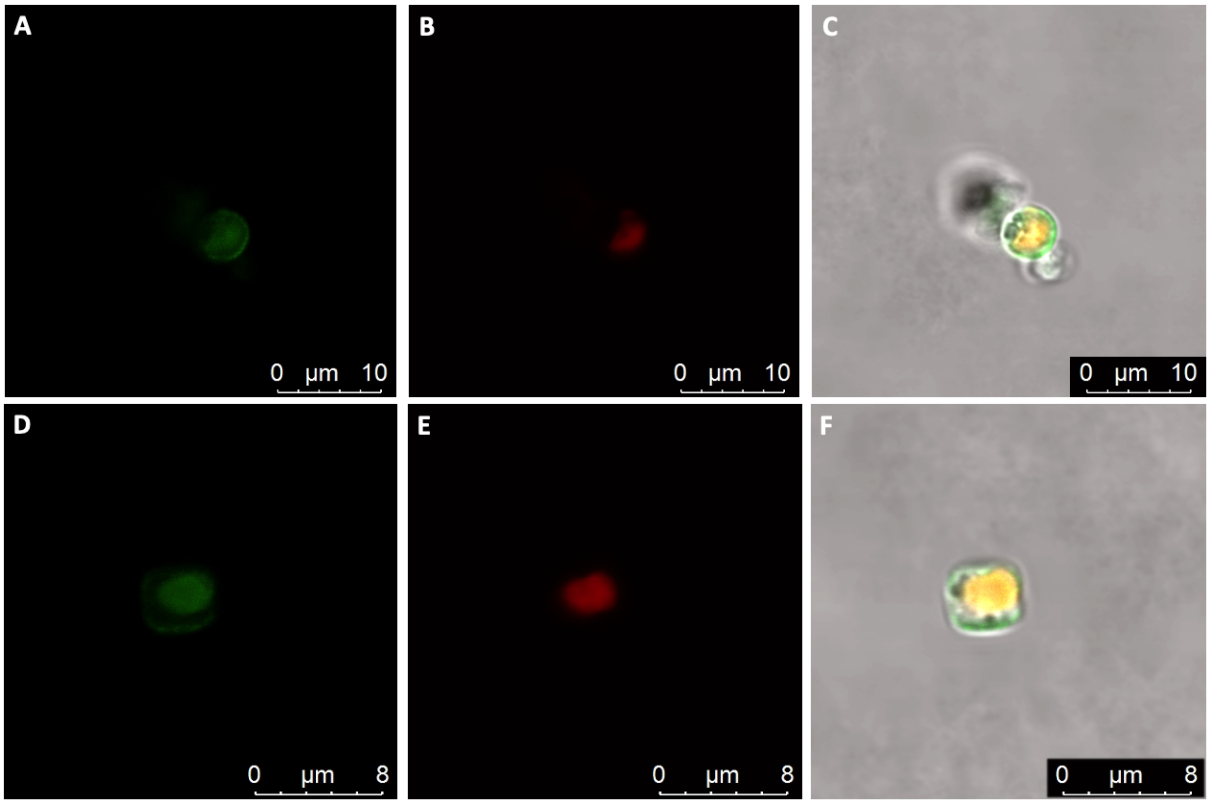

Figure 6.5.3: Visualization of two *T. pseudonana* cells from mNG-Tp23191-11 with integrated fusion protein mNG-Tp23191 imaged with CLSM. **A-C**) A cell is shown in valve view. **D-F**) A cell is shown in girdle band view. Fluorescence detected within the range of mNG (colored in green), and autofluorescence (colored in red) is shown in the left and middle images, respectively. The image to the right is a bright-field microscope image. The fluorescence signals are also included, which makes it possible to detect the location of mNG-Tp23191.

6.6 The Impact of Cytoskeleton Inhibition on *T. pseudonana*

To get an insight into how different cytoskeletal elements impact *T. pseudonana* frustule assembly, *T. pseudonana* cultures were treated with different microfilament and microtubule inhibitors.

6.6.1 Determination of Proper Inhibitor Concentrations

Titration was performed to determine the concentration of inhibitors at which cell growth was reduced but not stopped. Graphical representations of the change in concentration of live cells as a function of time for all treatments are given in Appendix D.5. The percentage of growth for all concentrations of each inhibitor treatemnt, compared to a culture of TpWt under optimal growth conditions, showed that the cultures were differently affected (Table 6.6.1). As the second generation transformants had no visible signs of mNG-Tp23191, the inhibition experiment and further examination with SEM was only conducted with TpWt. For this reason, only the percentage of growth for TpWt was considered when proper concentrations were determined. The different cytochalasin D concentrations did not result in significant differences in growth among TpWt. Thus, a concentration of 6.0 μM was chosen for further inhibitor treatment. Colchicine (40 μM) and oryzalin (0.2 μM) were chosen for further inhibitor treatments, as they would presumably result in 30-50% of optimal growth.

Table 6.6.1: The percentage of growth for two transformants (mNG-Tp23191) and one wild type of *T. pseudonana* (TpWt) when compared to a TpWt under normal growth conditions.

Inhibitor	**Cytochalasin D**				**Colchicine**				**Oryzalin**			
Concentration [μM]	1.5	3.0	6.0	12	25	50	100	200	0.1	0.2	0.4	0.8
TpWt [%]	51	50	51	50	50	24	6	6	51	50	6	6
mNG-Tp23191-7 [%]	88	89	89	30	85	5	3	3	89	29	6	6
mNG-Tp23191-8 [%]	48	32	32	4	30	5	3	3	95	12	6	6

6.6.2 The Change in Fluorescence Pattern During Cytoskeleton Inhibition of *T. pseudonana* Transformants

The chemicals cytochalasin D, colchicine, and oryzalin induce different cell cycle arrest points. Cytochalasin D causes cell cycle arrest at the G_1-S boundary [133], while colchicine and oryzalin cause a block at the G_2-M boundary [134, 135]. For all inhibitor treatments, the detected mean fluorescence signal within the range of mNG was remarkably higher for *T. pseudonana* transformants, compared to TpWt. The fluorescence pattern for the highest concentrations of inhibitors as a function of time is given in Figure 6.6.1. The fluorescence signal within the range of mNG was approximately constant for mNG-Tp23191-7 and 8 during the treatment with microfilament inhibitor cytochalasin D (Figure 6.6.1.A). On the contrary, the two microtubule inhibitors, colchicine, and oryzalin, resulted in an increased fluorescence signal in the range of mNG for the two transformants (Figure 6.6.1.B-C). Moreover, it was observed that the fluorescence signal in the range of mNG was remarkably increased for transformant mNG-Tp23191-8 from 24 h to 48 h of incubation with oryzalin (0.8 μM).

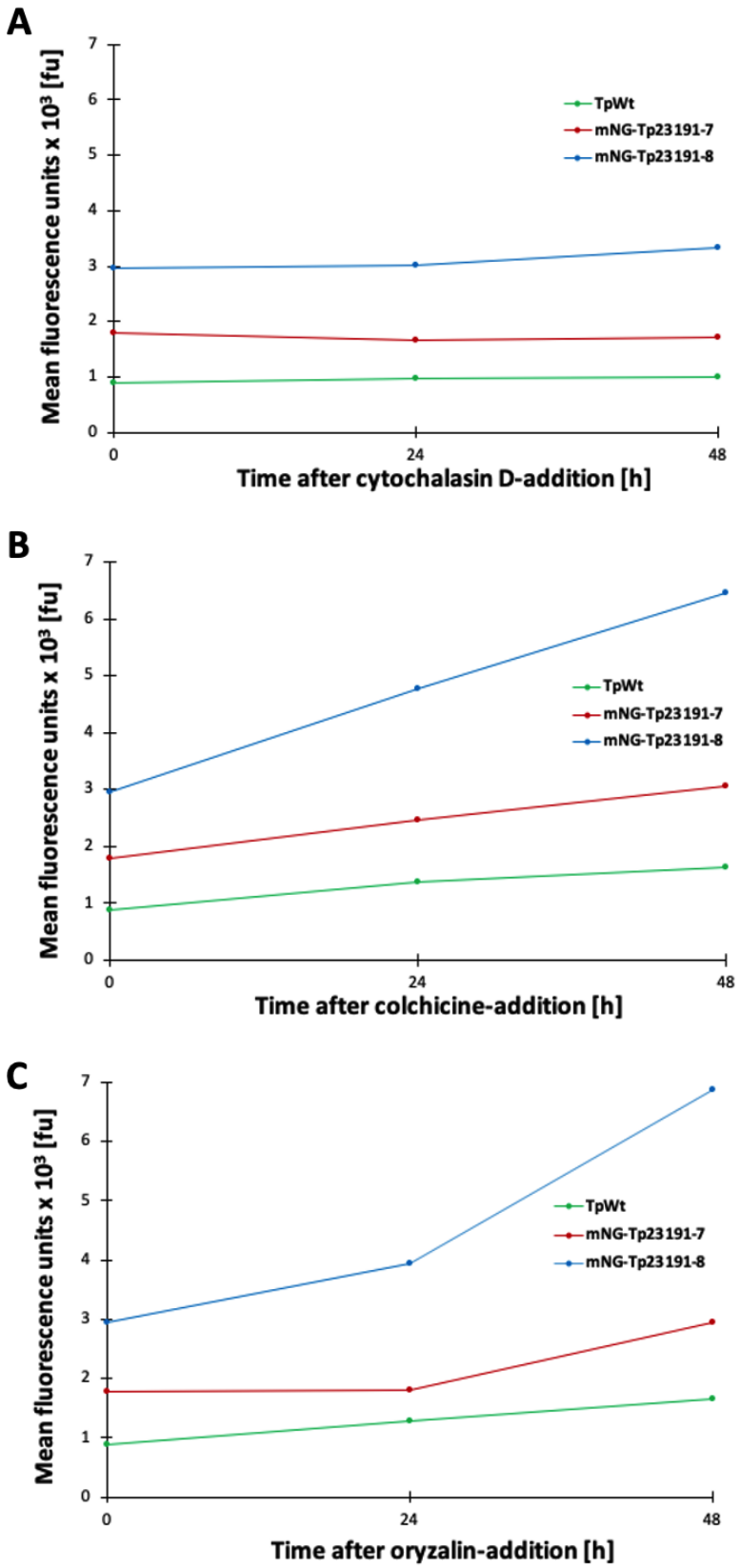

Figure 6.6.1: *T. pseudonana* cultures treated with inhibitors of the cytoskeleton for 48 h. The change in detected mean fluorescence signal in the range of mNG as a function of time. Wild types are denoted TpWt, while transgenic lines with fusion protein are denoted mNG-Tp23191. **A**) Cytochalasin D [12 μM]. **B**) Colchicine [200 μM]. **C**) Oryzalin [0.8 μM].

6.6.3 The Impact of Microfilament and Microtubule Inhibition on Frustule Morphology

Cultures of TpWt treated with cytochalasin D (6.0 μM), colchicine (40 μM), and oryzalin (0.2 μM) and TpWt without inhibitor were cleaned in two rounds to remove organic material. During the SEM examination, it was observed that most frustules were crushed or deformed. They were merged in a complex network and partly covered in an unknown soft material, which might have been a biofilm.

Special attention was paid to imaging valves, but also girdle bands were imaged. No pre-synchronization in growth was conducted before the inhibitor treatment. Thus, cells were at different cell cycle stages when treated, and this was taken into account when SEM images were examined. Table 6.6.2 summarizes the most prominent differences of *T. pseudonana* frustule morphology observed from SEM images. The average number of rimoportulae in all treatments did not indicate any deviations and are thus not included in Table 6.6.2. The numbers of rimoportulae on frustules for all inhibitor treatments are given in Appendix D.6. Moreover, a fraction of the intact frustules in all samples looked like they were untreated or undertreated. Figure 6.6.2 includes frustules with visible deviations in frustule morphology compared to *T. pseudonana* cells without inhibitor treatment. Each row shows frustules with the same treatment. The first two columns show predominant morphology in valve view, while the last column show closed up images of morphological details.

Table 6.6.2: Observations of frustule morphology after treatment of *T. pseudonana* with different cytoskeleton inhibitors. No treatment (None), cytochalasin D (Cyt D), colchicine (Colc), oryzalin (Oryz).

Frustule morphology		**Treatment**			
Elements	Observations	None	Cyt D	Colc	Oryz
Fultoportulae	None	-	4/13	3/17	4/16
	One	11/11	9/13	10/17	12/16
	Two	-	-	3/17	-
	Three	-	-	1/17	-
Rimoportulae	Overgrowth and/or deformed	3/11	4/13	7/17	10/16
Costa and cross-connections	Overgrowth and/or reduced pattern	2/11	8/13	12/17	10/16
Girdle bands	Lack in pore pattern	-	3/13	9/17	6/16

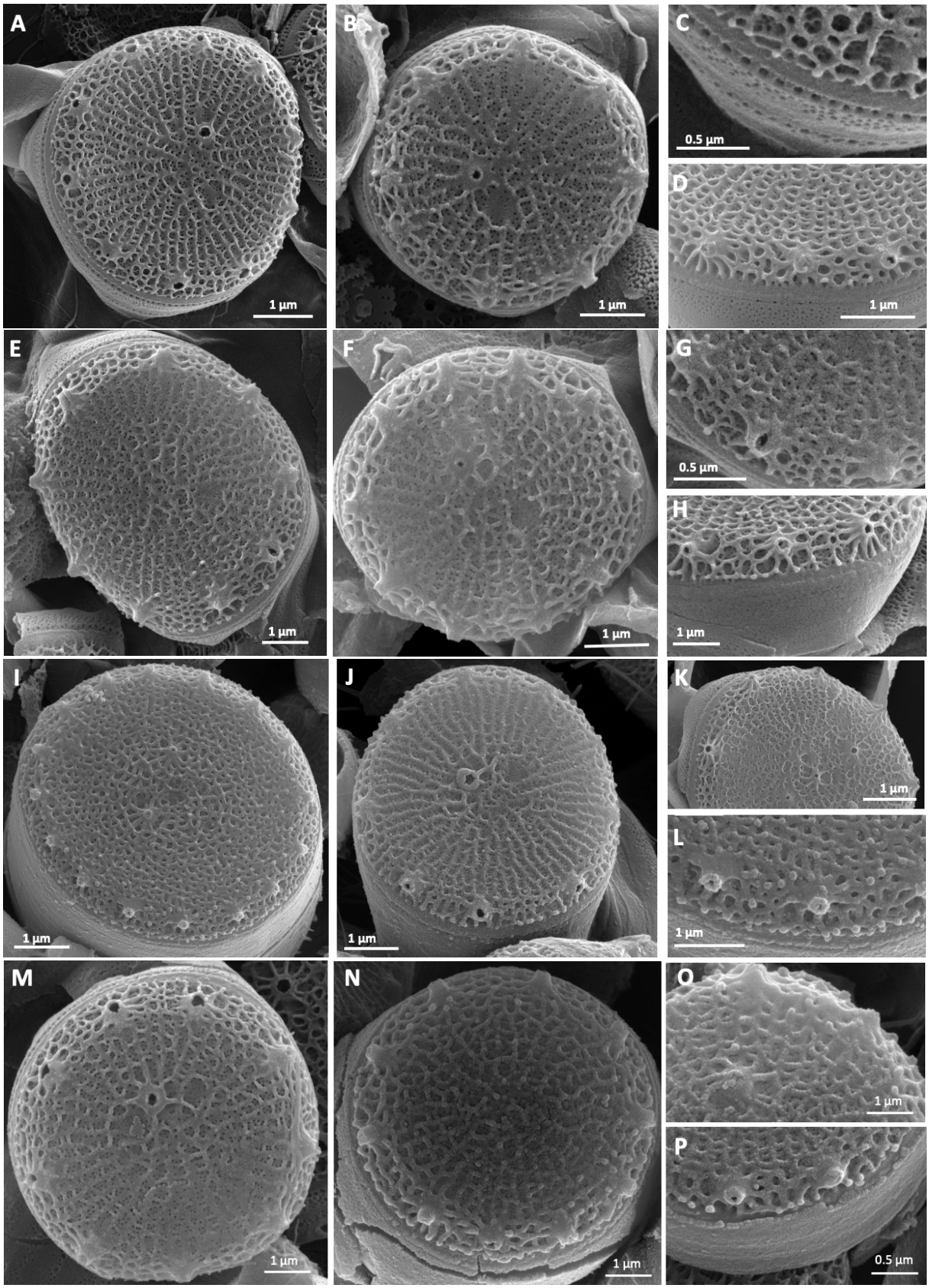

Figure 6.6.2: SEM images of *T. pseudonana* frustules. Valve view with the predominant morphology is given in images to the left and the middle, while close up images are given to the right. **A-D**) No treatment. **E-H**) Treatment with the microfilament inhibitor cytochalasin D. **I-L**) Treatment with the microtubule inhibitor colchicine. **M-P**) Treatment with the microtubule inhibitor oryzalin.

Untreated *T. pseudonana* frustules are shown in Figure 6.6.2.A-D. All examined frustules had one fultoportula, and girdle bands with visible pores. The majority of frustules had a morphology similar to the frustule visualized in Figure 6.6.2.A, with a well-defined costa and cross-connections, visible cribrum pores and a defined pattern of pores on valvocoupla (Figure 6.6.2.C). However, some frustules had silica overgrowth and a reduced pattern on the rim (Figure 6.6.2.B). Most of the portulae were wide, while others were smaller in diameter and shaped like a turtle-neck (Figure 6.6.2.D).

Frustules in Figure 6.6.2.E-H, had been exposed to microfilament inhibitor cytochalasin D, which hinders actin polymerization. The fultoportula was absent among 4/13 frustules (Figure 6.6.2.E). Some frustules had fultoportula, but with abnormal morphology (Figure 6.6.2.F). These cells were presumably exposed to cytochalasin D when the valve structure was partly developed. Additionally, silica overgrowth on the rim and rimoportulae were observed among the majority of the frustules (Figure 6.6.2.G). 3/17 frustules had an abnormal girdle band structure, with reduced pore pattern and an absent line of pores in valvocoupla (Figure 6.6.2.H).

Frustules exposed to microtubule inhibitors colchicine and oryzalin are shown in Figure 6.6.2.I-L and Figure 6.6.2.M-P, respectively. About half of the examined frustules treated with microtubule inhibitors had girdle bands with a smooth structure with no visible pores or less defined pores (Figure 6.6.2.P,I). Inhibition of microtubule polymerization with colchicine resulted in an increased number of fultoportulae. 3/17 frustules had two fultoportulae, while one frustule had three linearly ordered fultoportulae (Figure 6.6.2.K). 12/17 frustules had a deformed valve structure, with non-observable cribrum pores, due to thick costae and cross-connections (Figure 6.6.2.L). Small portulae with overgrowth of silica Figure 6.6.2.I), and larger, deformed portulae (Figure 6.6.2.J) were observed. Treatment with oryzalin, which depolymerizes microtubules, resulted in 10/16 frustules with deformed valve structures. Silica overgrowth predominated, and both portulae, costae, and cross-connections were deformed (Figure 6.6.2.M,O). Additionally, 4/16 frustules lacked fultoportula (Figure 6.6.2.N).

In summary, all treatments with the cytoskeletal inhibitors resulted in phenotypes with reduced pore pattern in the girdle band structure, frustules without fultoportula, deformed rimoportulae, and silica overgrowth on costae and cross-connections. The morphological changes observed on frustules pre-treated with drugs that inhibited microfilaments and microtubules indicate how these cytoskeletal elements contribute to *T. pseudonana* frustule assembly.

Chapter 7

Discussion of Laboratory Research

The present laboratory research aimed to understand better how silicanin Tp23191 is expressed in *T. pseudonana* by mapping the expression pattern of the mNG-Tp23191 fusion protein in transgenic lines and relating these results to stages and events of the cell cycle. By treating *T. pseudonana* cultures with drugs that inhibit microtubules and microfilaments, it was investigated how elements of the cytoskeleton participate in frustule assembly in *T. pseudonana*. The main findings are discussed in the following sections.

7.1 Synchronized Growth of *T. pseudonana* Transformants

The attempts of synchronized growth conducted herein were based on the Si-starvation/ replenishment procedure developed by Hildebrand and Frigleri [57]. The unsuccessful synchronized cell cycle arrest after 24 h with Si-starvation was unexpected, as it was not in coherence with the previous *T. pseudonana* synchronization studies conducted with the same protocol [35, 48, 50, 57, 139]. Different growth medium and aeration by stirring have been hypothesized to be important factors in achieving synchrony [57]. However, as cells were kept on continuous stirring during Si-starvation, it is not likely that these factors were the only reasons for the delay in cell cycle arrest [57]. The third attempt of synchronization was considered successful, although only cultures of transgenic lines appeared to be synchronized. It was surprising to find that transgenic lines had obtained cell cycle arrest after 30 h, while TpWt remained unsynchronized after 48 h of incubation. This deviation may be due to a lower tolerance of limited growth conditions among transgenic lines due to the previous exposure to ntc. Nevertheless, it does not explain why TpWt was unsynchronized after a doubling in time of Si-starvation compared to the original protocol [57]. The varying duration time of Si-starvation necessary to achieve cell cycle arrest observed in this study indicates that the developed synchronization procedure is not optimal. Hence, for future synchronization studies, it is suggested to monitor the change in cell density during Si-starvation to ensure that cells have stagnated in growth before Si-addback.

Since only transgenic lines from the third synchronization study appeared to be synchronized, the data retrieved from mNG-Tp23191-4 and 11 was the main focus for further discussion. For both transformants, a peak in cell division was observed 7 h after Si-addback, and 80% of the cells had divided. This is in accordance with the previous successful *T. pseudonana* synchronization studies, where a doubling in cell concentration had occurred after 8 h [23,

48, 57]. From literature, when cells are synchronized in early G_1, girdle band creation starts immediately after Si-replenishment and continues for 3 h, while valve creation occurs after 4 h and continues until cells undergo cytokinesis [48]. In the study by Hildebrand et al., cell cycle arrest at early G_1 phase predominated, and a peak in cell division was observed at 6 h [57]. By considering this when interpreting the results herein, it is possible that: (1) Most cells were arrested in the early G_1 phase, and the one hour delay in cell division was due to insufficient aeration. This argument is consistent with the findings of Hildebrand et al., who observed a 2 h delay of valve synthesis among cultures with inadequate air supply [57]. (2) The prolonged Si-starvation led to a stagnation in late G_1 amongst the majority of the cells. This is in agreement with another observation made by Hildebrand et al., where cells were synchronized in late G_1 or near the G_1-S boundary, and most cells had passed cytokinesis 6 h after Si-addback [57].

Based on changes in cell concentration during the timelapse detection, it is believed that cells had arrested at different cell cycle stages [23, 57]. The 21-22% increase in cell density and the 6-7% decrease in mean cell size observed the first hour, suggest that a fraction of cells arrested in the G_2-M boundary and completed cytokinesis the first hour. This is not in accordance with the cell cycle determinations conducted by the NovoCyte software, which predicted that only a small fraction of cells had obtained cell cycle arrest in G_2+M. A possible explanation is that the manual gating led to an underestimation of cells in G_2+M. Some of the changes in cell distribution calculated by NovoCyte differs from the findings by Hildebrand et al. [57]. Herein, the number of cells in G_1 was never below 36%, and it was no significant peak of cells in G_2+M. However, our peak in S phase 2-3 h after Si-addition, is partly consistent with the peak of cells in S phase 3-4 h after Si-addition observed by Hildebrand et al. [57].

NovoCyte software predicted that the same fraction of cells (40-42%) had obtained cell arrest in the S phase, both for transgenic lines and TpWt. An equal distribution of cells for both synchronized and unsynchronized cultures is unlikely, and these results strengthen the assumption that the calculation was not completely accurate. From literature, between 13-23% of cells had arrested in the S phase with the same synchronization procedure [57]. Additionally, the long S phase does not coincide with the estimated duration of the S phase, which is between 1-1.5 h in cells of *T. pseudonana* [139]. Based on this, it is suggested that the software had overestimated the number of cells in the S-phase, especially at the first measurements, which might be due to the uneven distribution of cells in the different cell cycle phases. Overall, the combined results presented herein indicate that the majority of cells were arrested in G_1. With the assumption that the cells were synchronized in growth throughout the timelapse detection, girdle band creation predominated the first hours, while valve creation predominated a few hours before the sharp increase in concentration at 6-7 h.

7.2 The Change in Expression Level of mNG-Tp23191 in *T. pseudonana* Transformants

Synchronized cell cycle arrest was conducted such that the expression of the mNG-Tp23191 fusion protein could be examined at different cell cycle stages in transgenic lines of *T. pseudonana*. Analysis of data from the third synchronization study revealed a low detection of fluorescence signal within the range of mNG. Compared with the previous synchronization study conducted with the same transgenic lines before this thesis [1], the detected fluorescence signal within the range of mNG was remarkably lower for all measurements, and the highest detected

signal was 4-5 times lower than previously observed (See Appendix E). The lack of detectable fusion protein was confirmed with microscope studies and western blot. Because of the constant exposure to ntc, a plasmid loss was unlikely. A possible persistent defect in pTpPuc3-mNG-Tp23191 was contradicted with the unexpected discovery of visible mNG-Tp23191 in the same transformants two months after the synchronization studies were conducted (Section 6.5). FCM showed a remarkable high fluorescence signal within the range of mNG for both transformants, while microscope studies revealed that numerous cells from both transgenic lines expressed mNG-Tp23191 at different intensities. Moreover, the fusion protein was localized in the frustule - both in valves and girdle bands. Despite this, the circular dots of fusion protein that were presumably consistent with the intracellular location of SDV previously observed during the specialization project were not observed herein (Figure 6.5.3) [1]. These observations indicate that the expression level of mNG-Tp23191 had increased after being kept in darkness at a low temperature for two months, but it was not on the same level as before.

The cause of the change in gene expression of mNG-Tp23191 in first generation *T. pseudonana* transformants, is unknown. Overexpression of genes can affect the total protein translation upon what is normal [115, 116], and the overexpression can inhibit or activate other proteins or pathways which again can result in a downregulation of the gene overexpression [115]. However, as the first transformants had visible fusion protein for months, it is unlikely that the undetectable mNG-Tp23191 was due to overexpression. From literature, it is known that epigenetic changes have a central role in the activation and deactivation of genes. The expression of genes can be influenced by both internal changes inside the organism and external changes in the environment [140]. Thus, it is possible that gene silencing occurred as a result of epigenetic modifications. Prior to the synchronization studies, nutrients were not added to mNG-Tp23191-4 and 11 for a longer period (Tore Brembu, personal communication). Thus, they were in bad shape, and frequent dilution of cultures with f/2 medium was necessary before synchronization studies were conducted. Similarly, clones from the second transformation were kept in a poor nutrient environment for 34 days, before they were grown in larger culture flasks. In hindsight, it is reasonable to believe that the limited nutrient availability triggered stress, which induced an epigenetic change in all transgenic lines. This suggestion can explain why the expression level of mNG-Tp23191 was decreased to such a big extent that the fusion protein was no longer visible in first generation transformants, and that the fusion protein was never observed in second generation transformants. It is not known if the fusion protein was visible in a short time after the transformation, as no analysis was performed due to COVID-19 restrictions.

DNA methylation is a highly conserved epigenetic modification found in a wide range of eukaryotic organisms, diatoms included [141, 142]. Several putative cytosine-5 DNA methyltransferases (C5-MTases) homologs have been found in *T. pseudonana*, which can catalyze *de novo* methylation on previously unmethylated cytosine residues [143]. This mechanism prevents the methylated sequence from being expressed [144], and can thus be reversed by DNA demethylase activity [145]. As far is known by the author, DNA demethylases have not yet been characterized in *T. pseudonana*. However, if gene silencing occurred as a result of DNA methylation, it is reasonable to believe that the re-detection of mNG-Tp23191 in first generation transformants was due to a reversed repression caused by DNA methylases. Little is known about the organization of artificial plasmids in diatoms, whether they remain circular or are arranged on nucleosomes. Nevertheless, the low GC-content in the CAH-cassette on pTpPuc3 functions as centromeres and enables plasmid maintenance in diatoms as an extra chromosomal plasmid [114]. If the plasmid is organized on nucleosomes, like observed in mammalian cells

[146], it might be possible that post-translational acetylation of histones induced by an external factor [147], led to the silencing of mNG-Tp23191. If the change in expression was due to this epigenetic change, deacetylation must have reversed the repression in first generation transformants. Nevertheless, the fusion protein is still not seen in the transgenic lines from the second transformants, and it would be interesting to see if the expression level will change in the future.

Given that no visible signs of mNG-Tp23191 were present when cells from transgenic lines were examined with microscopy in this study, changes in mean fluorescence signal within the range of mNG during the inhibitor titration were unexpected. A putative correlation between fluorescence signal and cell cycle arrest was seen in cultures of transgenic lines treated with cytoskeleton inhibitors. The detected fluorescence signal was approximately constant when transgenic lines were treated with microfilament inhibitors, which causes cell cycle arrest at the G_1-S boundary [133]. This was in contrary to both treatments with microtubule inhibitors, which had a significantly higher detection of the fluorescence signal (Figure 6.5.1). It is known that both chemicals cause a block in the G_2-M boundary [134, 135]. In this study, a reduction in detected fluorescence signal within the range of mNG was observed the first hour after Si-replenishment in the third synchronization study. Based on the assumption that a fraction of cells divided the first hour, this decrease in fluorescence signal suggests a more significant expression of mNG-Tp23191 in late G_2+M compared to early G_1. In total, these observations were quite interesting and strengthen the hypothesis that the mNG-Tp23191 fusion protein is present in the G_2 phase of the cell cycle when the valve is assembled inside the valve SDV. This is coherent with previous assumptions made during the specialization project [1]. However, no conclusion could be drawn considering the remarkable pattern of fluorescence as neither mNG-Tp23191 was visible under a microscope nor confirmed with western blot.

7.3 The Impact of Microtubule and Microfilament Inhibitors in *T. pseudonana*

The study of how elements of the cytoskeleton affect biosilica assembly in *T. pseudonana* suffers from several limitations. These limitations were notably related to only a small number of frustules being imaged as most frustules were deformed or crushed, and only one parallel was performed due to the lack of time. In order to remove a sufficient amount of organic material prior to SEM, the cleaning protocol was implemented twice. Some of the mechanical damages were probably due to random collisions between frustules during pre-treatment [138]. However, it is believed that the large fraction of destroyed frustules was due to the increased number of washing steps. This assumption is in agreement with Romann et al. [138], which previously stated that a more efficient cleaning protocol would result in more fragile frustules. Moreover, a larger fraction of the intact frustules were apparently untreated or undertreated. Assuming the inhibitor treatment affected the mechanical strength of the cell wall, frustules with phenotypes might have been underrepresented in the series of imaged frustules. *T. pseudonana* cells were not pre-synchronized in growth before the chemicals were added to the cultures. Thus, some differences in frustule morphology are possibly due to cells being at different cell cycle stages when exposed to microtubule and microfilament inhibitors [57]. Also, the inhibitor concentrations affected the degree of morphological changes. Nevertheless, higher concentrations might have resulted in more fragile frustules, or even worse, that frustules would not have occurred if the cells had obtained cell cycle arrest. Differences in frustule morphology resulting from

genetic variations have previously been observed within the same diatom species, included *T. pseudonana* [35]. However, it is unlikely that all morphological variations observed herein were natural, as the examination of treated frustules compared to untreated frustules (Section 6.6.3) showed a similar trend in changes.

All drug treatments resulted in numerous of phenotypes with thecas of less defined structures, including smooth girdle band surfaces with less visible pores, and valves with overgrowth of silica or reduced silica pattern on the rim. These observations are consistent with the previously confirmed impact of microfilaments and microtubules on microscale positioning of biosilica, involving the overall construction of valves and girdle bands, in different diatom species [20, 22, 32]. In this study, overgrowth of silica on costae and cross-connections predominated on frustules treated with the microtubule inhibitors colchicine and oryzalin, while it was observed on a smaller fraction of frustules treated with the microfilament inhibitor cytochalasin D. This observation may indicate that both elements of the cytoskeleton are involved in the formation of ribs, but to varying degrees, in accordance with previous inhibitor treatments of the centric *Cyclotella cryptica* conducted with the same drugs [20]. Previous findings of microtubules in rib structures of centric diatoms support this hypothesis [121, 126]. Based on the knowledge that the formation of ribs is categorized as part of the microscale biosilica pattern, this observation suggests that microfilaments and microtubules contribute to biosilica mesoscale patterns [22]. Additionally, several phenotypes without fultoportula were observed on frustules exposed to all drugs, which led to the suggestion that both elements of the cytoskeleton are involved in forming this morphological structure. The increased number of fultoportulae on frustules treated with colchicine may indicate that the polymerization of tubulin is related to the positioning of fultoportulae *T. pseudonana*. This hypothesis is supported by the observation of the mispositioning of fultoportula on frustules from *C. cryptica* after microtubule inhibitor treatment [20] and previous observations of microtubules in regions consistent with portulae in the centric *Coscinodiscus granii* [22]. Tesson and Hildebrand have previously hypothesized that the fultoportula is formed from an organic complex and that an area without deposited silica defines the structure [20]. Perhaps elements of the cytoskeleton are involved in this putative organic complex?

Another interesting observation was the reduced pattern of pores on girdle bands in several frustules treated with different drugs. From literature, it is assumed that microfilaments are associated with girdle band formation. This knowledge is based on previous inhibitor treatments and direct observations of actin rings and microfilaments in regions consistent with the pore region on the valvocoupla [20, 35]. Based on this, it can be suggested that the lack of pores on girdle bands after treatment with cytochalasin D was due to the inhibition of actin polymerization. A larger fraction of frustules with reduced pore pattern on girdle bands were observed on frustules treated with colcicine and oryzalin. Maybe these deviations in frustule morphology result from microtubules being involved in the assembly of pores in girdle bands of *T. pseudonana*? Previous treatments of microtubule inhibitors have shown that morphological elements are affected differently depending on the diatom species [122, 125], indicating that specific morphological control mechanisms are involved in the morphogenesis occurring in different diatom species. As this is a limited study, the previous suggestions presented herein are based on a small number of examined frustules. Therefore, no conclusions can be drawn considering the specific contribution of microfilaments and microtubules on *T. pseudonana* frustule assembly. The experiment should be replicated in several parallels before the concrete role of microfilaments and microtubules concidering biosilica formation in *T. pseudonana* can be stated. Nevertheless, the

deviations in frustule morphology observed herein provided insight into the potential structural elements that may be affected by the specific elements of the cytoskeleton.

7.4 Further Aspects

For further determination of the functions of silicanin Tp23191, the investigation of the mNG-Tp23191 fusion protein should be replicated with new transgenic lines of *T. pseudonana*. Hence, to neglect the possibility of gene silencing induced by limited nutrient availability, it is suggested that the new cultures are kept under optimal growth conditions with continuously nutrient supply before the experiments are conducted. Moreover, the expression pattern of the fusion protein and subcellular locations at different cell cycle stages can be determined with a timelapse visualization experiment on pre-synchronized cultures, as previously conducted with Sin-1 in *T. pseudonana* [119]. As the cause of the change in the expression of the fusion protein is unknown, other genetic tools should be utilized for further investigation of silicanin Tp23191. The putative association between silicanin Tp23191 and the silicalemma can be confirmed as previously conducted with Sin-1 [119], using the protocol described by Shepperd et al. [148]. In short, the silicalemma is isolated, and a base-treatment will bind putative TM domains to the lipid bilayer. Immunodetection can further confirm or deny if predicted TM domains are integrated into the membrane [149]. Similarly, an immunodetection with an antibody directed against parts of the predicted luminal region of the gene can confirm that parts of the protein are intraluminal [119].

Silicanin knockdown mutants can be generated using RNA interference and RNA antisense approaches [150], while silicanin knockout mutants can be generated using the clustered regularly interspaced short palindromic repeats (CRISPR)/Cas9-based approach [151] recently developed for genome editing in centric diatoms. Tesson et al. have used the former approach for knockdown lines of SAPs [54], while Görlich et al. have used the latter approach for knockout lines of Sin-1 [6] with *T. pseudonana*, both experiments successfully conducted. Understanding the appearance and cellular positioning of frustule elements related to the cell cycle stages in diatoms can be important towards a better understanding of the biosilica formation. Hence, synchronization studies on knockdown lines, followed by an investigation of frustule morphology, may reveal information regarding the putative role of silicanin Tp23191 in biosilica formation.

As previously mentioned, to determine the specific role of the microtubules and microfilaments in *T. pseudonana*, the cytoskeleton inhibitor treatment should be redone with several replicates. It is suggested to pre-synchronize the *T. pseudonana* cultures in growth before a new inhibitor treatment is conducted and that the washing steps and/or concentrations are reduced such that a larger fraction of the frustules are intact at SEM examination. Fluorescent staining of cytoskeleton elements, as previously conducted by Van De Meene and Pickett-Heaps, can confirm the presens of microfilaments and microtubules. For example, microfilaments can be stained with phallodin or phallacidin and microtubules with antibodies, before timelapse CLSM or TEM studies are conducted [121]. Additionally, a combined inhibitor treatment can reveal how the putative interactions between microfilaments and microtubules affect the biosilica formation.

Information regarding the putative association between the cytoskeleton and silicalemma-spanning proteins can be further investigated with inhibitor treatments of silicanin knockdown/knockout lines. Trofimov and coworkers have recently developed an analytic system, the artificial neural network, using *T. pseudonana*, to distinguish differences in morphology in modified frustules

and wild type frustules based on SEM images. The idea is that genotype and phenotype should be linked together by machine learning, and that the software is programmed such that it will automatically recognize pores, and extract pore-related parameters [20, 152]. This program can make it easier to detect deviations in morphology, and are thus valuable during the investigation of organic components putatively involved in the cell wall biomineralization, like the silicanins or elements of the cytoskeleton. Moreover, PDMPO can be used to stain the newly formed silica in the same experiments [22], which can make it easier to confirm if the silicanins or elements of the cytoskeleton is present at the same intracellular locations as to where the biosilica is assembled. A confirmed correlation can suggest some involvement and, thus, facilitate our understanding of the specific role of different organic components.

Chapter 8

Conclusion

The main aim of this thesis was to understand better how nanopatterned biosilica is created in diatoms and the future potential of utilizing diatom frustules in industrial manufacturing of biotechnological applications. Transgenic lines of *T. pseudonana* with fusion protein mNG-Tp23191 were successfully synchronized in growth, and functional studies were conducted. The fusion protein mNG-Tp23191 was localized in the valves and the girdle bands, consistent with previous observations. Unfortunately, no further conclusions of silicanin Tp23191 in *T. pseudonana* could be drawn based on the data presented herein. This was due to the unforeseen reduction in the expression level of mNG-Tp23191, possibly caused by gene silencing induced by unfavorable growth conditions. Transgenic lines treated with microtubule inhibitors, which induce a cell cycle arrest at the G_2-M boundary showed an increased fluorescence signal in the range of mNG, which strengthened the hypothesis that silicanin Tp23191 is present in the G_2 phase of the cell cycle when valves are created in valve SDVs. However, the putative functional role of silicanin Tp23191 in frustule assembly remains unsolved, and further investigation is necessary to conclude whether or not silicanin Tp23191 is involved in biosilica formation. The role of the cytoskeleton in frustule assembly was investigated with inhibitor treatments of *T. pseudonana*. Deviations in morphology on frustules treated with microfilament and microtubule inhibitors led to the assumption that both elements of the cytoskeleton contribute to the biosilica pattern on the meso- and microscale. All drug treatments resulted in several phenotypes with reduced overgrowth on the rim, absent fultoportula, and reducted pattern of pores on the valvocoupla. Thus, microfilaments and microtubules may be involved in the assembly of these elements in *T. pseudonana*. However, as this was a limited study, no conclusions could be drawn, and further investigations are necessary. The literature reviews conducted herein gave an overview of the typical morphological features of diatoms and how frustule assembly is related to the cell cycle. Additionally, it was achieved an insight into the potential use of diatoms in drug delivery systems and immunodiagnostic by immobilization of biomolecules on frustules, which highlighted that genetic manipulation of frustule assembly is valuable for the development of optimally adapted biosilica to the area of application. Diatom biosilica is currently not used in any commercial products, and further *in vivo* studies are crucial towards a future utilization of diatom frustules in biomedical applications. Identifying and characterizing organic molecules putatively involved in cell wall biomineralization in diatoms can give a better understanding of the mechanisms of biosilica formation and make it easier for the future development of environmentally friendly diatom-based applications.

Bibliography

[1] V. Årdal. Functional studies of silicanin Tp23191 in diatom cell wall biomineralization. Project report in TBT4500, Department of Natural Science and Technology, NTNU – Norwegian University of Science and Technology, 2019.

[2] A. Gal, S. Weiner, and L. Addadi. A perspective on underlying crystal growth mechanisms in biomineralization: Solution mediated growth versus nanosphere particle accretion. *CrystEngComm*, **17**(13):2606–2615, 2015.

[3] J.F. Ma. Uptake of silicon in different plant species. E. Bauerlein (Ed.). In *Handbook of Biomineralization*. Wiley-VCH Verlag GmbH. 113–124, 2007.

[4] N. Kröger and N. Poulsen. Biochemistry and molecular genetics of silica biomineralization in diatoms. E. Bauerlein (Ed.). In *Handbook of Biomineralization*. Wiley-VCH Verlag GmbH. 43–58, 2007.

[5] C. Hamm. Interactions between biomineralization and function of diatom frustules. E. Bauerlein (Ed.). In *Handbook of Biomineralization*. Wiley-VCH Verlag GmbH. 83–94, 2008.

[6] S.Görlich, D. Pawolski, I. Zlotnikov, and N. Kröger. Control of biosilica morphology and mechanical performance by the conserved diatom gene *Silicanin-1*. *Communications Biology*, **2**(1):1–8, 2019.

[7] P. Treguer, D.M. Nelson, A.J. Van Bennekom, D.J. De Master, A. Leynaert, and B. Queguiner. The silica balance in the world ocean: A reestimate. *Science*, **268**(5209):375–379, 1995.

[8] N. Kröger and N. Poulsen. Diatoms—from cell wall biogenesis to nanotechnology. *Annual Review of Genetics*, **42**(1):83–107, 2008.

[9] A. Benoiston, F.M. Ibarbalz, L. Bittner, L. Guidi, O. Jahn, S. Dutkiewicz, and C. Bowler. The evolution of diatoms and their biogeochemical functions. *Philosophical Transactions of the Royal Society B: Biological Sciences*, **372**(1728):73–80, 2017.

[10] W.H.C.F. Kooistra. The evolution of the diatoms. E. Bauerlein (Ed.). In *Handbook of Biomineralization*. Wiley-VCH Verlag GmbH. 95–111, 2008.

[11] E.V. Armbrust, J.A. Berges, C. Bowler, B.R. Green, D. Martinez, N.H. Putnam, S. Zhou, A.E. Allen, K.E. Apt, M. Bechner, M.A. Brzezinski, B.K. Chaal, A. Chiovitti, A.K. Davis, M.S. Demarest, J.C. Detter, T. Glavina, D. Goodstein, M.Z. Hadi, U. Hellsten, M. Hildebrand, B.D. Jenkins, J. Jurka, V.V. Kapitonov, N. Kröger, W.W.Y. Lau, T.W. Lane, F.W. Larimer, J.C. Lippmeier, S. Lucas, M. Medina, A. Montsant, M. Obornik, M.S. Parker, B. Palenik, G.J. Pazour, P.M. Richardson, T. Rynearson, M.A. Saito, D.C. Schwartz, K. Thamatrakoln, K. Valentin, A. Vardi, F.P. Wilkerson, and D.S. Rokhsar. The genome of the diatom *Thalassiosira pseudonana*: Ecology, evolution, and metabolism. *Science*, **306**(5693):79–86, 2004.

[12] C. Bowler, A.E. Allen, J.H. Badger, J. Grimwood, K. Jabbari, A. Kuo, U. Maheswari, C. Martens, F. Maumus, R.P. Otillar, E. Rayko, A. Salamov, K. Vandepoele, B. Beszteri, A. Gruber, M. Heijde, M. Katinka, T. Mock, K. Valentin, F. Verret, J.A. Berges, C. Brownlee, J. Cadoret, A. Chiovitti, C.J. Choi, S. Coesel, A. De Martino, J.C. Detter, C. Durkin, A. Falciatore, J. Fournet, M. Haruta, M.J.J. Huysman, B.D. Jenkins, K. Jiroutova, R.E. Jorgensen, Y. Joubert, A. Kaplan, N. Kröger, P.G. Kroth, J. La Roche, E. Lindquist, M. Lommer, V. Martin–Jézéquel, P.J. Lopez, S. Lucas, M. Mangogna, K. McGinnis, L.K. Medlin, A. Montsant, M. Oudot–Le Secq, C. Napoli, M. Obornik, M.S. Parker, J. Petit, B.M. Porcel, N. Poulsen, M. Robison, L. Rychlewski, T.A. Rynearson, J. Schmutz, H. Shapiro, M. Siaut, M. Stanley, M.R. Sussman, A.R. Taylor, A. Vardi, P. Dassow, W. Vyverman, A. Willis, L.S. Wyrwicz, D.S. Rokhsar, J. Weissenbach, E.V. Armbrust, B.R. Green, Y. Peer, and I.V. Grigoriev. The *phaeodactylum* genome reveals the evolutionary history of diatom genomes. *Nature*, **456**(7219):239–244, 2008.

[13] E. Chacón-Baca, H. Beraldi-Campesi, S.R.S Cevallos-Ferriz, A.H. Knoll, and S. Goublic. 70 ma nonmarine diatoms from Northern Mexico. *Geology*, **30**(3):272–281, 2002.

[14] C. Bowler, A. Vardi, and A.E. Allen. Oceanographic and biogeochemical insights from diatom genomes. *Annual Review of Marine Science*, **2**(1):333–365, 2010.

[15] E.V. Armbrust. The life of diatoms in the world's oceans. *Nature*, **459**(7244):185–192, 2009.

[16] A. Falciatore and C. Bowler. Revealing the molecular secrets of marine diatoms. *Annual Review of Plant Biology*, **53**(1):109–130, 2002.

[17] D.G. Mann and P. Vanormelingen. An inordinate fondness? The number, distributions, and origins of diatom species. *Journal of Eukaryotic Microbiology*, **60**(4):414–420, 2013.

[18] D.M. Nelson, P. Tréguer, M.A. Brzezinski, A. Leynaert, and B. Quéguiner. Production and dissolution of biogenic silica in the ocean: Revised global estimates, comparison with regional data and relationship to biogenic sedimentation. *Global Biogeochemical Cycles*, **9**(3):359–372, 1995.

[19] M. Hildebrand, S.J.L. Lerch, and R.P. Shrestha. Understanding diatom cell wall silicification—moving forward. *Frontiers in Marine Science*, **5**(125):1–19, 2018.

[20] B. Tesson and M. Hildebrand. Dynamics of silica cell wall morphogenesis in the diatom *Cyclotella cryptica*: Substructure formation and the role of microfilaments. *Journal of Structural Biology*, **169**(1):62–74, 2010.

[21] D.H. Robinson and C.W. Sullivan. How do diatoms make silicon biominerals? *Trends in Biochemical Sciences*, **12**(1):151–154, 1987.

[22] B. Tesson and M. Hildebrand. Extensive and intimate association of the cytoskeleton with forming silica in diatoms: Control over patterning on the meso- and micro-scale. *PLoS ONE*, **5**(12):1–13, 2010.

[23] T. Brembu, M.S. Chauton, P. Winge, A.M. Bones, and O. Vadstein. Dynamic responses to silicon in *Thalasiossira pseudonana* - identification, characterisation and classification of signature genes and their corresponding protein motifs. *Scientific Reports*, **7**(1):1–14, 2017.

[24] V.A. Chepurnov, D.G. Mann, K. Sabbe, and W. Vyverman. Experimental studies on sexual reproduction in diatoms. In *International Review of Cytology*. Elsevier. 91–154, 2004.

[25] M. Hildebrand and S.J.L. Lerch. Diatom silica biomineralization: Parallel development of approaches and understanding. *Seminars in Cell & Developmental Biology*, **46**(1):27–35, 2015.

[26] C. Jeffryes, J. Campbell, H. Li, J. Jiao, and G. Rorrer. The potential of diatom nanobiotechnology for applications in solar cells, batteries, and electroluminescent devices. *Energy & Environmental Science*, **4**(10):3930–3941, 2011.

[27] M. Mishra, A.P. Arukha, T. Bashir, D. Yadav, and G.B.K.S. Prasad. All new faces of diatoms: Potential source of nanomaterials and beyond. *Frontiers in Microbiology*, **8**(1239):1–8, 2017.

[28] J. Pickett-Heaps, A.M. Schmid, and L.A. Edgar. The cell biology of diatom valve formation, progress in phycological research. F.E. Round and D.J. Chapman (Eds.). Biopress Ltd., Bristol. 1–168, 1990.

[29] R.M. Black (Ed.). Microfossils. In *The elements of palaeontology*. Cambridge university press. 248, 1987.

[30] D. Losic, R.J. Pillar, T. Dilger, J.G. Mitchell, and N.H. Voelcker. Atomic force microscopy (AFM) characterisation of the porous silica nanostructure of two centric diatoms. *Journal of Porous Materials*, **14**(1):61–69, 2006.

[31] M. Hildebrand. Diatoms, biomineralization processes, and genomics. *Chemical Reviews*, **108**(11):4855–4874, 2008.

[32] M. Hildebrand, S. Kim, D. Shi, K. Scott, and S. Subramaniam. 3D imaging of diatoms with ion-abrasion scanning electron microscopy. *Journal of Structural Biology*, **166**(3):316–328, 2009.

[33] J.E.N. Dolatabadi and M.D.L. Guardia. Applications of diatoms and silica nanotechnology in biosensing, drug and gene delivery, and formation of complex metal nanostructures. *TrAC Trends in Analytical Chemistry*, **30**(9):1538–1548, 2011.

[34] J. Taylor and C. Cocquyt. Diatoms from the Congo and Zambezi basins – methodologies and identification of the genera. Y. Samyn, D.V. Spiegel and J. Degreef (Eds.). In *Abc Taxa. The Series of Manuals Dedicated to Capacity Building in Taxonomy and Collection Management*. Publisher unknown. 1-66, 2016.

[35] M. Hildebrand, E. York, J.I. Kelz, A.K. Davis, L.G. Frigeri, D.P. Allison, and M.J. Doktycz. Nanoscale control of silica morphology and three-dimensional structure during diatom cell wall formation. *Journal of Materials Research*, **21**(10):2689–2698, 2006.

[36] Y.D. Bedoshvili and Y.V. Likhoshway. Cellular mechanisms of diatom valve morphogenesis. J. Seckbach and R. Gordon (Eds.). In *Diatoms: Fundamentals and Applications*. Wiley. 99–114, 2019.

[37] Z. Pan, S.J.L. Lerch, L. Xu, Z. Li, Y. Chuang, J.Y. Howe, S.M. Mahurin, S. Dai, and M. Hildebrand. Electronically transparent graphene replicas of diatoms: A new technique for the investigation of frustule morphology. *Scientific Reports*, **4**(1):1–6, 2014.

[38] J.C. Lewin. Silicon metabolism in diatoms. *The Journal of General Physiology*, **37**(5):589–599, 1954.

[39] P.J. Lopez, J. Desclés, A.E. Allen, and C. Bowler. Prospects in diatom research. *Current Opinion in Biotechnology*, **16**(2):180–186, 2005.

[40] K. Thamatrakoln and M. Hildebrand. Silicon uptake in diatoms revisited: A model for saturable and nonsaturable uptake kinetics and the role of silicon transporters. *Plant Physiology*, **146**(3):1397–1407, 2008.

[41] M.A. Brzezinski. Cell-cycle effects on the kinetics of silicic acid uptake and resource competition among diatoms. *Journal of Plankton Research*, **14**(11):1511–1539, 1992.

[42] G.S. Blank and C.W. Sullivan. Diatom mineralization of silicic acid. *Archives of Microbiology*, **123**(2):157–164, 1979.

[43] N. Poulsen, A. Scheffel, V.C. Sheppard, P.M. Chesley, and N. Kröger. Pentalysine clusters mediate silica targeting of silaffins in *Thalassiosira pseudonana*. *Journal of Biological Chemistry*, **288**(28):20100–20109, 2013.

[44] A. Chiovitti, R.E. Harper, A. Willis, A. Bacic, P. Mulvaney, and R. Wetherbee. Variations in the substituted 3-linked mannans closely associated with the silicified walls of diatoms. *Phycology*, **41**(6):1154–1161, 2005.

[45] N. Kröger and R. Wetherbee. Pleuralins are involved in theca differentiation in the diatom *Cylindrotheca fusiformis*. *Protist*, **151**(3):263–273, 2000.

[46] N. Poulsen and N. Kröger. Silica morphogenesis by alternative processing of silaffins in the diatom *Thalassiosira pseudonana*. *Journal of Biological Chemistry*, **279**(41):42993–42999, 2004.

[47] T. Mock, M.P. Samanta, V. Iverson, C. Berthiaume, M. Robison, K. Holtermann, C. Durkin, S.S. BonDurant, K. Richmond, M. Rodesch, T. Kallas, E.L. Huttlin, F. Cerrina, M.R. Sussman, and E.V. Armbrust. Whole-genome expression profiling of the marine diatom *Thalassiosira pseudonana* identifies genes involved in silicon bioprocesses. *Proceedings of the National Academy of Sciences*, **105**(5):1579–1584, 2008.

[48] L.G. Frigeri, T.R. Radabaugh, P.A. Haynes, and M. Hildebrand. Identification of proteins from a cell wall fraction of the diatom *Thalassiosira pseudonana*. *Molecular & Cellular Proteomics*, **5**(1):182–193, 2005.

[49] S.R. Smith, C. Glé, R.M. Abbriano, J.C. Traller, A. Davis, E. Trentacoste, M. Vernet, A.E. Allen, and M. Hildebrand. Transcript level coordination of carbon pathways during silicon starvation-induced lipid accumulation in the diatom *Thalassiosira pseudonana*. *New Phytologist*, **210**(3):890–904, 2016.

[50] R. Shrestha, B. Tesson, T. Norden-Krichmar, S. Federowicz, M. Hildebrand, and A.E. Allen. Whole transcriptome analysis of the silicon response of the diatom *Thalassiosira pseudonana*. *BMC Genomics*, **13**(499):1–16, 2012.

[51] N. Kroumlger. Polycationic peptides from diatom biosilica that direct silica nanosphere formation. *Science*, **286**(5442):1129–1132, 1999.

[52] A. Scheffel, N. Poulsen, S. Shian, and N. Kröger. Nanopatterned protein microrings from a diatom that direct silica morphogenesis. *Proceedings of the National Academy of Sciences*, **108**(8):3175–3180, 2011.

[53] S. Wenzl, R. Hett, P. Richthammer, and M. Sumper. Silacidins: Highly acidic phosphopeptides from diatom shells assist in silica precipitation in vitro. *Angewandte Chemie International Edition*, **47**(9):1729–1732, 2008.

[54] B. Tesson, S.J.L. Lerch, and M. Hildebrand. Characterization of a new protein family associated with the silica deposition vesicle membrane enables genetic manipulation of diatom silica. *Scientific Reports*, **7**(1):1–13, 2017.

[55] N. Kröger, C. Bergsdorf, and M. Sumper. Frustulins: Domain conservation in a protein family associated with diatom cell walls. *European Journal of Biochemistry*, **239**(2):259–264, 1996.

[56] M. Hildebrand, G. Holton, D.C. Joy, M.J. Doktycz, and D.P. Allison. Diverse and conserved nano- and mesoscale structures of diatom silica revealed by atomic force microscopy. *Journal of Microscopy*, **235**(2):172–187, 2009.

[57] M. Hildebrand, L.G. Frigeri, and A.K. Davis. Synchronized growth of *Thalassoiosira pseudonana* Bacillariophyceae. Provides novel insights into cell wall synthesis. Processes in relation to the cell cycle. *Journal of Phycology*, **43**(4):730–740, 2007.

[58] M.L. Chiappino and B.E. Volcani. Studies on the biochemistry and fine structure of silicia shell formation in diatoms VII. Sequential cell wall development in the pennate *Navicula pelliculosa*. *Protoplasma*, **93**(2):205–221, 1977.

[59] L. Margulis and M.J. Chapman (Eds.). Kingdom protoctista. In *Kingdoms and Domains*. Elsevier. 117–230, 2009.

[60] D.G. Mann. Patterns of sexual reproduction in diatoms. Technical report. **269**(1):11–20, 1993.

[61] M. Hildebrand, M.J. Doktycz, and D.P. Allison. Application of AFM in understanding biomineral formation in diatoms. *Pflügers Archiv - European Journal of Physiology*, **456**(1):127–137, 2007.

[62] N. Almqvist, Y. Delamo, B.L. Smith, N.H. Thomson, A. Bartholdson, R. Lal, M. Brzezinski, and P.K. Hansma. Micromechanical and structural properties of a pennate diatom investigated by atomic force microscopy. *Journal of Microscopy*, **202**(3):518–532, 2001.

[63] S. Hazelaar, H.J. Van Der Strate, W.W.C. Gieskes, and E.G. Vrieling. Monitoring rapid valve formation in the pennate diatom *Navicula Salinarum*. Bacillariophyceae. *Phycology*, **41**(2):354–358, 2005.

[64] M. Vartanian, J. Desclés, M. Quinet, S. Douady, and P. J. Lopez. Plasticity and robustness of pattern formation in the model diatom *Phaeodactylum tricornutum*. *New Phytologist*, **182**(2):429–442, 2009.

[65] M.S. Aw, S. Simovic, Y. Yu, J. Addai-Mensah, and D. Losic. Porous silica microshells from diatoms as biocarrier for drug delivery applications. *Powder Technology*, **223**(1):52–58, 2012.

[66] I. Rea and L.D. Stefano. Recent advances on diatom-based biosensors. *Sensors*, **19**(23):1–8, 2019.

[67] I. Rea, N.M. Martucci, L.D. Stefano, I. Ruggiero, M. Terracciano, P. Dardano, N. Migliaccio, P. Arcari, R. Taté, I. Rendina, and A. Lamberti. Diatomite biosilica nanocarriers for siRNA transport inside cancer cells. *Biochimica et Biophysica Acta (BBA) - General Subjects*, **1840**(12):3393–3403, 2014.

[68] N. Kröger, N. C. Dubey, and E. Kumari. Chapter 6. Immobilization of proteins on diatom biosilica. D. Losic (Ed.). In *Diatom Nanotechnology*. Royal Society of Chemistry. 126–149, 2017.

[69] S. Maher, T. Kumeria, M.S. Aw, and D. Losic. Diatom silica for biomedical applications: Recent progress and advances. *Advanced Healthcare Materials*, **7**(19):1–19, 2018.

[70] E. De Tommasi, J. Gielis, and A. Rogato. Diatom frustule morphogenesis and function: A multidisciplinary survey. *Marine Genomics*, **35**(1):1–18, 2017.

[71] T. Kumeria, M. Bariana, T. Altalhi, M. Kurkuri, C.T. Gibson, W. Yang, and D. Losic. Graphene oxide decorated diatom silica particles as new nano-hybrids: Towards smart natural drug microcarriers. *Journal of Materials Chemistry B*, **1**(45):6302–6311, 2013.

[72] H. Zhang, M. Shahbazi, E.M. Mäkilä, T.H. Da Silva, R.L. Reis, J.J. Salonen, J.T. Hirvonen, and H.A. Santos. Diatom silica microparticles for sustained release and permeation enhancement following oral delivery of prednisone and mesalamine. *Biomaterials*, **34**(36):9210–9219, 2013.

[73] I. Ruggiero, M. Terracciano, N.M. Martucci, L.D. Stefano, N. Migliaccio, R. Tatè, I. Rendina, P. Arcari, A. Lamberti, and I. Rea. Diatomite silica nanoparticles for drug delivery. *Nanoscale Research Letters*, **9**(1):1–7, 2014.

[74] D. Losic, Y. Yu, M.S. Aw, S. Simovic, B. Thierry, and J. Addai-Mensah. Surface functionalisation of diatoms with dopamine modified iron-oxide nanoparticles: Toward magnetically guided drug microcarriers with biologically derived morphologies. *Chemical Communications*, **46**(34):6323–6325, 2010.

[75] V. Onesto, M. Villani, M.L. Coluccio, R. Majewska, A. Alabastri, E. Battista, A. Schirato, D. Calestani, N. Coppedé, M. Cesarelli, F. Amato, E. Di Fabrizio, and F. Gentile. Silica diatom shells tailored with au nanoparticles enable sensitive analysis of molecules for biological, safety and environment applications. *Nanoscale Research Letters*, **13**(1):1–9, 2018.

[76] T. Fuhrmann, S. Landwehr, M.E. Rharbi-Kucki, and M. Sumper. Diatoms as living photonic crystals. *Applied Physics B*, **78**(3):257–260, 2004.

[77] J. Parkinson and R. Gordon. Beyond micromachining: The potential of diatoms. *Trends in Biotechnology*, **17**(5):190–196, 1999.

[78] A.N. Norberg, N.P. Wagner, H. Kaland, F. Vullum-Bruer, and A.M. Svensson. Silica from diatom frustules as anode material for Li-ion batteries. *RSC Advances*, **9**(70):41228–41239, 2019.

[79] D. Losic, G. Rosengarten, J.G. Mitchell, and N.H. Voelcker. Pore architecture of diatom frustules: Potential nanostructured membranes for molecular and particle separations. *Journal of Nanoscience and Nanotechnology*, **6**(4):982–989, 2006.

[80] Z. Bao, M.R. Weatherspoon, S. Shian, Y. Ce, P.D. Graham, S.M. Allan, G. Ahmad, M.B. Dickerson, B.C. Church, Z. Kang, H.W. Abernathy III, C.J. Summers, M. Liu, and K.H. Sandhage. Chemical reduction of three-dimensional silica micro-assemblies into microporous silicon replicas. *Nature*, **446**(7132):172–175, 2007.

[81] Y. Wang, D. Zhang, J. Pan, and J. Cai. Key factors influencing the optical detection of biomolecules by their evaporative assembly on diatom frustules. *Journal of Materials Science*, **47**(17):6315–6325, 2012.

[82] L.D. Stefano, L. Rotiroti, M.D. Stefano, A. Lamberti, S. Lettieri, A. Setaro, and P. Maddalena. Marine diatoms as optical biosensors. *Biosensors and Bioelectronics*, **24**(6):1580–1584, 2009.

[83] M. Terracciano, L.D. Stefano, and I. Rea. Diatoms green nanotechnology for biosilica-based drug delivery systems. *Pharmaceutics*, **10**(4):1–15, 2018.

[84] S. Leonardo, B. Prieto-Simón, and M. Campàs. Past, present and future of diatoms in biosensing. *TrAC Trends in Analytical Chemistry*, **79**(1):276–285, 2016.

[85] Y. Artioli. Adsorption. In *Encyclopedia of Ecology*. Elsevier. 60–65, 2008.

[86] N.R. Haase, S. Shian, K.H. Sandhage, and N. Kröger. Biocatalytic nanoscale coatings through biomimetic layer-by-layer mineralization. *Advanced Functional Materials*, **21**(22):4243–4251, 2011.

[87] N. Poulsen, C. Berne, J. Spain, and N. Kröger. Silica immobilization of an enzyme through genetic engineering of the diatom *Thalassiosira pseudonana*. *Angewandte Chemie International Edition*, **46**(11):1843–1846, 2007.

[88] V.C. Sheppard, A. Scheffel, N. Poulsen, and N. Kröger. Live diatom silica immobilization of multimeric and redox-active enzymes. *Applied and Environmental Microbiology*, **78**(1):211–218, 2011.

[89] N.R. Ford, K.A. Hecht, D. Hu, G. Orr, Y. Xiong, T.C. Squier, G.L. Rorrer, and G. Roesijadi. Antigen binding and site-directed labeling of biosilica-immobilized fusion proteins expressed in diatoms. *ACS Synthetic Biology*, **5**(3):193–199, 2016.

[90] I. Gill and A. Ballesteros. Bioencapsulation within synthetic polymers (Part 1): Sol–gel encapsulated biologicals. *Trends in Biotechnology*, **18**(7):282–296, 2000.

[91] E. Kumari, S. Görlich, N. Poulsen, and N. Kröger. Genetically programmed regioselective immobilization of enzymes in biosilica microparticles. *Advanced Functional Materials*, **30**(25):1–13, 2020.

[92] A. Falciatore, M. Jaubert, J. Bouly, B. Bailleul, and T. Mock. Diatom molecular research comes of age: Model species for studying phytoplankton biology and diversity. *The Plant Cell*, **32**(3):547–572, 2019.

[93] S. Parveen, R. Misra, and S.K. Sahoo. Nanoparticles: A boon to drug delivery, therapeutics, diagnostics and imaging. *Nanomedicine: Nanotechnology, Biology and Medicine*, **8**(2):147–166, 2012.

[94] M.S Aw, S. Simovic, J. Addai-Mensah, and D. Losic. Silica microcapsules from diatoms as new carrier for delivery of therapeutics. *Nanomedicine*, **6**(7):1159–1173, 2011.

[95] R.B. Vasani, D. Losic, A. Cavallaro, and N.H. Voelcker. Fabrication of stimulus-responsive diatom biosilica microcapsules for antibiotic drug delivery. *Journal of Materials Chemistry B*, **3**(21):4325–4329, 2015.

[96] M.S. Aw, M. Bariana, Y. Yu, J. Addai-Mensah, and D. Losic. Surface-functionalized diatom microcapsules for drug delivery of water-insoluble drugs. *Journal of Biomaterials Applications*, **28**(2):163–174, 2012.

[97] E. Blanco, T. Sangai, A. Hsiao, S. Ferrati, L. Bai, X. Liu, F. Meric-Bernstam, and M. Ferrari. Multistage delivery of chemotherapeutic nanoparticles for breast cancer treatment. *Cancer Letters*, **334**(2):245–252, 2013.

[98] B. Delalat, V.C. Sheppard, S.R. Ghaemi, S. Rao, C.A. Prestidge, G. McPhee, M. Rogers, J.F. Donoghue, V. Pillay, T.G. Johns, N. Kröger, and N.H. Voelcker. Targeted drug delivery using genetically engineered diatom biosilica. *Nature Communications*, **6**(1):1–11, 2015.

[99] W. Yang, P.J. Lopez, and G. Rosengarten. Diatoms: Self assembled silicananostructures, and templates for bio/chemical sensors and biomimetic membranes. *The Analyst*, **136**(1):42–53, 2011.

[100] D. Medarevic, D. Losic, and S. Ibric. Diatoms - nature materials with great potential for bioapplications. *Chemical Industry*, **70**(6):613–627, 2016.

[101] H.E. Townley, A.R. Parker, and H. White-Cooper. Exploitation of diatom frustules for nanotechnology: Tethering active biomolecules. *Advanced Functional Materials*, **18**(2):369–374, 2008.

[102] A. Li, J. Cai, J. Pan, Y. Wang, Y. Yue, and D. Zhang. Multi-layer hierarchical array fabricated with diatom frustules for highly sensitive bio-detection applications. *Journal of Micromechanics and Microengineering*, **24**(2):1–9, 2014.

[103] K. Lin, V. Kunduru, M. Bothara, K. Rege, S. Prasad, and B.L. Ramakrishna. Biogenic nanoporous silica-based sensor for enhanced electrochemical detection of cardiovascular biomarkers proteins. *Biosensors and Bioelectronics*, **25**(10):2336–2342, 2010.

[104] K. Albert, X. Huang, and H. Hsu. Bio-templated silica composites for next-generation biomedical applications. *Advances in Colloid and Interface Science*, **249**(1):272–289, 2017.

[105] A. Kamińska, M. Sprynskyy, K. Winkler, and T. Szymborski. Ultrasensitive SERS immunoassay based on diatom biosilica for detection of interleukins in blood plasma. *Analytical and Bioanalytical Chemistry*, **409**(27):6337–6347, 2017.

[106] J. Yang, L. Zhen, F. Ren, J. Campbell, G.L. Rorrer, and A.X. Wang. Ultra-sensitive immunoassay biosensors using hybrid plasmonic-biosilica nanostructured materials. *Journal of Biophotonics*, **8**(8):659–667, 2014.

[107] X. Kong, Y. Xi, P.L. Duff, X. Chong, E. Li, F. Ren, G.L. Rorrer, and A.X. Wang. Detecting explosive molecules from nanoliter solution: A new paradigm of SERS sensing on hydrophilic photonic crystal biosilica. *Biosensors and Bioelectronics*, **88**:63–70, 2017.

[108] D.P. Snustad and M.J. Simmons (Eds). Chapter 14. The techniques of molecular genetics. In *Genetics*. Wiley. 366-473, 2012.

[109] E. Snapp. Design and use of fluorescent fusion proteins in cell biology. *Current Protocols in Cell Biology*, **27**(1):1–13, 2005.

[110] N.C. Shaner, G.G. Lambert, A. Chammas, Y. Ni, P.J. Cranfill, M.A. Baird, B.R. Sell, J.R. Allen, R.N. Day, M. Israelsson, M.W. Davidson, and J. Wang. A bright monomeric green fluorescent protein derived from *Branchiostoma lanceolatum*. *Nature Methods*, **10**(5):407–409, 2013.

[111] P.J. Verveer and P.I.H. Bastiaens. FRET analysis of signaling events in cells. R.A. Bradshaw and E.A. Dennis (Eds.). In *Handbook of Cell Signaling*. Elsevier. 305–309, 2003.

[112] B.J. Karas, R.E. Diner, S.C. Lefebvre, J. McQuaid, A.R. Phillips, C.M. Noddings, J.K. Brunson, R.E. Valas, T.J. Deerinck, J. Jablanovic, J.T.F. Gillard, K. Beeri, M.H. Ellisman, J.I. Glass, C.A. Hutchison III, H.O. Smith, J.C. Venter, A.E. Allen, C.L. Dupont, and P.D. Weyman. Designer diatom episomes delivered by bacterial conjugation. *Nature Communications*, **6**(1):1–10, 2015.

[113] R.E. Diner, V.A. Bielinski, C.L. Dupont, A.E. Allen, and P.D. Weyman. Refinement of the diatom episome maintenance sequence and improvement of conjugation-based dna delivery methods. *Frontiers in Bioengineering and Biotechnology*, **4**(8):1–12, 2016.

[114] R.E. Diner, C.M. Noddings, N.C. Lian, A.K. Kang, J.B. McQuaid, J. Jablanovic, J.L. Espinoza, N.A. Nguyen, M.A. Anzelmatti, J. Jansson, V.A. Bielinski, B.J. Karas, C.L. Dupont, A.E. Allen, and Å.D. Weyman. Diatom centromeres suggest a mechanism for nuclear DNA acquisition. *Proceedings of the National Academy of Sciences*, **114**(29):15–24, 2017.

[115] G. Prelich. Gene overexpression: Uses, mechanisms, and interpretation. *Genetics*, **190**(3):841–854, 2012.

[116] H. Chen, S. Venkat, J. Wilson, P. McGuire, A. Chang, Q. Gan, and C. Fan. Genome-wide quantification of the effect of gene overexpression on *Escherichia coli* growth. *Genes*, **9**(8):1–12, 2018.

[117] D. Vaulot, R.J. Olson, and S.W. Chisholm. Light and dark control of the cell cycle in two marine phytoplankton species. *Experimental Cell Research*, **167**(1):38–52, 1986.

[118] W.M. Darley and B.E. Volcani. Role of silicon in diatom metabolism. *Experimental Cell Research*, **58**(2):334–342, 1969.

[119] A. Kotzsch, P. Gröger, D. Pawolski, P.H.H. Bomans, N.A.J.M. Sommerdijk, M. Schlierf, and N. Kröger. Silicanin-1 is a conserved diatom membrane protein involved in silica biomineralization. *BMC Biology*, **15**(1):1–16, 2017.

[120] N. Kröger. Self-assembly of highly phosphorylated silaffins and their function in biosilica morphogenesis. *Science*, **298**(5593):584–586, 2002.

[121] A.M.L. Van De Meene and J.D. Pickett-Heaps. Valve morphogenesis in the centric diatom *Proboscia alatasundstrom*. *Journal of Phycology*, **38**(2):351–363, 2002.

[122] Y. Bedoshvili, K. Gneusheva, M. Popova, A. Morozov, and Y. Likhoshway. Anomalies in the valve morphogenesis of the centric diatom alga *Aulacoseira* islandica caused by microtubule inhibitors. *Biology Open*, **7**(8):1–10, 2018.

[123] G.S. Blank and C.W. Sullivan. Diatom mineralization of silicic acid VI. the effects of microtubule inhibitors on silicic acid metabolism in *navicula saprophila*. *Journal of Phycology*, **19**(1):39–44, 1983.

[124] S.A. Cohn, J. Nash, and J.D. Pickett-Heaps. The effect of drugs on diatom valve morphogenesis. *Protoplasma*, **149**(2):130–143, 1989.

[125] K.V. Kharitonenko, Y.D. Bedoshvili, and Y.V. Likhoshway. Changes in the micro- and nanostructure of siliceous valves in the diatom *Synedra acus* under the effect of colchicine treatment at different stages of the cell cycle. *Journal of Structural Biology*, **190**(1):73–80, 2015.

[126] A.M.L. Van De Meene and J.D. Pickett-Heaps. Valve morphogenesis in the centric diatom *rhizosolenia setigera* (Bacillariophyceae, Centrales) and its taxonomic implications. *European Journal of Phycology*, **39**(1):93–104, 2004.

[127] T. Svitkina. The actin cytoskeleton and actin-based motility. *Cold Spring Harbor Perspectives in Biology*, **10**(1):1–22, 2018.

[128] R. Dominguez and K.C. Holmes. Actin structure and function. *Annual Review of Biophysics*, **40**(1):169–186, 2011.

[129] C. Aumeier, E. Polinski, and D. Menzel. Actin, actin-related proteins and profilin in diatoms: A comparative genomic analysis. *Marine Genomics*, **23**(1):133–142, 2015.

[130] Open University. *A tour of the cell: 4.2 The cytoskeleton*. `https://www.open.edu/openlearn/science-maths-technology/science/tour-the-cell/content-section-4.2`, no date. (Accessed on 06/14/2020).

[131] G.J. Brouhard and L.M. Rice. Microtubule dynamics: An interplay of biochemistry and mechanics. *Nature Reviews Molecular Cell Biology*, **19**(7):451–463, 2018.

[132] M. Schliwa. Action of cytochalasin D on cytoskeletal networks. *The Journal of Cell Biology*, **92**(1):79–91, 1982.

[133] M. Trendowski. Using cytochalasins to improve current chemotherapeutic approaches. *Anti-Cancer Agents in Medicinal Chemistry*, **15**(3):327–335, 2015.

[134] Y.Y. Leung, L.L.Y. Hui, and V.B. Kraus. Colchicine—update on mechanisms of action and therapeutic uses. *Seminars in Arthritis and Rheumatism*, **45**(3):341–350, 2015.

[135] L.C. Morejohn, T.E. Bureau, J. Mol-Bajer, A.S. Bajer, and D.E. Fosket. Oryzalin, a dinitroaniline herbicide, binds to plant tubulin and inhibits microtubule polymerization in vitro. *Planta*, **172**(2):252–264, 1987.

[136] M. Nymark, C. Volpe, M.C.G Hafskjold, H. Kirst, M. Serif, O. Vadstein, A.M. Bones, A. Melis, and P. Winge. Loss of ALBINO3b insertase results in truncated light-harvesting antenna in diatoms. *Plant Physiology*, **181**(3):1257–1276, 2019.

[137] T.A. Strand, R. Lale, K.F. Degnes, M. Lando, and S. Valla. A new and improved host-independent plasmid system for RK2-based conjugal transfer. *PLoS ONE*, **9**(3):1–6, 2014.

[138] J. Romann, M.S. Chauton, S.M. Hanetho, M. Vebner, M. Heldal, C. Thaulow, O. Vadstein, G. Tranell, and M. Einarsrud. Diatom frustules as a biomaterial: Effects of chemical treatment on organic material removal and mechanical properties in cleaned frustules from two *Coscinodiscus* species. *Journal of Porous Materials*, **23**(4):905–910, 2016.

[139] K. Thamatrakoln and M. Hildebrand. Analysis of *Thalassiosira pseudonana* silicon transporters indicates distinct regulatory levels and transport activity through the cell cycle. *Eukaryotic Cell*, **6**(2):271–279, 2006.

[140] I. Lobo. Environmental influences on gene expression — learn science at scitable. `https://www.nature.com/scitable/topicpage/environmental-influences-on-gene-expression-536/`, 2008. (Accessed on 06/19/2020).

[141] J.A. Law and S.E. Jacobsen. Establishing, maintaining and modifying DNA methylation patterns in plants and animals. *Nature Reviews Genetics*, **11**(3):204–220, 2010.

[142] E.E. Jarvis, T.G. Dunahay, and L.M. Brown. DNA nucleoside composition and methylation in several species of microalgae. *Phycology*, **28**(3):356–362, 1992.

[143] F. Maumus, P. Rabinowicz, C. Bowler, and M. Rivarola. Stemming epigenetics in marine Stramenopiles. *Current Genomics*, **12**(5):357–370, 2011.

[144] D.P. Snustad and M.J. Simmons (Eds). Chapter 19. Regulation of gene expression in eukaryotes. Wiley. 531-555.

[145] S. Ramchandani, S.K. Bhattacharya, N. Cervoni, and M. Szyf. DNA methylation is a reversible biological signal. *Proceedings of the National Academy of Sciences*, **96**(11):6107–6112, 1999.

[146] V. Mladenova, E. Mladenov, and G. Russev. Organization of plasmid DNA into nucleosome-like structures after transfection in eukaryotic cells. *Biotechnology & Biotechnological Equipment*, **23**(1):1044–1047, 2009.

[147] T. Vaissiere, C. Sawan, and Z. Herceg. Epigenetic interplay between histone modifications and DNA methylation in gene silencing. *Mutation Research/Reviews in Mutation Research*, **659**(1):40–48, 2008.

[148] V. Sheppard, N. Poulsen, and N. Kröger. Characterization of an endoplasmic reticulum-associated silaffin kinase from the diatom *Thalassiosira pseudonana*. *Journal of Biological Chemistry*, **285**(2):1166–1176, 2009.

[149] Y. Fujiki, A.L. Hubbard, S. Fowler, and P.B Lazarow. Isolation of intracellular membranes by means of sodium carbonate treatment: Application to endoplasmic reticulum. *The Journal of Cell Biology*, **93**(1):97–102, 1982.

[150] R.P. Shrestha and M. Hildebrand. Evidence for a regulatory role of diatom silicon transporters in cellular silicon responses. *Eukaryotic Cell*, **14**(1):29–40, 2014.

[151] A. Hopes, V. Nekrasov, S. Kamoun, and T. Mock. Editing of the urease gene by CRISPR-cas in the diatom *Thalassiosira pseudonana*. *Plant Methods*, **12**(1):1–12, 2016.

[152] A.A. Trofimov, A.A. Pawlicki, N. Borodinov, S. Mandal, T.J. Mathews, M. Hildebrand, M.A. Ziatdinov, K.A. Hausladen, P.K. Urbanowicz, C.A. Steed, A.V. Ievlev, A. Belianinov, J.K. Michener, R. Vasudevan, and O.S. Ovchinnikova. Deep data analytics for genetic engineering of diatoms linking genotype to phenotype via machine learning. *npj Computational Materials*, **5**(1), 2019.

[153] R.R.L. Guillard (Ed.). Culture of phytoplankton for feeding marine invertebrates. In *Culture of Marine Invertebrate Animals*. Plenum Press. 26-60, 1975.

[154] Bio-Rad. *Precision Plus Protein Dual Color Standards*. `https://www.bio-rad.com/en-no/sku/1610374-precision-plus-protein-dual-color-standards-500-ul?ID=1610374`, no date. (Accessed on 05/27/2020).

[155] Fisher Scientific. *Thermo Scientific GeneRuler 1kb Plus DNA Ladder*. https://www.fishersci.se/shop/products/fermentas-generuler-1kb-plus-dna-ladder/11581625, no date. (Accessed on 12/05/2019).

Appendix

A Recipes for Culture Media and Agar Plates

The following recipes are similar to those used during the specialization project conducted in 2019. Hence, they have been reviewed and re-used [1]. All medium has been stored at 4°C.

A.1 f/2 Medium

Table A.1 shows the recipe for the f/2 medium. This growth medium is developed for growing coastal marine algae and is especially suitable for diatoms. Filtered seawater, FSW, (0.2 μm filter, 1000 mL) was autoclaved (120°C, 20 min) and cooled down until reaching a temperature less than 55°C. Nutritional salts, vitamins, and trace metals were added after filtration (0.2 μ). Antibiotics were added when needed. Prior to the making of f/2 medium, stock solutions of vitamins and trace metals were made. Recipes are given in Table A.2 and Table A.3, respectively. All concentrations in the tables are the final concentrations in an f/2-medium, together with a suggested stock solution. Si-free f/2 medium was made with the same recipe, and the only difference is that $Na_2SiO_3 \cdot 9H_2O$ was excluded. To simplify the preparation of Si-free f/2 medium, $Na_2SiO_3 \cdot 9H_2O$ was excluded from the stock solution of trace metals [153].

Table A.1: f/2 medium recipe for growing coastal marine algae. FSW is added to obtain a total volume of 1 L.

Components	Concentration [M]	Stock solution [g/L]	Volume [mL]
$NaNO_3$	$8.82 \cdot 10^{-4}$	75	1
NaH_2PO_4	$3.62 \cdot 10^{-5}$	5	1
$Na_2SiO_3 \cdot 9\ H_2O$	$1.06 \cdot 10^{-4}$	45	1
Vitamins	*	*	1
Trace metals	*	*	1

Table A.2: Vitamins (vit) needed for f/2 medium with suggested stock solutions and the necessary amount for the preferrable final concentration.

Vitamins	Concentration [M]	Stock solution [g/L]	Amount
Thiamine HCl (vit. B_1)	$2.96 \cdot 10^{-7}$	-	200 mg
Biotin (vit. H)	$2.05 \cdot 10^{-9}$	1	1 mL
Cyanocobalamin (vit. B_{12})	$3.69 \cdot 10^{-10}$	1	1 mL

Table A.3: Trace elements necessary for f/2 medium with suggested stock solutions and the necessary amount for the preferrable final concentration.

Trace metals	Concentration [M]	Stock solution [g/L]	Amount [g]
$FeCl_3 \cdot 6H_2O$	$1.17 \cdot 10^{-5}$	-	3.15
$Na_2EDTA \cdot 2H_2O$	$1.17 \cdot 10^{-5}$	-	4.36
$CuSO_4 \cdot 5H_2O$	$3.93 \cdot 10^{-8}$	9.8	1
$Na_2MoO_4 \cdot 2H_2O$	$2.60 \cdot 10^{-8}$	6.3	1
$ZnSO_4 \cdot 7H_2O$	$7.65 \cdot 10^{-8}$	22.0	1
$CoCl_2 \cdot 6H_2O$	$4.20 \cdot 10^{-8}$	10.0	1
$MnCl_2 \cdot 4H_2O$	$9.20 \cdot 10^{-7}$	180.0	1

A.2 L1 Medium

The necessary components and the respective amounts needed to make 1 L of the L1 medium are given in Table A.4. Pre-autoclaved (120°C, 20 min) FSW (950 mL) was cooled down prior to the addition of the necessary components.

Table A.4: Components and the specific amount needed for 1 L of the L1 medium. FSW is added to a total amount of 1 L.

Components	Concentration [g/L]	Amount [g]
$Na_2EDTA \cdot 2H_2O$	4.36	4.36 g
$FeCl_3 \cdot 6H_2O$	3.15	3.15 g
$MnCl_2 \cdot H_2O$	178.1	1 mL
$ZnSO_4 \cdot 7H_2O$	23.0	1 mL
$CoCl_2 \cdot 6H_2O$	11.9	1 mL
$CuSO_4 \cdot 5H_2O$	2.50	1 mL
$Na_2MoO_4 \cdot 2H_2O$	19.9	1 mL
$NiSO_4 \cdot 6H_2O$	2.63	1 mL
H_2SeO_3	1.29	1 mL
Na_3VO_4	1.84	1 mL
K_2CrO_4	1.94	1 mL

A.3 L1 Agar Plates

A diluted version of the L1 medium was used for L1 agar plates (94% diluted L1, 5% LB medium, 1% agar). This was made as explained in Appendix A.2, except that 490 mL of FSW was replaced with deionized water, and agar (10 g) was added before autoclavation. LB medium was made as explained in Appendix A.4 and added to the L1 medium such that a 5% concentration was obtained. Necessary antibiotics were added before the solution was poured into Petri dishes.

A.4 LB Medium and LB Agar Plates

LB medium and LB agar were used for bacterial growth. Table A.5 shows the components needed for the making of both types, as the only difference is whether or not bactoagar are added before sterilization. Deionized water (1000 mL) and the necessary amount of each component was added to a flask and autoclaved (120°C, 20 min). When a selection marker was needed, antibiotic was added when the temperature was below 55°C to avoid degrading. LB agar plates were made by pouring agar solution into Petri dishes.

Table A.5: Components and the specific amount needed for 1 L of LB medium and LB agar plates. Bactoagar are only included when LB agar plates are made.

Components	**Amount [g/L]**
Trypton	10
Yeast extract	5
NaCl	5
(Bactoagar)	15

B Protocols

B.1 SDS-page

An SDS-page gel is composed of a resolving gel and a stacking gel. The components necessary to make a complete gel with the respective volumes are listed in Table B.1.

Table B.1: Components with the respective volumes that are used to make an SDS-page with a resolving gel and a stacking gel.

Components	**Resolving gel [μL]**	**Stacking gel [μL]**
MQ	3.15	2.15
Acrylamid, 40%	2.25	352
Tris, 1.5M	1.95	-
Tris, 0.5M	-	0.91
SDS, 10%	75	35
APS, 10%	75	35
TEMED	7.5	7.5

Resolving gel and stacking gel was made separately, starting with the stacking gel. All components were mixed. The addition of ammonium persulfate (APS) and tetramethylethylenediamine (TEMED) resulted in a fast polymerization and was therefore added last. The solution was quickly pipetted into the gel chamber (XCell SureLock) until reaching the filler line. Isopropanol was added to prevent air bubbles and flatten out the gel. When the gel was fully polymerized, isopropanol was poured out of the gel chamber. Resolving gel was made, with the same order of addition as the former gel, and the solution was quickly pipetted into the gel chamber. Gel comb was added and kept in the gel until it was fully polymerized. 1x SDS running buffer was prepared with MOPS SDS Running Buffer (Novex) by diluting it with MQ (ratio 1:20). This solution was used to rinse the gel three times after the gel comb was removed before the chamber was filled with the same solution.

A combination of pellet, supernatant, and protein extract of the different protein samples was used for analysis. Hence, protein extracts from transformants, TpWt, and *E. coli* were spun down (6500 g, 100 μL, 10 min) before sample preparation. See Table B.2 for detailed information of each sample.

Table B.2: Information on each sample run on SDS-page. Protein samples from wild type (TpWt) and transformants (mNG-Tp23191) of *T. pseudonana*, in addition to *E. coli* with pNCS-mNG were used.

Samples	Protein samples	Volume [μL]	MQ [μL]
1. *E. coli* with pNCS-mNG	Protein extract	5	10
2. *E. coli* with pNCS-mNG	Pellet	-	15
3. TpWt	Protein extract	15	-
4. mNG-Tp23191-4	Protein extract	15	-
5. mNG-Tp23191-11	Protein extract	15	-
6. mNG-Tp23191-4	Supernatant	15	-
7. mNG-Tp23191-4	Pellet	-	15

Samples were incubated with protein loading dye (NuPAGE by Invitrogen, 5 μL) and incubated (30 min, 50°C). Furthermore, samples (20 μg) and protein ladder were loaded in separate wells onto the pre-made 12% SDS gel. SDS-page lasted for 90 min (100 V, 40 mA).

B.2 Towbin Buffer

Towbin buffer (1L) was made with the components and the respective volumes described in Table B.3. The volume was adjusted to 1 L by the addition of MQ.

Table B.3: Recipe for Towbin buffer. The volume was adjusted to 1 L by further addition of MQ.

Chemicals	Amounts
Tris, 25 mM	3.03 g
Glycine, 20%	14.4 g
Methanol, pH 8.3	200 mL
MQ	500 mL

B.3 PVDF Membrane

PVDF membrane by Invitrogen (0.45 μm pore size) was used for Western Blot. The membrane was equilibrated in methanol (100%, 30 sec), washed in MQ (2 min), and kept in Towbin buffer (10 min) with continuously shaking.

B.4 1x Bind Solution

1x iBind Flex Solution Kit by Invitrogen was used to make a 1x Bind Solution. The following recipe is given in Table B.4.

Table B.4: The reagents and the specific volume necessary to make 1x Bind Solution.

Components	Volume [mL]
iBind 5x Buffer	6
iBind 100x Additive	0.3
MQ	23.7
Total volume:	30

B.5 Heat-shock Transformation

Competent *E. coli* DH10B cells from -80°C were thawed on ice and gently mixed with a plasmid (324.3 ng/uL, 0.1 μL). The mixture was incubated on ice (30 min), followed by heat-shock (42°C, 45 sec). After incubation on ice (2 min), SOC-media (950 μL) was added to the tube. The tube was incubated (37°C, 60 min) with coherent shaking (250 rpm) using incubator Multitron by INFORS. 100μL was spread on prewarmed LB-agar plates (50 μg/mL kan, 10 μg/mL gen) and incubated overnight at 37°C.

B.6 DNA Isolation

DNeasy Plant Pro Kit by Qiagen was used for DNA isolation of TpWt and transformants. Solution CD1 (500 μL) and a pre-cooled bead of stainless-steel were added to the sample before it was run twice in MM400 Mixer Mill by Retsch. The sample was placed in a pre-cooled adapter set for the first run and transferred to a pre-warmed adapter set before the second run. Program settings are given in Table B.5.

Table B.5: Program settings used on Retsch to break down cells into smaller fractions. The samples were run twice with different temperatures on the adapter set.

Run	Adapter set [°C]	Frequency [Hz]	Time [min]
1	-80	24	2
2	20	24	2

A further stepwise procedure is given below:

1. The sample was centrifuged (12 000 g, 2 min).
2. The supernatant was transferred to a clean Eppendorf tube (1.5 mL), and solution CDS2 (250 μL) was added before the sample was vortexed (5 sec).
3. The sample was centrifuged (12 000 g, 1 min), and the supernatant was transferred to a clean Eppendorf tube.
4. Buffer APP (500 μL) was added, and the sample was vortexed (5 sec).
5. The lysate was transferred to an MB Spin Column (600 μL x 2), followed by centrifugation (12 000 g, 1 min x 2) and discard of flow-through.
6. Buffer AW1 (650 μL) was added to the MB Spin Column, followed by centrifugation (12 000 g, 1 min). Flow-through was discarded, and the tube was centrifuged (16 000 g, 2 min).
7. The MB Spin Column was transferred to a new Eppendorf tube, and Buffer EB (100 μL) was added to the center of the filter membrane.
8. The sample was centrifuged (12 000 g, 1 min), the MB Spin Column was discarded, and the flow-through was kept for further analysis.

B.7 Sample Preparation before PCR

Phusion High-Fidelity DNA Polymerase kit by ThermoFisher Scientific was used for sample preparation before PCR. The recipe is given in Table B.6. In order to prevent degradation caused by DNA polymerase, this component was added in the end.

Table B.6: ThermoFisher Scientific recommends the given recipe for a PCR.

Components	Volume [μL]	Final concentration
5 x HF buffer	10	1x
dNTP	1	10 mM each
DMSO	1	(3%)
MQ	30	-
Forward primer	2.5	0.5 μM
Reverse primer	2.5	0.5 μM
Template DNA	5	$<$250 ng
DNA polymerase	0.5	0.02 U/µL

B.8 Constructs for PCR

Annealing temperature and elongation time were adjusted to the primers and the size of the DNA fragments. These settings, together with information about the constructs, are given in Table B.7. Nucleotide sequences for the different primers are listed in Table B.8.

Table B.7: All fragments amplified with PCR are given below. The length of each fragment and the primers are included in addition to the specific settings used for PCR.

Number	Template	Length [bp]	Primer	Annealing temperature [°C]	Elongation time [sec]
1	NrsR	211	NouF NouR	64	15
2	Parts of mNeonGreen-Tp23191	1653	His3-seqF M13Rev	60	30
3	mNeonGreen-Tp23191 protein	3769	His3-seqF mNeonR	54	60
4	Parts of Tp23191	1726 and 993	F1 R1	54	35
5	The whole Tp23191	2299 and 1566	F1 R2	54	35

Table B.8: Nucleotide sequences for the different primers used for amplification of DNA constructs.

Primer	Nucletide sequence
NrsF	5'-TCCTTCACCACCGACACC
NrsR	3'-ACGAGACGACCACGAAGC
His3-SeqF	5'-TGTTCCCTCCACCAAAG
M13REV	3'-CAGGAAACAGCTATGAC
mNeonSeqR	3'-TGGACTTCAGGTTTAACTCC
F1	5'-TTGATCAGCAGTGACCTCAACA
R1	3'-TGATGTAGTTCTCGGCGTAAGT
R2	3'-CAACACAGGGAGGTCAAACTCT

B.9 Agarose Gel Electrophoresis

Agarose gel (1.2%) was made by mixing agarose (4.8 g) and 1x stock solution (400 mL) of Tris-acetate-EDTA (TAE) buffer. TAE buffer contains a mixture of Tris base, acetic acid, and ethylenediaminetetraacetic acid (EDTA). The content of a 50x TAE buffer is given in Table B.9. A 1x stock solution was made by mixing 50x stock solution TAE buffer (20 mL) with MQ (980 mL). The agarose gel was heated until reaching the boiling point and stored at 60°C before use.

Table B.9: The following components and the corresponding amount necessary to make a 50x stock solution of TAE buffer.

Components	Consentration[mM]	Amount
Tris-base	2	242 g/L
Acetate	1	57.1 mL/L
Sodium EDTA	50	100 mL/L

Prior to gel electrophoresis, agarose gel (1.2%) was added to a gel chamber and dried before the gel was covered with buffer (1xTAE). DNA ladder (5 μL) was added to the first well, and a mixture of loading dye and sample (1:5 ratio) was added in separate wells. The agarose gel electrophoresis was conducted (100 V, 20 W) within a time region of 1-2 h.

B.10 Sample Preparation before Sanger Sequencing

QIAquick gel extraction kit by Qiagen was used for DNA extraction from an agarose gel after gel electrophoresis. The stepwise procedure is given below:

1. A DNA fragment was cut from the agarose gel with a sharp scalpel, weighted, and placed in an Eppendorf tube.
2. Buffer QG and gel (3:1 ratio) were incubated (50°C, 10 min) with constant shaking to dissolve the gel.
3. Isopropanol (1 gel volume) was added to the sample, mixed and transferred to a QIAquick spin column. Samples were centrifuged (19 000 g, 1 min), and flow-through was discarded. For large sample volumes, they were spun several times until all volume had run through the column.

4. Buffer QG (500 μL) was added, the sample was centrifuged (19 000 g, 1 min), and flow-through was discarded.
5. For washing, Buffer PE (750 μL) was added, the sample was centrifuged (19 000 g, 1 min), and flow-through was discarded.
6. To elute DNA, the QIAquick column was placed into a clean Eppendorf tube, and Buffer EB (50 μL) was added to the center of the membrane. The sample was centrifuged (19 000 g, 1 min), and the flow-through was kept for further analysis.

An Eppendorf tube of the modified plasmid, specific primers, and MQ were sent to Eurofins Genomics for Sanger sequencing, see Table B.10 for the specific relationship considering the components.

Table B.10: DNA fragment and the specific primers were added to an Eppendorf tube and sent to Eurofins Genomics for Sanger sequencing.

Component	**Amount [μL]**
DNA fragment	5
Forward primer	2.5
Reverse primer	2.5

B.11 Frustule Cleaning

A modified version of the soft cleaning protocol developed by Romann et al. was used for frustule cleaning [138]. The stepwise procedure is given below:

1. Cells were pelleted by centrifugation (3242 g, 10 min).
2. Pelleted diatoms were washed with MQ and centrifuged (3242 g, 10 min x 3) before incubated overnight at 60 °C.
3. The sample was dissolved in SDS/EDTA solution (4 mL, 50 g $L^{-}1$ in 100 mM Titriplex III) at pH 5, vortexed (1 min) and incubated in room temperature for 20 min and centrifuged (3242 g, 10 min). This step was repeated six times.
4. The sample was washed with MQ and centrifuged (3242 g, 10 min) before it was extracted in ethanol (1 mL, 96%) and stored at 4 °C.
5. Centrifugation (3242 g, 10 min) followed by a new round of step 3-5 was performed to remove more organic material from the frustules.

B.12 Sample Preparation before SEM

The stepwise procedure for sample preparation before SEM are given below:

- A sample with *T. pseudonana* frustules diluted in ethanol (70%) was centrifuged. The supernatant (700 μL) was removed, and the sample was resuspended by vortexing.
- Double-sided carbon tape was attached to the SEM pin (Chemi-Teknik). Dust was removed from a silicon wafer (P4, Chemi-Teknik) using a bellows before the silicon wafer was placed on a filter paper (Whatman 50 Hardened, VWR).
- A small cut was made on edge using a diamond pen, and the disc was split in two by applying pressure. Pieces of 10 x 10 mm were broken off and placed on the carbon tape attached to the SEM pin.
- Sample (15 μL) was pipetted on different pieces of the silicon wafer. A lid was placed on top, and the sample was dried for 30 min.
- The lid was removed, and the sample was coated with gold/palladium (15 nm in thickness).

C Interpretation of Results

C.1 Genomic Analysis of *T. pseudonana* Transformants

A map of the plasmid integrated into *T. pseudonana* transformants are given in Figure C.1 together with the primers used for amplification of the five different DNA fragments. The forward and reverse primers used in the same reactions are marked with a similar color.

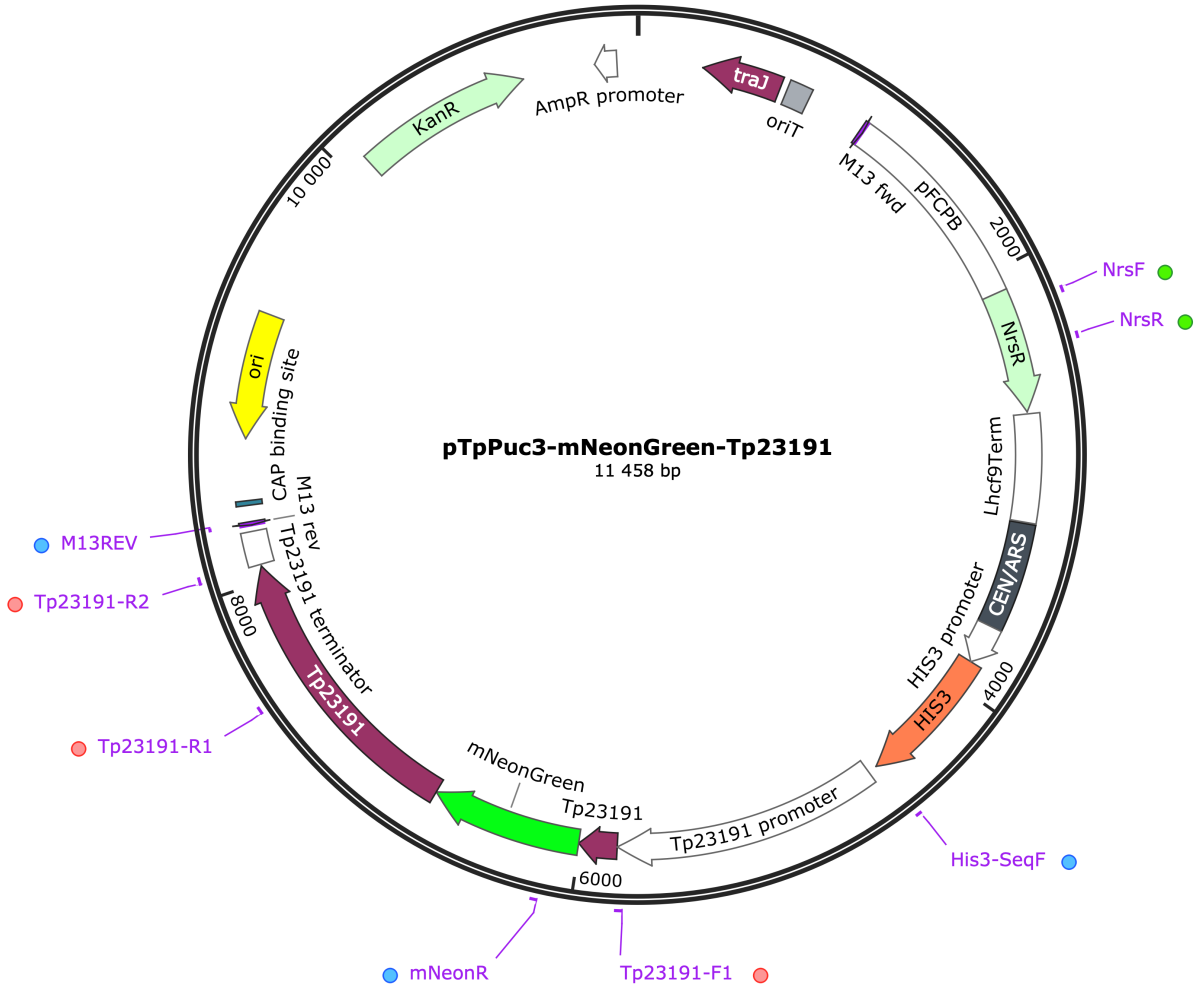

Figure C.1: Plasmid pTpPuc3-mNG-Tp23191 constructed with SnapGene. Primers used for amplification of different DNA fragments are shown in purple, and each pair are denoted with a specific color. Forward primers His3-seqF and F1 are used for amplification of different fragments. Hence, both reverse primers are marked with the same color.

C.2 Protein Ladder for SDS-page

Figure C.2 shows the Precision Plus Protein Dual Color Standards used as a reference when the sizes of proteins were determined after an SDS-page.

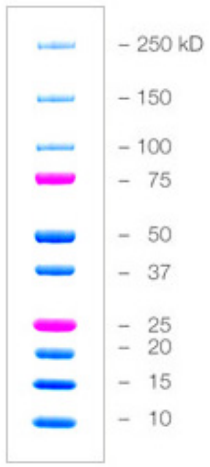

Figure C.2: Precision Plus Protein Dual Color Standard with bands and their specific sizes given in kD. [154].

C.3 DNA Ladder for Gel Electrophoresis

Figure C.3 shows the GeneRuler 1kb Plus DNA Ladder run on agarose gel (1%) for 45 min. Precise sizes of the DNA fragments are stated. The DNA ladder and its sizes were used for the identification of DNA fragments after PCR.

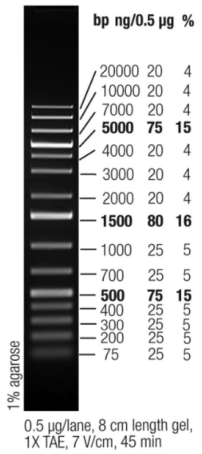

Figure C.3: The bands and their specific sizes are given in bp after GeneRuler 1kb Plus DNA Ladder has run on an agarose gel (1%) for 45 min [155].

D Supplementary Results

D.1 The Third Synchronization Study

The fraction of live cells for all measurements collected during the third synchronization study is given in Table D.1. A sharp temporary reduction in cell density at 3 h was not in coherence with the calculated fraction of live cells. This deviation is colored in red.

Table D.1: The calculated fractions of live cells for all measurements conducted during the third synchronization study. The deviation is colored red.

Time	Fraction of live cells		
[h]	TpWt	mNG-Tp23191-4	mNG-Tp23191-11
0	0,63	0,67	0,67
1	0,60	0,65	0,65
2	0,63	0,68	0,69
3	0,65	0,72	0,72
4	0,61	0,69	0,70
5	0,59	0,70	0,70
6	0,61	0,71	0,71
7	0,60	0,72	0,72
7,5	0,61	0,73	0,73
8	0,60	0,72	0,72
8,5	0,62	0,70	0,73
9	0,62	0,77	0,74

D.2 Cell Cycle Stage Determinations

Height versus area density plot on the fluorescent channel for SybrGreen from measurements with FCM, and graphical distribution of cells in different cell stages calculated with Novo Cyte software, for mNG-Tp23191-11 are given in Figure D.1.A and B, respectively.

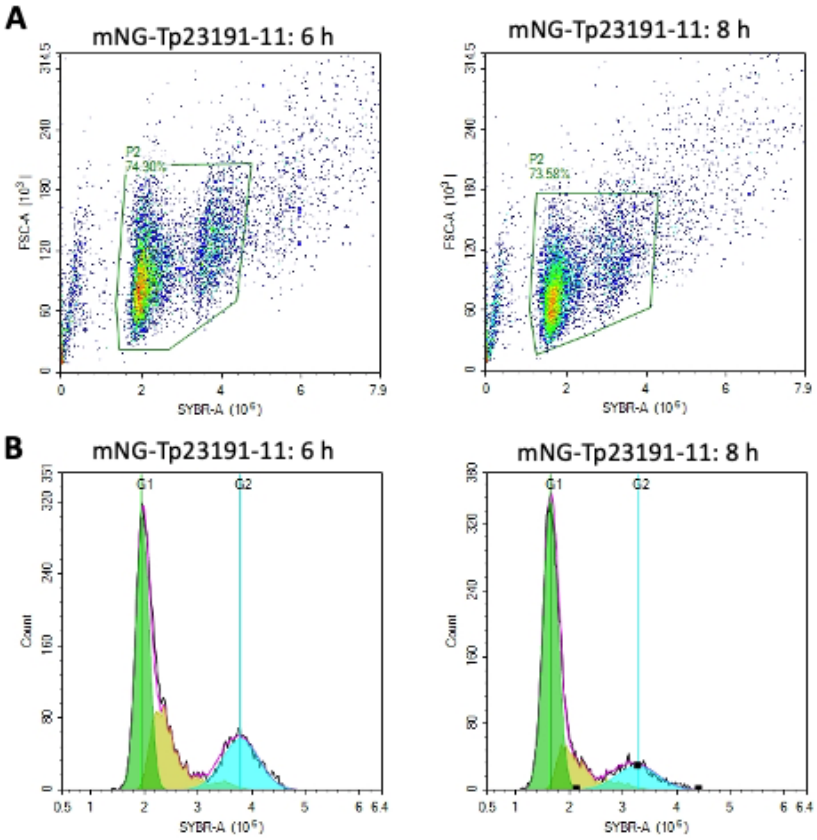

Figure D.1: Cell cycle stage determinations with NovoCyte software. **A**) Manual gating in NovoCyte of the population for each measurement. **B**) Distribution of cells in different stages of the cell cycle; G_1 (green), S (yellow) and G_2+M (blue). mNG-Tp23191-11 is a *T. pseudonana* transformant with integrated fusion protein mNG-Tp23191.

D.3 Protein Concentrations from *T. pseudonana* Cultures

Table D.2 summarizes the total protein concentration in different *T. pseudonana* cultures and the mean protein concentration per thousand cells. The overall concentration was greater for the *T. pseudonana* transformants with integrated pTpPuc3-mNG-Tp23191, compared to TpWt.

Table D.2: Protein concentration in *T. pseudonana* cultures after protein isolation. Samples were taken 4 h after Si-addition during the third synchronization study.

Culture of *T. pseudonana*	**Concentration [μg/mL]**	**Concentration [μg/cells·10^4]**
TpWt	308	1.52
mNG-Tp23191-4	484	2.79
mNG-Tp23191-11	496	2.84

D.4 Fluorescence Microscopy

Fluorescence microscope images of *T. pseudonana* cells from three different cultures of second generation transformants with fusion protein mNG-Tp23191 are given in Figure D.2. None of the examined cells showed any visible signs of expressed fusion protein. The contrast was adjusted on all images due to the low fluorescence signal in the range of mNG. This made it possible to see the complete overlap between fluorescence signals the optical filter within the range of mNG and autofluorescence.

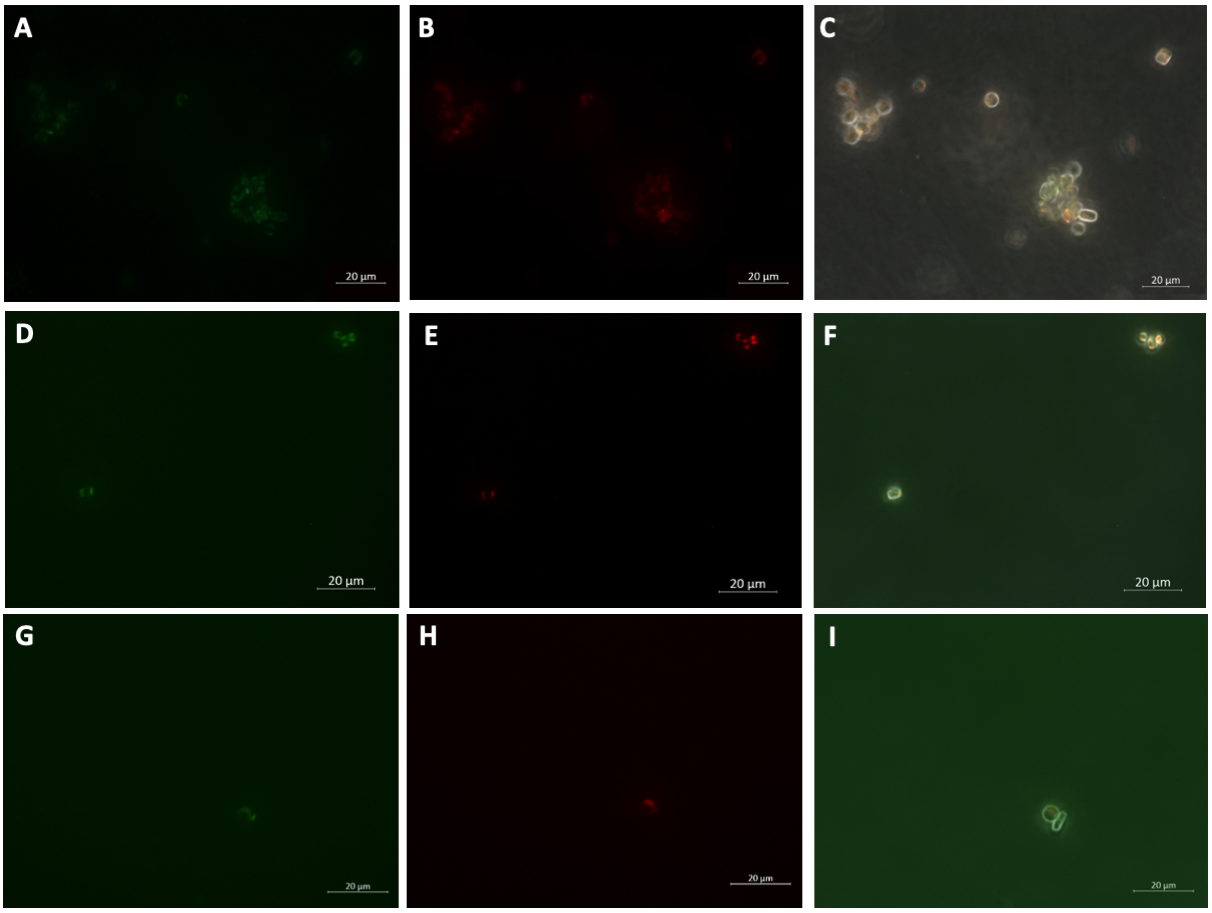

Figure D.2: Visualization of *T. pseudonana* transgenic lines with integrated fusion protein mNG-Tp23191. All images in each row show the same group of cells, but with different settings on the fluorescence microscope. Detected fluorescence signal between 505-555 nm is shown in the left images, while the fluorescence signal above 650 nm is shown in the middle images. The two channels of fluorescence signals are merged on top of a bright-field microscopy image in the right images, which makes it possible to see if there are any overlap. **A**) Transformant mNG-Tp23191-8. **B**) Transformant mNG-Tp23191-13. **C**) Transformant mNG-Tp23191-18.

D.5 Determination of Proper Inhibitor Concentrations

Graphical representations of the change in cell concentration among different cultures of *T. pseudonana* are given below. Only live cells was included in the plots. Two *T. pseudonana* transformants (mNG-Tp23191-7 and 8) and one wild type (Tpwt) were used for this experiment. Three inhibitors, each of four different concentrations, were added to separate cultures and incubated for 48 h. FCM was conducted at the start, 24 h, and 48 h after inhibitor-addition.

Inhibition with Cytochalasin D

Cytochalasin D, with a final concentration of 1.5 μM, 3.0 μM, 6.0 μM and 12.0 μM are given in Figure D.3-6, respectively.

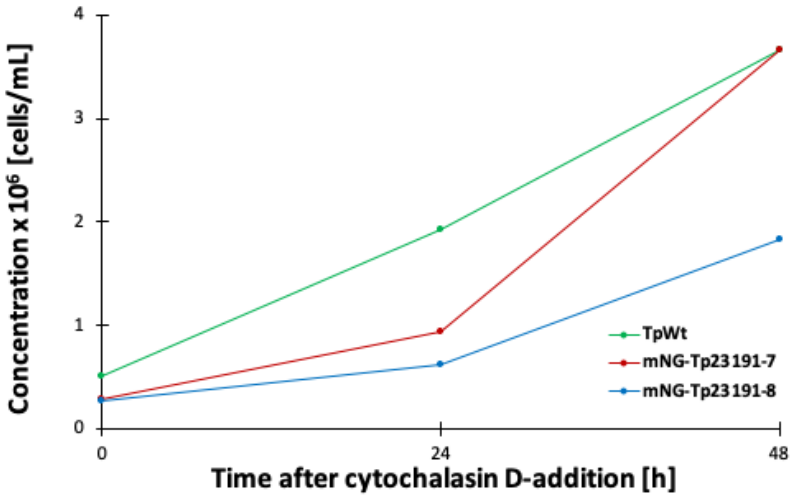

Figure D.3: *T. pseudonana* cultures were treated with cytochalasin D [1.5 μM]. The change in concentration as a function of time. Transformants with fusion protein are denoted mNG-Tp23191, while the wild type is called TpWt.

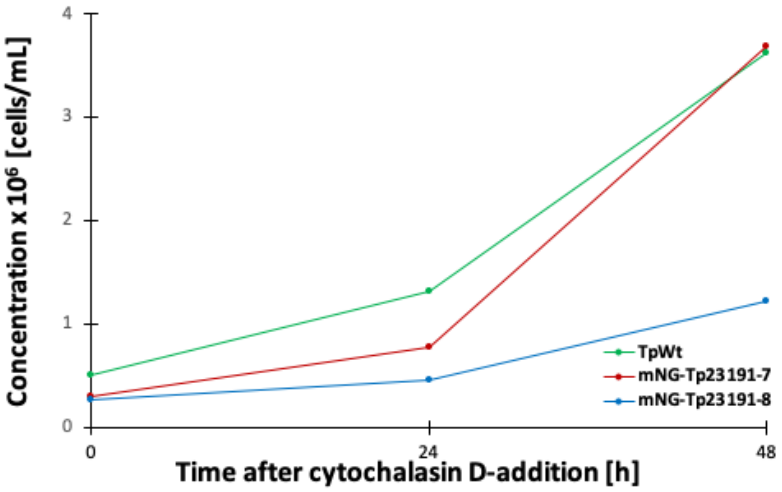

Figure D.4: *T. pseudonana* cultures were treated with cytochalasin D [3.0 μM]. The change in concentration as a function of time. Transformants with fusion protein are denoted mNG-Tp23191, while the wild type is called TpWt.

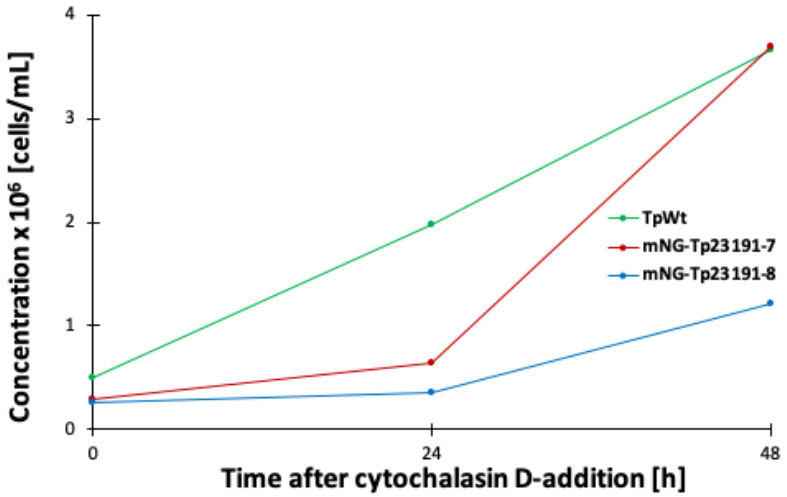

Figure D.5: *T. pseudonana* cultures were treated with cytochalasin D [6.0 μM]. The change in concentration is given as a function of time. Transformants with fusion protein are denoted mNG-Tp23191 while wild type is called TpWt.

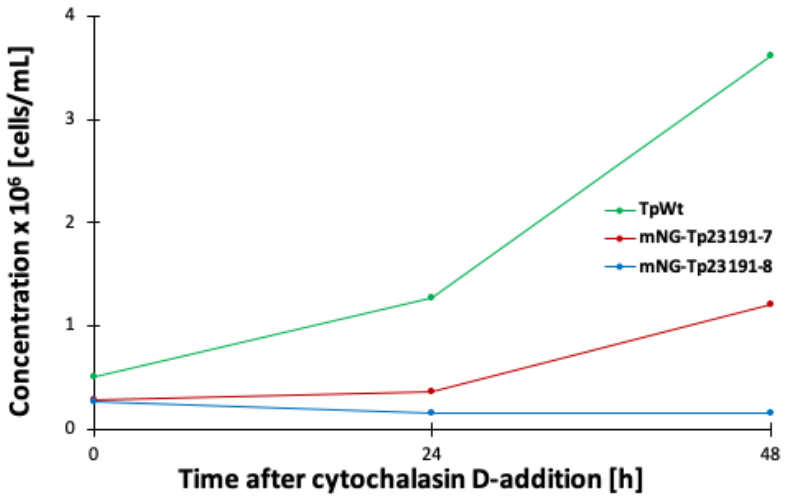

Figure D.6: *T. pseudonana* cultures were treated with cytochalasin D [12.0 μM]. The change in concentration as a function of time. Transformants with fusion protein are denoted mNG-Tp23191, while the wild type is called TpWt.

Inhibition with Colchicine

Colchicine, with a final concentration of 25 μM, 50 μM, 100 μM and 200 μM are given in Figure D.7-10, respectively.

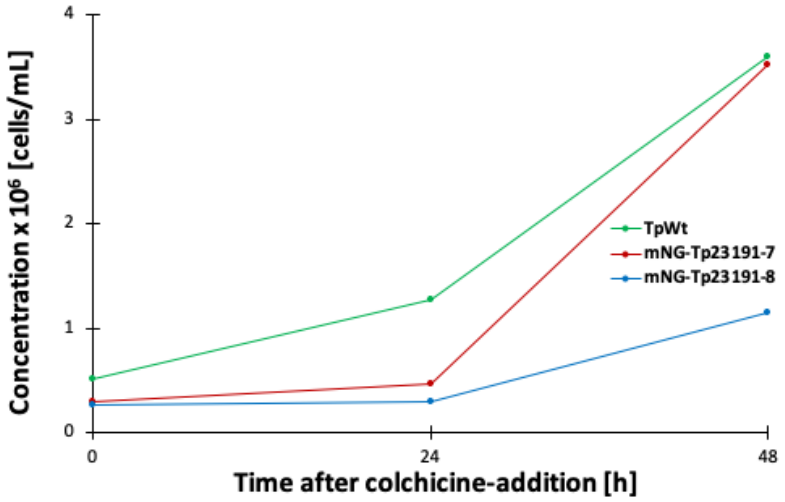

Figure D.7: *T. pseudonana* cultures were treated with colchicine [25 μM]. The change in concentration as a function of time. Transformants with fusion protein are denoted mNG-Tp23191, while the wild type is called TpWt.

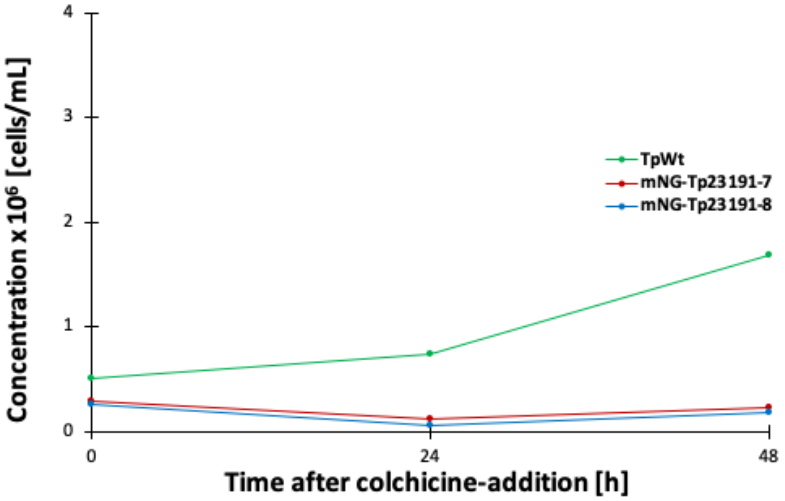

Figure D.8: *T. pseudonana* cultures were treated with colchicine [50 μM]. The change in concentration as a function of time. Transformants with fusion protein are denoted mNG-Tp23191, while the wild type is called TpWt.

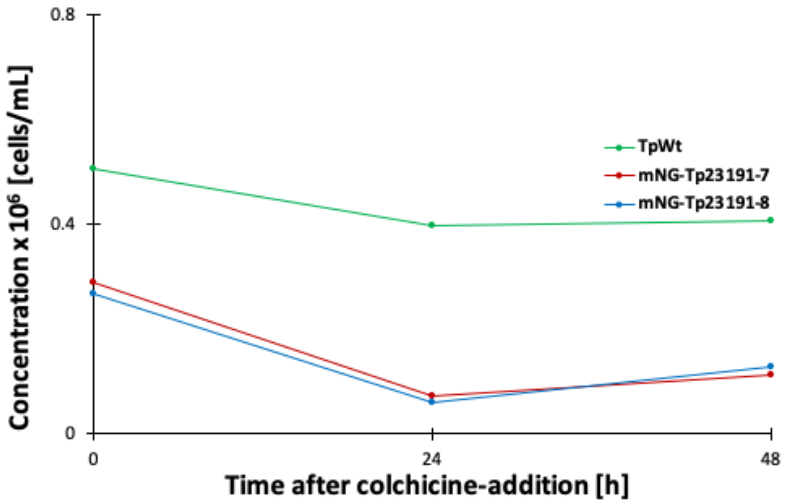

Figure D.9: *T. pseudonana* cultures were treated with colchicine [100 μM]. The change in concentration as a function of time. Transformants with fusion protein are denoted mNG-Tp23191, while wild type is called TpWt.

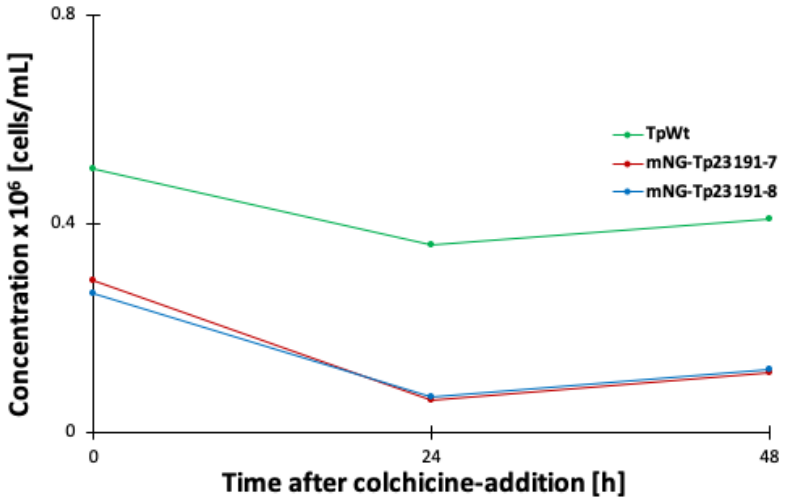

Figure D.10: *T. pseudonana* cultures were treated with colchicine [200 μM]. The change in concentration as a function of time. Transformants with fusion protein are denoted mNG-Tp23191, while the wild type is called TpWt.

Inhibition with Oryzalin

Oryzalin, with a final concentration of 0.1 μM, 0.2 μM, 0.4 μM and 0.8 μM are given in Figure D.11-14, respectively.

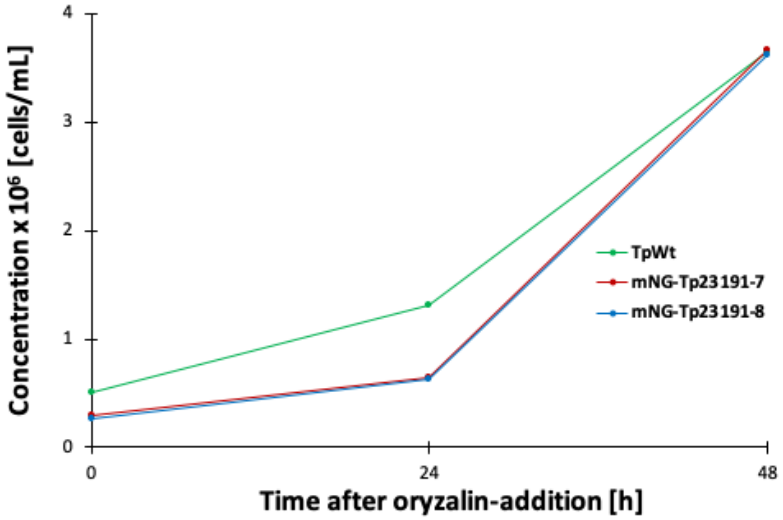

Figure D.11: *T. pseudonana* cultures were treated with oryzalin [0.1 μM]. The change in concentration as a function of time. Transformants with fusion protein are denoted mNG-Tp23191, while the wild type is called TpWt.

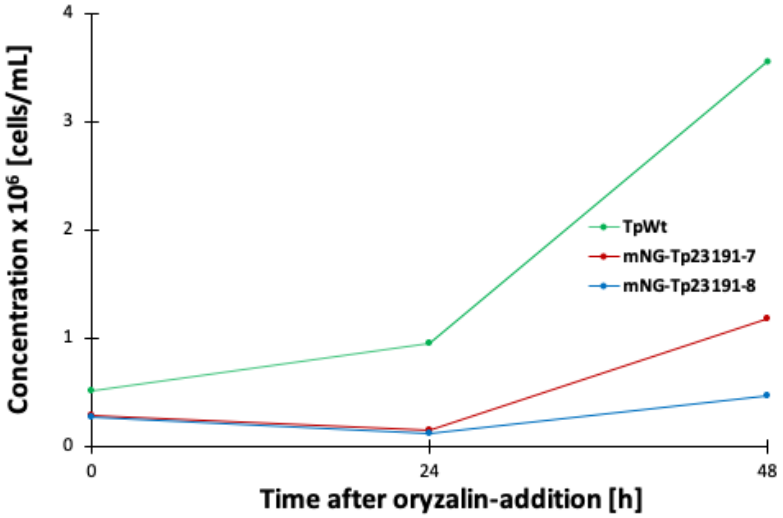

Figure D.12: *T. pseudonana* cultures were treated with oryzalin [0.2 μM]. The change in concentration as a function of time. Transformants with fusion protein are denoted mNG-Tp23191, while the wild type is called TpWt.

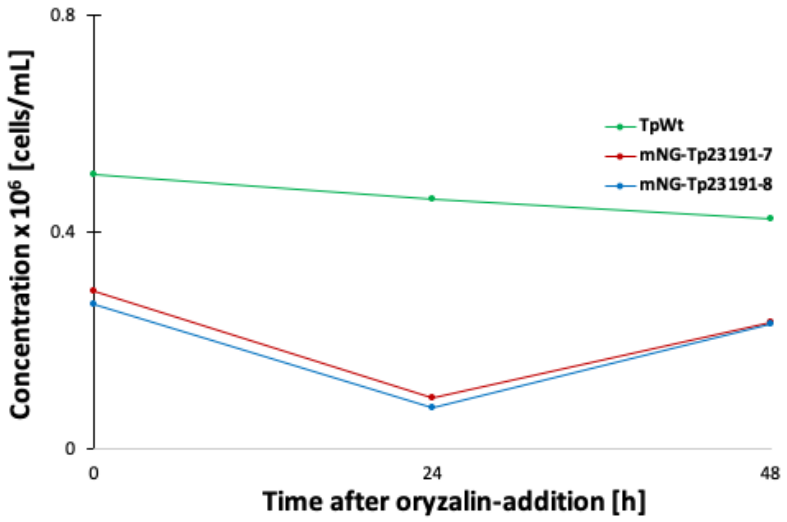

Figure D.13: *T. pseudonana* cultures were treated with oryzalin [0.4 μM]. The change in concentration as a function of time. Transformants with fusion protein are denoted mNG-Tp23191, while the wild type is called TpWt.

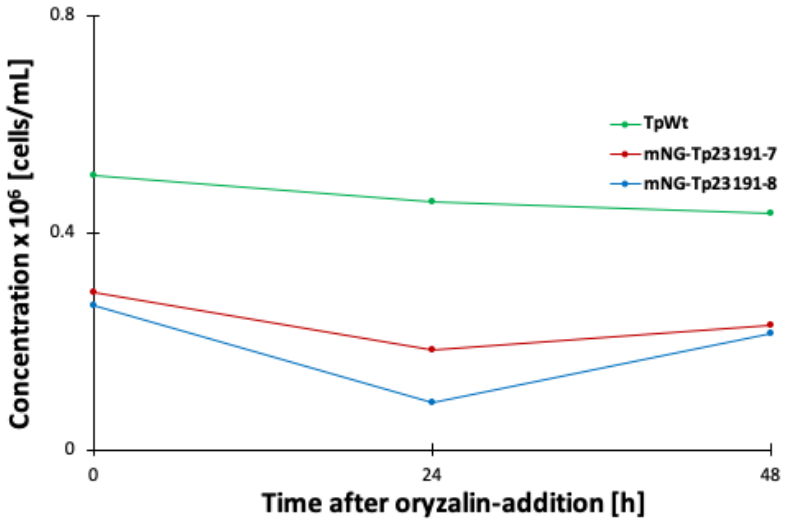

Figure D.14: *T. pseudonana* cultures were treated with oryzalin [0.8 μM]. The change in concentration as a function of time. Transformants with fusion protein are denoted mNG-Tp23191, while the wild type is called TpWt.

D.6 Examination of *T. pseudonana* Frustule Morphology after Cytoskeleton Inhibition

Table D.3 shows the number of rimoportulae on *T. pseudonana* frustules imaged with SEM. Frustules without treatment, and treated with the different cytoskeleton inhibitors are included.

Table D.3: The number of rimoportulae on the frustules after treatment of *T. pseudonana* with different cytoskeletal inhibitors. No treatment (None), cytochalasin D (Cyt D), colchicine (Colc), oryzalin (Oryz).

Treatment	**Number of rimoportulae**				
[μM]	7-8	9-10	11-12	13-14	16
None	2	6	2	1	-
Cyt D [0.6]	1	7	3	1	2
Col [40]	3	8	4	1	1
Oryz [0.2]	1	9	4	2	-

E Results from the Specialization Project

The following section includes results from functional studies of mNG-Tp23191 in transgenic lines of *T. pseudonana* collected by the author during the specialization project prior to this thesis [1]. The intracellular location of mNG-Tp23191 was determined with CLSM. Figure E.1 shows two images of *T. pseudonana* cells where the fluorescence signal from fusion protein mNG-Tp23191 (colored in green) does not overlap with autofluorescence from the chlorophyll (colored in red). It was concluded that the fusion protein is present at different locations consistent with valves and girdle bands. Several circular dots were observed on the outline of the cell and in the middle of the protoplast, which was presumed to be consistent with the location of SDVs. Moreover, the fluorescence signal within one diatom cell and between neighboring cells was in different intensities. The image in Figure E.2 was derived with fluorescence microscopy, and the detected fluorescence signal within the range of mNG is shown in green. Only some cells expressed the fusion protein, which led to the suggestion that mNG-Tp23191 is only present at certain stages of the *T. pseudonana* cell cycle.

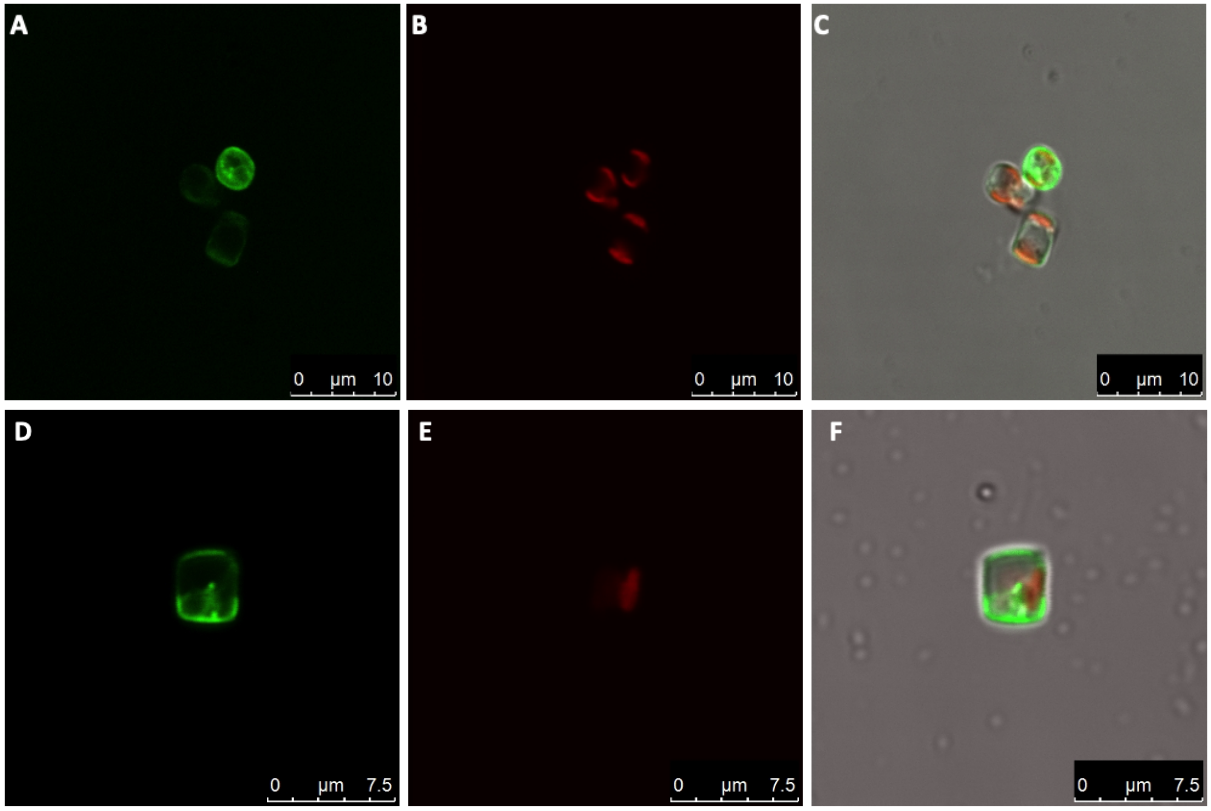

Figure E.1: Visualization of several *T. pseudonana* cells with integrated fusion protein mNG-Tp23191 using CLSM. **A-C**) A cell in valve view and two cells in girdle band view. **D-F**) A cell in girdle band view. Fluorescence detected within the range of mNG (colored in green) and autofluorescence (colored in red) are shown in the left and middle images, respectively. The image to the right is a bright-field microscope image. The fluorescence signals are also included, which makes it possible to detect the location of mNG-Tp23191.

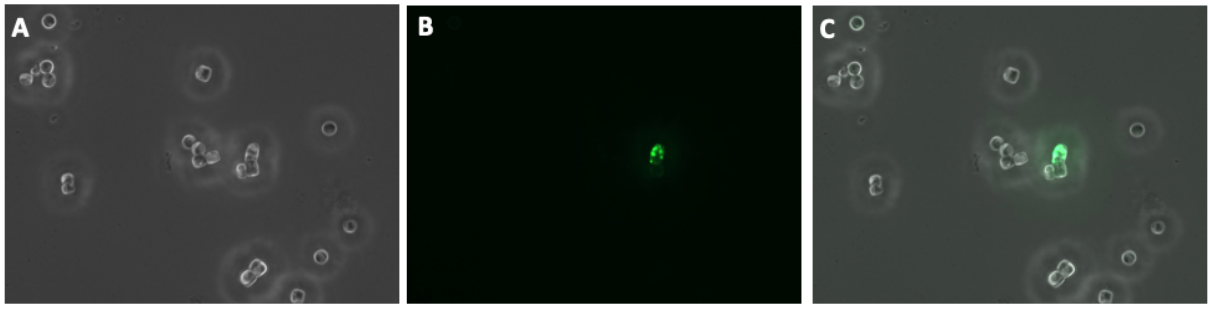

Figure E.2: Fluorescence microscopy of a *T. pseudonana* culture which contains plasmid pTpPuc3-mNeonGreen-Tp23191. Bright-field images and fluorescence microscopy images within the range of mNeonGreen are given in **A** and **B**, respectively. In **C**, both images are merged, which makes it possible to determine which cells that have visible the fusion protein.

Graphical representations of the synchronization study conducted with cultures of transgenic lines and wild types of *T. pseudonana* are given in Figure E.3. Only live cells were included in the plots. According to Figure E.3.A, there was a doubling in cell concentration 5 h after Si-addback for all colonies except for TpWt2. For the same time point, the mean fluorescence signal was slightly decreased, which was the same trend as the previous three hourly measurements. By comparing results to those of earlier studies, it was assumed that most diatoms had undergone cell arrest in the G_2+M phase of the cell cycle. As shown in Figure E.3.B, the highest mean fluorescence signal was detected after 1 h. Based on the assumption that most cells were arrested in the G_2+M phase prior to Si-addition, it was hypothesized that silicanin Tp23191 is present in this part of the diatom cell cycle, where valves are created in valve SDVs.

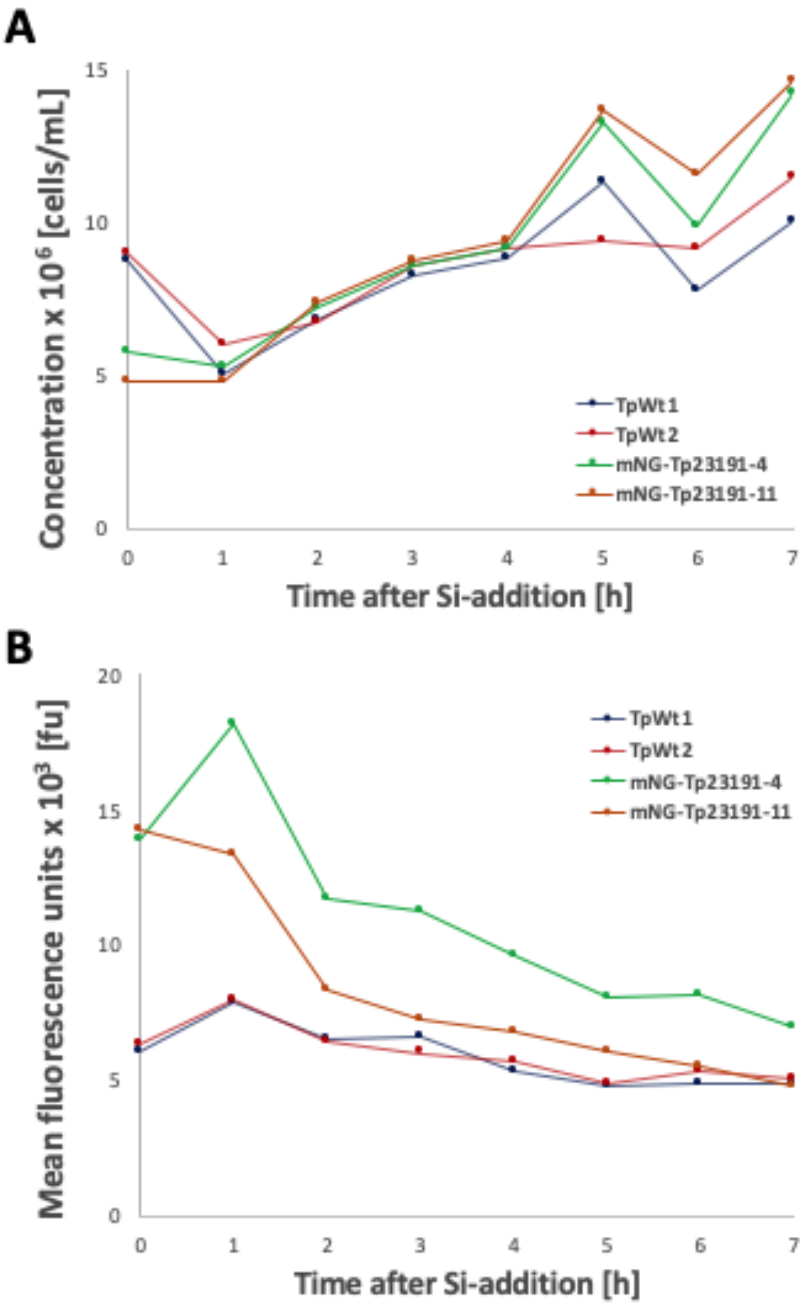

Figure E.3: All measurements are conducted after Si-replenishment on pre-silicate starved *T. pseudonana* transformants 4 and 11 with integrated mNG-Tp23191 and two wild types (wt). **A**) Cell concentration as a function of time. **B**) Mean fluorescence units detected within the range of mNG as a function of time.

Vilde Årdal

Cell Wall Biomineralization in the Centric Diatom *Thalassiosira pseudonana*: Silicanin Tp23191 and the Cytoskeleton

NTNU
Norwegian University of
Science and Technology